

**UNIVERSIDAD POLITÉCNICA DE MADRID**

**ESCUELA TÉCNICA SUPERIOR  
DE INGENIEROS DE TELECOMUNICACIÓN**



**MÁSTER UNIVERSITARIO  
EN INGENIERÍA DE TELECOMUNICACIÓN**

**MASTER'S THESIS**

**DESIGN AND IMPLEMENTATION OF A VIRTUAL  
REALITY TRAINING PLATFORM PROVIDED  
WITH HAPTIC FEEDBACK FOR FLEXIBLE  
URETERORENOSCOPY INTERVENTIONS WITH A  
MINIMALLY INVASIVE SURGICAL ROBOT**

**MARÍA PERAL BOIZA**

**2018**



**UNIVERSIDAD POLITÉCNICA DE MADRID**

**ESCUELA TÉCNICA SUPERIOR  
DE INGENIEROS DE TELECOMUNICACIÓN**



**MÁSTER UNIVERSITARIO  
EN INGENIERÍA DE TELECOMUNICACIÓN**

**MASTER'S THESIS**

**DESIGN AND IMPLEMENTATION OF A VIRTUAL  
REALITY TRAINING PLATFORM PROVIDED  
WITH HAPTIC FEEDBACK FOR FLEXIBLE  
URETERORENOSCOPY INTERVENTIONS WITH A  
MINIMALLY INVASIVE SURGICAL ROBOT**

**Autora:  
MARÍA PERAL BOIZA**

**Tutor:  
ÁLVARO GUTIÉRREZ MARTÍN**

**2018**



## Resumen

La presencia de cálculos en el tracto urinario se conoce con el nombre de litiasis urinaria o urolitiasis. Esta enfermedad urológica presenta una alta morbilidad en el mundo. Las recomendaciones recientes en el tratamiento de la urolitiasis se inclinan hacia procesos endourológicos, como la ureteroscopia flexible (URSf). Esta técnica mínimamente invasiva presenta importantes beneficios desde el punto de vista del paciente, como la reducción del daño causado en los tejidos. Sin embargo, a su vez presenta importantes inconvenientes para los urólogos, como problemas de ergonomía y exposición continua a radiación.

Con el objetivo de proporcionar una solución a este problema, el proyecto LITHOS, en el que este Trabajo de Fin de Máster está enmarcado, fue originado para la creación de una alternativa tecnológica basada en un sistema robótico quirúrgico de mínima invasión dedicado a intervenciones de ureterorrenoscopia flexible. Este sistema combina tanto los beneficios que la URSf ofrece a los pacientes, como soluciones a las limitaciones presentes desde la perspectiva de los cirujanos.

El objetivo principal de este Trabajo de Fin de Máster es el diseño e implementación de una plataforma de realidad virtual para el entrenamiento de los cirujanos en intervenciones de ureterorrenoscopia flexible con el sistema robótico del proyecto LITHOS, previa a la implementación del sistema quirúrgico final. La plataforma desarrollada incluye la misma interfaz de usuario que el sistema robótico. A su vez, se proporciona realimentación háptica al usuario para el control de la plataforma implementada mediante un manipulador de tres grados de libertad. De esta forma, se incrementa la inmersión del cirujano en la intervención. Diversos escenarios clínicos son simulados y presentados al especialista, incluyendo diferentes localizaciones y morfologías de los cálculos urinarios. El objetivo de la plataforma desarrollada es proporcionar un entorno efectivo de entrenamiento en procedimientos de URSf a los urólogos que manipulan el sistema robótico final.

**PALABRAS CLAVE:** ureterorrenoscopia flexible, simulación quirúrgica, cirugía robótica, entorno de entrenamiento, dinámica basada en posición, realimentación háptica, control en lazo cerrado.

## Abstract

The presence of calculi in the urinary tract is known as urinary lithiasis or urolithiasis. This urologic disease presents a high morbidity rate in the world. Recent urolithiasis treatment recommendations have changed towards endourologic procedures, such as flexible ureteroscopy (fURS). This minimally invasive technique presents many benefits from the patient point of view, like less damage to human tissue. However, it also presents important drawbacks to urologic surgeons, such as ergonomic problems and radiation exposure.

In order to provide a solution to this problem, the LITHOS project, where this Master's thesis is framed, was created to develop a technological alternative based on a minimally invasive surgical robot for flexible ureterorenoscopy interventions. It combines the benefits that fURS offers to the patients, and solutions to the limitations encountered from the surgeons perspective.

The main objective of this Master's thesis is the design and implementation of a virtual reality training platform for flexible ureterorenoscopy interventions with the LITHOS system, prior to the implementation of the final surgical system. This developed platform includes the same user interface as the robotic system. Moreover, haptic feedback is provided for the control of the implemented platform with a three degrees of freedom manipulator, so as to increase the immersion of the surgeon in the intervention. Diverse clinical scenarios are simulated and presented to the specialist, including different calculi locations and morphologies. The objective of the implemented platform is to provide an effective training environment for urologic surgeons manipulating the robotic system in fURS interventions.

**KEYWORDS:** flexible ureterorenoscopy, surgical simulation, robotic surgery, training environment, position based dynamics, shape matching, haptic feedback, closed-loop control.

## Agradecimientos

Primeramente quiero dar las gracias a mi tutor Álvaro Gutiérrez Martín por toda la ayuda recibida y su inestimable dedicación y apoyo, tanto técnico como humano, durante la realización de este Trabajo Fin de Máster. También quiero agradecer a Félix Monasterio-Huelin su colaboración y sus consejos. Muchas gracias a ambos por todas sus clases de teoría de control y robótica impartidas y a las que tuve la suerte de asistir, y porque ellos me han introducido en el apasionante mundo de los sistemas hápticos.

Muchas gracias también al resto de miembros y compañeros del Robolabo, por apoyarme cada día, sacarme siempre una sonrisa e impulsarme hacia adelante en los momentos complicados.

A su vez quiero dar mi más sincero gracias a los profesores que tuve la gran suerte de tener durante el colegio, y a los que debo las bases de lo que ahora sé. Ellos me enseñaron que todo logro conlleva un esfuerzo constante, sin atajos y sin excusas.

También quiero agradecerle a mis amigos cercanos todo el apoyo que me han mostrado desde siempre. Porque a su lado todos los retos son posibles.

Y por supuesto, quiero dar las gracias a mis padres y a mi hermana Ana, por escucharme, por aconsejarme, por apoyarme, por entenderme, por quererme. Por estar siempre a mi lado, en los buenos y malos momentos. Porque sin ellos nada de esto habría sido posible y a los que les debo todo. Y a mis abuelos, a los que tanto quiero.



# CONTENTS

<b>Resumen</b>	<b>v</b>
<b>Abstract</b>	<b>vi</b>
<b>Agradecimientos</b>	<b>vii</b>
<b>Contents</b>	<b>viii</b>
<b>List of Figures</b>	<b>xi</b>
<b>List of Tables</b>	<b>xiv</b>
<b>1 Introduction and objectives</b>	<b>1</b>
1.1 Problem statement . . . . .	1
1.1.1 Introduction to flexible ureteroscopy (fURS) . . . . .	1
1.1.2 Surgical robots . . . . .	5
1.1.3 Surgical simulation in flexible ureteroscopy . . . . .	10
1.1.4 Introduction to haptic feedback . . . . .	13
1.2 Motivation and objectives . . . . .	14
1.3 Document layout . . . . .	15
<b>2 Dynamic model of a flexible ureterorenoscope</b>	<b>17</b>
2.1 Introduction to the simulator . . . . .	17
2.2 Dynamics algorithm . . . . .	21
2.2.1 Insertion . . . . .	22
2.2.2 Flexion and rotation . . . . .	27
2.3 Algorithm implementation . . . . .	29

2.3.1	Collision detection . . . . .	30
2.3.2	Collision response . . . . .	31
<b>3</b>	<b>Force feedback</b>	<b>35</b>
3.1	Introduction to the developed haptic system . . . . .	35
3.2	Hardware architecture description . . . . .	37
3.2.1	DC motors . . . . .	37
3.2.2	DC motor driver . . . . .	39
3.2.3	Mechanical design of the haptic system . . . . .	41
3.3	Integration with the training platform . . . . .	44
<b>4</b>	<b>Validation</b>	<b>51</b>
4.1	Dynamics rendering validation . . . . .	51
4.2	Haptic feedback validation . . . . .	57
<b>5</b>	<b>Conclusions and future work</b>	<b>59</b>
5.1	Conclusions . . . . .	59
5.2	Future work . . . . .	61
	<b>Appendices</b>	<b>63</b>
<b>A</b>	<b>Ethical, economic, social and environmental aspects</b>	<b>65</b>
A.1	Introduction . . . . .	66
A.2	Description of significant impacts associated with this project . . . . .	67
A.3	Detailed analysis of a significant impact . . . . .	68
A.4	Conclusions . . . . .	68
<b>B</b>	<b>Economical budget</b>	<b>71</b>
<b>C</b>	<b>Faulhaber DC Gearmotors 2619S012SR 22:1 + IE2-16 - Motor &amp; Encoder specifications</b>	<b>73</b>
<b>D</b>	<b>Faulhaber DC Micromotor 1516E012SR + 16A 41:1 + IE2-16 - Motor &amp; Encoder specifications</b>	<b>77</b>
	<b>Bibliography</b>	<b>81</b>

# LIST OF FIGURES

1.1	On the left, rigid ureteroscope (Nick Brook Urologist, 2013); on the right, semirigid ureteroscope (Basillote et al., 2004). . . . .	3
1.2	On the left, flexible ureteroscope (Basillote et al., 2004); on the right, flexible ureteroscopes ease the exploration of the upper urinary tract (European Association of Urology, 2018c). . . . .	4
1.3	Urologist surgeons have to maintain an unnatural posture during traditional flexible ureteroscopy interventions (Boston Scientific Urology, 2016). . . . .	5
1.4	Da Vinci surgical system (Intuitive Surgical Inc, CA, USA) (Simorov et al., 2012). . . . .	6
1.5	The TELELAP ALF-X surgical system (SOFAR S.p.A., ALF-X Surgical Robotics Department, Milan, Italy) (Fanfani et al., 2015). . .	7
1.6	Patient site (left) and surgeon site (right) of the RAVEN Surgical Robot (University of Washington, WA, USA) (Lum et al., 2009). . . . .	7
1.7	The magnetic navigation system Niobe (Stereotaxis, MO, USA) (Wikipedia, 2018). . . . .	8
1.8	Patient site (left) and surgeon site (right) of the robotic catheter system Sensei X2 (Hansel Medical Inc, CA, USA) (Hansel Medical Inc, 2016). . .	8
1.9	Flex robotic system (Medrobotics Corporation, MA, USA) (Remacle et al., 2015). . . . .	9
1.10	Surgeon manipulator (left) and robotic slave end effector (right) of MASTER (Nanyang Technological University and National University Health System, Singapore) (Simorov et al., 2012). . . . .	9
1.11	Patient site (left) and surgeon site (right) of the Avicenna Roboflex (ELMED, Ankara, Turkey) (Saglam et al., 2014). . . . .	10

1.12	(a) URO Mentor system (Simbionix, Tel Aviv, Israel) (Simbionix, 2016); (b) Scope Trainer (Mediskills Ltd., Edinburgh, United Kingdom) (Mediskills Ltd., 2015); (c) Uro-Scopic Trainer (Limbs and Things, Bristol, United Kingdom) (Limbs and Things); (d) Adult Ureteroscopy Trainer (Ideal Anatomic Modelling, MI, USA) (White et al., 2010) . . . . .	12
1.13	Impedance control architecture. . . . .	14
1.14	Admittance control architecture. . . . .	14
2.1	SpaceMouse Compact by 3Dconnexion (3Dconnexion, 2018). . . . .	18
2.2	3D mouse movements to control flexion, rotation and insertion of the virtual endoscope in design phase. . . . .	18
2.3	Virtual endoscope model implemented in the design phase. On the left, radiographic vision; on the right, endoscopic vision. . . . .	19
2.4	3D mice used as endoscope controllers. On the left, 3D mouse for the left hand controlling rotational motion (1) and insertion motion (2). On the right, 3D mouse for the right hand responsible for flexion motion (3). . . . .	20
2.5	On the left, the continuous flexible endoscope model; on the right, its discretization. . . . .	21
2.6	Section of the virtual endoscope body implemented: vertical distance constraints and flexibility degree constraints between adjacent nodes. . . . .	23
2.7	Geometric representation of the vertical distance constraint. . . . .	25
2.8	Geometric representation of the flexibility degree constraint. . . . .	25
2.9	Geometric representation of the junction constraint. . . . .	27
2.10	Simplified scheme followed for the flexion and rotation graphical computation. . . . .	28
2.11	Simplified example of the implemented algorithm based on a binary search principle to compute the rotation matrix $R_2$ , with a balanced binary tree of four levels. . . . .	29
2.12	Basic architecture of the developed simulation program. . . . .	30
2.13	Basic principle of the bounding box hierarchy (Weller, 2013). . . . .	31
2.14	Nodes of depth 4 in the axis aligned bounding box hierarchical tree of the implemented three-dimensional ureterorenal model. . . . .	32
2.15	The “finger-proxy” algorithm tries to reduce the distance between the proxy and goal positions. . . . .	32
2.16	Configuration space obstacles and constraint planes (Ruspini et al., 1997). . . . .	33
3.1	Simplified scheme of the developed impedance force closed loop. . . . .	36
3.2	Module of the transfer function in angular velocity of the motor for insertion and flexion. . . . .	38

3.3	Module of the transfer function in angular velocity of the motor for rotation. . . . .	40
3.4	Simplified H bridge circuit. . . . .	40
3.5	Flowchart of the design and assembly process of the final haptic system. . . . .	42
3.6	On the left, final designed 3D CAD model for controller 1 (a and c) and final 3D printed and assembled haptic controller 1 (e). On the right, final designed 3D CAD model for controller 2 (b and d) and final 3D printed and assembled haptic controller 2 (f). . . . .	43
3.7	Final mechatronic system. . . . .	44
3.8	Flowchart of the implemented haptic loop. . . . .	44
3.9	Range of motion of insertion and flexion control (left) and rotation (right). . . . .	45
3.10	Frames of bits for the serial communication used for position (up) and force (down) transmission. . . . .	46
3.11	Control architecture for the integration of force feedback in the virtual platform. . . . .	46
3.12	Proxy (in blue) and virtual cursor (in red) of the “finger-proxy” algorithm. $\Delta x$ (in gray) is used for the force calculation with the Hooke’s Law. . . . .	48
3.13	Force calculation implemented based on the Hooke’s Law. . . . .	49
4.1	Performance of the simulated endoscope model in three different scenarios (from left to right: Scenario 1, 2 and 3, respectively). . . . .	52
4.2	Mean computational frequency results obtained with seven experiments of 15 seconds in scenarios 1, 2 and 3. . . . .	53
4.3	Implemented virtual reality environment user interface, including endoscopy (right) and radiography (left) screens. . . . .	53
4.4	Simulation of the lithotripsy procedure. . . . .	54
4.5	Computational frequency results obtained with experiments of 15 seconds in Scenario 4. . . . .	54
4.6	Relation between mean computational frequency and number of nodes colliding. . . . .	55
4.7	Implemented virtual reality environment user interface for the force feedback close loop (radiographic view). . . . .	57
A.1	Impacts in relation to the area of influence and the life cycle phase of the product. . . . .	66
B.1	Economical budget of the project. . . . .	72



# LIST OF TABLES

2.1	Results from evaluation of prototype developed in the design phase. . .	19
3.1	Parameters of Faulhaber DC Gearmotors 2619S012SR 22:1 + IE2-16 (see Appendix C). . . . .	37
3.2	Parameters of Faulhaber DC Micromotor 1516E012SR + 16A 41:1 + IE2-16 (see Appendix D). . . . .	39
3.3	Possible states of the H bridge configuration with a DC motor. . . . .	41
3.4	Required number of bits for transmission. . . . .	45
4.1	Comparison mean percentage of execution time running at the different frequency ranges in Scenarios 1, 2, 3 and 4. . . . .	55
4.2	Mean percentage of execution time running at the different frame rates in Scenario 4 for both display modes. . . . .	56
4.3	Mean time required for force calculation and communication. . . . .	58
4.4	Mean percentage of execution time running at the different frequency ranges in Scenarios 4 with force feedback. . . . .	58

## CHAPTER

# 1

## INTRODUCTION AND OBJECTIVES

### 1.1 Problem statement

#### 1.1.1 Introduction to flexible ureteroscopy (fURS)

Urinary lithiasis or urolithiasis is defined as the presence of calculi in the urinary tract. This urologic disease presents a high morbidity rate in the world. According to a recent study carried out to determine the current prevalence of stone disease in the USA, one out of 11 individuals suffers from kidney stones at some point in their lives, being the prevalence of stones equal to 8.8% (10.6% for men and 7.1% for women) (Scales et al., 2012). Moreover, the increase of the prevalence and incidence of urolithiasis in other countries has also been reported in the last years (Hesse et al., 2003; Yasui et al., 2008; Prezioso et al., 2014; Heers and Turney, 2016). In addition, the urolithiasis incidence in pediatric patients has significantly increased in the last decades according to several studies (Routh et al., 2010; Sas et al., 2010; Dwyer et al., 2012; Edvardsson et al., 2018).

The causes of this increasing morbidity are unclear and currently debated. Although genetic factors have been associated with the risk of suffering from this urologic affection, it is believed that environmental factors play a major role in the recently increasing rates. Current lifestyle habits, such as diet, obesity or dehydration are linked to the development of kidney stone. Moreover, climate factors are also associated with this disease. Regions with elevated temperature present higher risk for kidney stones. Global warming is also linked to the increase of the urolithiasis prevalence and will have a significant impact on it in the following decades (Sofia and Walter, 2016; Sorokin et al., 2017). However, this urologic disease is very complex and further studies have to be performed to determine the risk factors in order to prevent and reduce the stone formation.

The urologic procedures for active treatment and removal of urinary tract calculi are the following:

- Extracorporeal shock-wave lithotripsy (SWL) is a minimally invasive procedure in which urinary calculi are fragmented by using focused shock waves originated from the outside of the body by a shock-wave generator. The resulting fragments from the lithotripsy (stone fragmentation) are smaller than the original calculus and they will pass with urine some time after the procedure (European Association of Urology, 2018b).
- Percutaneous nephrolithotomy (PNL) is a minimally invasive surgical procedure in which large calculi can be extracted directly from the kidney. The patient kidney is accessed using a tubular medical instrument, the nephroscope, that is inserted through the skin. It typically requires general anaesthesia (European Association of Urology, 2018a).
- Ureteroscopy (URS) is a minimally invasive technique to treat calculi located in any part of the urinary tract. It is performed with a ureteroscope inserted through the urethra and bladder into the ureter or kidney. This medical tubular instrument is composed of different channels. These channels enable the insertion of a fiber optic camera to acquire intraoperative images, stone baskets to extract the calculi, or a laser to perform lithotripsy. It typically requires general anaesthesia (European Association of Urology, 2018c).
- Open surgery is an invasive procedure in which the urinary tract is accessed through surgical incisions in the patient skin and urinary calculi can be directly treated and removed. It requires general anaesthesia.

Urologic guidelines state since more than one decade that open stone surgery has to be considered only in exceptional situations, usually associated with calculi complexity, failure of previous minimally invasive interventions and patient anatomical abnormalities (Alivizatos and Skolarikos, 2006). Moreover, the renal and ureteral calculi treatment recommendations included in the recent European Association of Urology guidelines have changed towards endourologic procedures, such as URS and PNL, versus SWL (Türk et al., 2016).

Likewise, global urolithiasis treatment trends have clearly changed in the same direction, according to (Geraghty et al., 2017), that considered data of URS, PNL, SWL and open surgery interventions. The study also revealed the important uptrend in the use of URS technique and its promising future.

As mentioned before, ureteroscopy is an endourologic minimally invasive procedure that allows the surgeon to access and treat stones located in any part of the urinary tract, thanks to the insertion of the ureteroscope into the ureter or kidney. The first ureteroscopic intervention was performed in 1912 by Young. Since this moment, ureteroscopes have experienced significant advancements. The first



Figure 1.1: On the left, rigid ureteroscope (Nick Brook Urologist, 2013); on the right, semirigid ureteroscope (Basillote et al., 2004).

endoscopes were rigid (see Figure 1.1a). The intraoperative view was achieved with thin lenses that were then replaced by glass rods, allowing for a better light transmission and a reduction of the endoscope diameter. Currently, the optical design is typically based on fiberoptics. Most of rigid ureteroscopes have been replaced by semirigid ureteroscopes (see Figure 1.1b). The first semirigid ureteroscope was reported in 1989. When fiberoptics were applied to rigid ureteroscopes, their shaft could also become more flexible without image distortion. In addition, it is less likely to break a semirigid endoscope than a rigid endoscope (Basillote et al., 2004).

The first report of flexible ureteroscopy (fURS) was published in 1964 by Marshall. Progress of flexible ureteroscopy was closely related to the development of flexible fiberoptics. However, the use of flexible ureteroscopes expanded only after more recent advances in this technology were achieved. Figure 1.2a depicts a flexible ureteroscope with 270 degrees of deflection in two directions. The incorporation of active tip deflection to passive flexible ureteroscopes represented an important advance in the exploration of the upper urinary tract by endourologic techniques (see Figure 1.2b). The deflection mechanism of the current flexible endoscopes includes one or two actively deflectable segments and a passive segment located proximal to the former. Whereas the active deflection of the tip is controlled by the surgeon with a mechanism on the handle of the endoscope, the passive deflection refers to the bending of the passive segment, which is more flexible than the rest of the endoscope, in contact with the urinary tract tissue. The inclusion of holmium laser was also a great enhancement of this technology in order to allow intracorporeal lithotripsy, as well as stone retrieval devices, such as stone graspers and baskets, to capture and remove calculi (Basillote et al., 2004; Buscarini and Conlin, 2008; Alenezi and Denstedt, 2015).

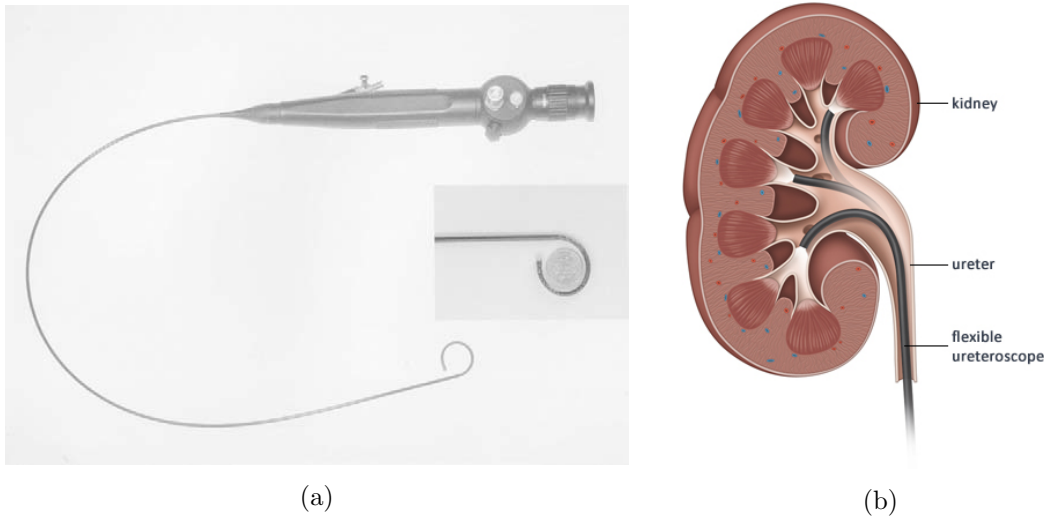


Figure 1.2: On the left, flexible ureteroscope (Basillote et al., 2004); on the right, flexible ureteroscopes ease the exploration of the upper urinary tract (European Association of Urology, 2018c).

The use of flexible ureteroscopy has experienced determining improvements over the past years, including design modifications, miniaturization of the distal tip and deflection increase, along with new digital video technologies and intracorporeal lithotripsy devices (Beiko and Denstedt, 2007). These ongoing advances have led to an increase in the use of fURS and the expansion of its potential indications. It has been proved to be a safe and effective technique when performed with holmium laser lithotripsy in the treatment of urinary calculi, presenting high stone-free rate and low morbidity (Breda et al., 2008, 2009).

However, although ureteroscopy techniques offer many benefits from the patient perspective, they also present some drawbacks to urologic surgeons. These surgical procedures involve serious ergonomics problems, as the surgeon maintains a standing position during the whole intervention, holding the ureteroscope up and turning the head to look at the endoscopy and radiography screens (see Figure 1.3). This position leads to musculoskeletal pains and joints stiffness (Saglam et al., 2014; Geavlete et al., 2016a). Moreover, the endourologic surgeon is exposed to important doses of ionizing radiation from X-rays, used to acquire intraoperative images.

The LITHOS project objective is the design and development of a novel surgical remotely controlled robotic system for flexible ureterorenoscopic lithotripsy interventions, aiming for combining both the benefits that these procedures present for the patients and also solutions to the drawbacks they have from the surgeons point of view. The final system is based on a multifunctional collaborative robot located in the patient site for the endoscope manipulation, which is teleoperated by the surgeon from a control panel. This two sites approach provides the urologic specialists with a more ergonomic workspace, remote from radiation sources.



Figure 1.3: Urologist surgeons have to maintain an unnatural posture during traditional flexible ureteroscopy interventions (Boston Scientific Urology, 2016).

### 1.1.2 Surgical robots

Minimally invasive surgery (MIS) involves surgical procedures that aim to cause less damage to human tissue than traditional open surgical techniques. It is performed through small incisions or trocars, so its advantages over traditional open surgery are numerous: shorter recovering periods, minor postoperative complications, less scarring, shorter hospital stays, reduced pain and lower morbidity rate (Jaffray, 2005).

Moreover, MIS indications are widely expanded in many medical areas, like gynecology and urology (Mack, 2001), and it provides an effective and safe alternative to traditional open surgery in different types of surgical interventions (Smithers et al., 2007; Lacy et al., 2008; Guillotreau et al., 2009). In addition, advances in surgical instrumentation, focused on constant equipment miniaturization and refinement, have contributed to reduce tissue damage during MIS procedures.

However, MIS also presents several drawbacks. The learning curve for most surgeons is longer when compared to open surgery, and these procedures can also present longer operating time and higher equipment costs (Fuchs, 2002). The occasional possibility of conversion to an open procedure due to intraoperative complications can occur during MIS interventions. A loss of the visibility of the operative area, the tactile perception and the surgeon dexterity are also associated with MIS. Moreover, ergonomics problems causing physical symptoms on surgeons have been repeatedly reported (Park et al., 2010; Sari et al., 2010; Miller et al., 2012).

Robot-assisted surgery (RAS) is also becoming an expanded technology. Computer-assisted manipulation offers greater precision and can increase the surgeon dexterity during minimally invasive procedures (Fuchs, 2002). Some of them also include haptic feedback, which intensifies enormously the immersive experience of the surgeon in the actual intervention. In addition, important ergonomic improvements

from the surgeons point of view are achieved with robotic surgery systems when compared with traditional procedures (Lee et al., 2005; Saglam et al., 2014; Geavlete et al., 2016a). The feasibility of robot-assisted minimally invasive procedures has been demonstrated in different types of interventions (Cadiere et al., 2001; Pigazzi et al., 2006; Coronado et al., 2012; Lee et al., 2014).

Currently available surgical robotic systems for minimally invasive procedures are performing interventions in different clinical areas, such as laparoscopy, catheterization and ureterorenoscopy.

The Da Vinci surgical system (Intuitive Surgical Inc, CA, USA) is composed by four computer-manipulated robotic arms to operate the patient and a surgeon console provided with stereoscopic view, hand controls and pedals, where the specialist remains seated during the intervention (see Figure 1.4). The robotic arms in the operative site system replicate identically the movements performed in the control console. It provides the surgeons with up to seven degrees of freedom (DOF). It has been demonstrated to offer advantages over traditional MIS interventions (Hubens et al., 2003; Maeso et al., 2010).



Figure 1.4: Da Vinci surgical system (Intuitive Surgical Inc, CA, USA) (Simorov et al., 2012).

The TELELAP ALF-X surgical system (SOFAR S.p.A., ALF-X Surgical Robotics Department, Milan, Italy) provides a new robotic approach to minimally invasive procedures offering haptic feedback to the surgeon (see Figure 1.5). It comprises a remote control unit with 3D vision and an eye-tracking camera control system. The patient site includes three or four manipulator arms with six DOF each. In contrast to the Da Vinci surgical system, it is not possible to use wristed instrumentation with the TELELAP ALF-X system, which is extremely useful in complex surgical interventions. Nevertheless, its feasibility and effectiveness in different clinical procedures have been reported (Alletti et al., 2015; Fanfani et al., 2015, 2016).

The RAVEN Surgical Robot (University of Washington, WA, USA) is a robotic system for MIS procedures that provides haptic interaction (see Figure 1.6). It includes the patient site with two articulated manipulators of seven DOF each, and the surgeon site that is composed of two control devices and a video display from the operation field. The patient site is based on a spherical mechanism that has been optimized for the best kinematic performance of the system in a very compact



Figure 1.5: The TELELAP ALF-X surgical system (SOFAR S.p.A., ALF-X Surgical Robotics Department, Milan, Italy) (Fanfani et al., 2015).



Figure 1.6: Patient site (left) and surgeon site (right) of the RAVEN Surgical Robot (University of Washington, WA, USA) (Lum et al., 2009).

workspace. It has been used in several telesurgical experiments, obtaining successful outcomes (Lum et al., 2009).

The robotic Percutaneous Access to the Kidney (PAKY) device (The Johns Hopkins Medical Institutions, MD, USA) is comprised of a radiolucent, sterilizable needle driver located at the terminal end of a robot arm with seven DOF. The movement of the needle is performed by a DC motor that is controlled with a joystick. It has been proved to be an effective and safe system in clinical interventions and in vitro experiments (Cadeddu et al., 1998). In addition, its accuracy and feasibility when combined with a remote center of motion (RCM) device of two DOF have been determined in comparison to standard manual access (Su et al., 2002).

The magnetic navigation system Niobe (Stereotaxis, MO, USA), for catheter interventions, is based on two computer-controlled permanent magnets that are located on opposite sides of the patient (see Figure 1.7). They generate an external magnetic field that can be precisely manipulated in order to steer a small magnet in the distal tip of the catheter. The insertion of the catheter is controlled by a motor



Figure 1.7: The magnetic navigation system Niobe (Stereotaxis, MO, USA) (Wikipedia, 2018).

drive. Several clinical studies in patients determined the effectiveness of this system (Ernst et al., 2004; Kiemeneij et al., 2008).

The robotic catheter system Sensei X2 (Hansel Medical Inc, CA, USA) includes the remote catheter manipulator, the Artisan Extend Control Catheter and a remote surgeon console with screens and a three-dimensional master controller device (see Figure 1.8). The Artisan Extend Control Catheter provides six DOF. The catheter tip replicates the movements performed on the console controller. The catheter system allows force feedback to the surgeon when performing surgical procedures. In addition, although this system was created for cardiac applications, it was demonstrated that the Sensei system is feasible for performing ureterorenoscopic interventions, after undergoing the required software and configuration modifications (Desai et al., 2008, 2011).

Flex robotic system (Medrobotics Corporation, MA, USA) is composed of a highly articulated flexible scope and was specifically developed for transoral robotic surgery.



Figure 1.8: Patient site (left) and surgeon site (right) of the robotic catheter system Sensei X2 (Hansel Medical Inc, CA, USA) (Hansel Medical Inc, 2016).

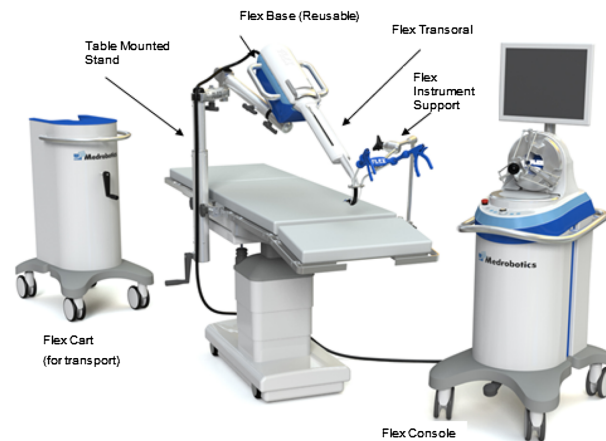


Figure 1.9: Flex robotic system (Medrobotics Corporation, MA, USA) (Remacle et al., 2015).

It allows to steer flexible surgical instruments like endoscopes. The system consists of three different units: The Flex Cart, with the Flex Base and the Flex Scope, the Flex Console, and the Flex Instruments (see Figure 1.9). The flexible scope is controlled by the surgeon with a manipulator from the Flex console, which provides haptic feedback. Many clinical validations have been performed with the Flex robotic system, providing that this system is easy to use, safe and effective in transoral robotic surgery (Remacle et al., 2015; Mattheis et al., 2017).

MASTER (Nanyang Technological University and National University Health System, Singapore) is a master-slave endoscopic robot designed for natural orifice transluminal endoscopic surgery (see Figure 1.10). It provides nine DOF and haptic feedback. It is necessary that an endoscopist introduces the endoscope into the patient. After the endoscope has been correctly positioned, the robotic slave can

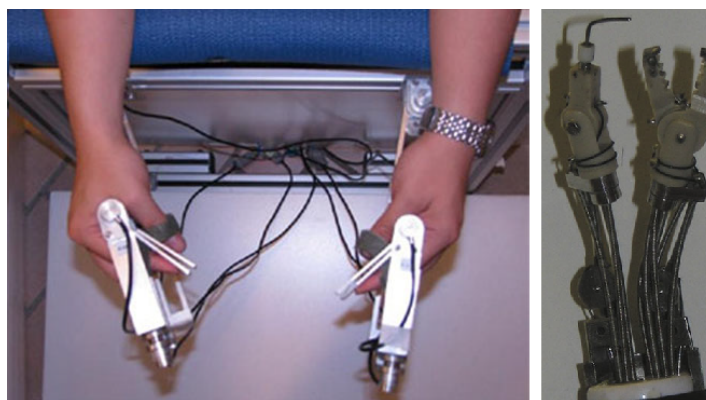


Figure 1.10: Surgeon manipulator (left) and robotic slave end effector (right) of MASTER (Nanyang Technological University and National University Health System, Singapore) (Simorov et al., 2012).

be precisely controlled by the surgeon. It was proved to be a feasible surgical system to perform endoscopic sub-mucosal dissections to segmental hepatectomies in animal models (Lomanto et al., 2015; Peters et al., 2018).

Finally, the Avicenna Roboflex (ELMED, Ankara, Turkey) is a robot specifically designed for flexible ureteroscopy (see Figure 1.11). It is composed of the surgeon console and the manipulator of the flexible endoscope. Two joysticks and pedals, a wheel and a control monitor allow manipulating the endoscope from the remote unit. The manipulator is composed of a motor system and a robotic arm where the endoscope is fixed. Moreover, a system in the robotic arm allows the insertion of the laser fibre for the lithotripsy procedure. It was reported to be a suitable and safe system in clinical interventions (Saglam et al., 2014; Geavlete et al., 2016b).

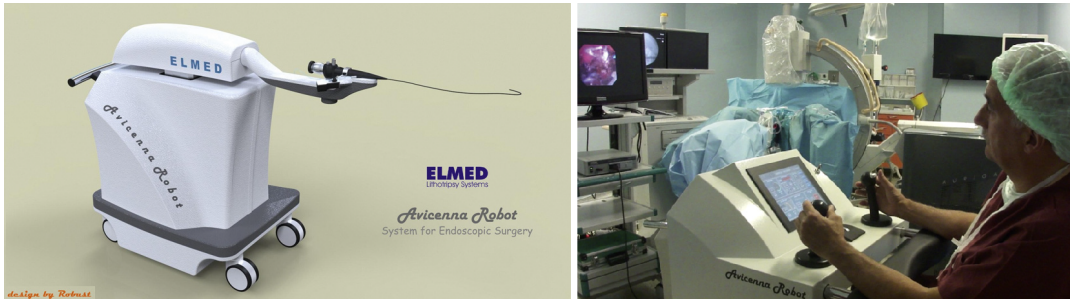


Figure 1.11: Patient site (left) and surgeon site (right) of the Avicenna Roboflex (ELMED, Ankara, Turkey) (Saglam et al., 2014).

Although many robotic surgical systems have been designed for MIS interventions, just a few of them are able to work on flexible ureteroscopy. It is within this gap where the LITHOS project emerges.

### 1.1.3 Surgical simulation in flexible ureteroscopy

The benefits of surgical simulation in medical training, including robot-assisted surgery, have been repeatedly reported (Kunkler, 2006; Al Bareeq et al., 2008). Its advantages generally involve improvements in the efficiency and skills of the surgeon, learning curve reduction, improved educational experience, reduction in costs and easy access to different clinical scenarios. In addition, virtual reality (VR) simulation is becoming more widespread in medical applications. Several studies have already established the usefulness of VR simulation as a mean to train MIS technical skills (Våpenstad and Buzink, 2013).

Simulation platforms for ureterorenoscopy training have been previously developed. URO Mentor system (Symbionix, Tel Aviv, Israel) is a high fidelity computer-based platform for the simulation of rigid and flexible cystoscopic and ureterorenoscopic procedures (see Figure 1.12a). This platform allows training calculi lithotripsy and extraction, irrigation pressure control, contrast material injection

and performing biopsies in real time simulation with realistic haptic feedback. It also provides anatomic and non-anatomic practice exercises with different levels of difficulty in order to acquire basic skills. It is composed of a personal computer and an operating table with a mannequin and a monitor for displaying intraoperative images (Michel et al., 2002). In (Dolmans et al., 2009), 89 urologists and residents in urology performed urological interventions and evaluated the platform afterwards as realistic and useful as an educational tool. In (Schout et al., 2010), the real time performance of cysto-urethroscopy interventions was analyzed for 100 different interns. 50% of the participants had received prior training with the URO Mentor system before performing the procedure on the patients. The results showed that the trained participants performance was significantly better.

The Scope Trainer (Mediskills Ltd., Edinburgh, United Kingdom) is a benchtop model that allows the user to simulate standard endoscopic procedures, such as flexible cystoscopy, rigid or flexible ureteroscopy or intracorporeal lithotripsy (see Figure 1.12b). This platform consists of a urinary tract model, including a distensible bladder, that can be accessed through the ureteral orifice in order to perform an endoscopic examination as in a real intervention (Watterson and Denstedt, 2007). In (Brehmer and Tolley, 2002), 14 urologists were scored when performing rigid ureteroscopy on the model and patients. The participants performed equally on both model and patients, and they considered the procedure on the model similar to the real surgery. In (Brehmer and Swartz, 2005), the performance of 26 urologists during semi-rigid ureteroscopy was analyzed before and after training with the Scope Trainer. Results showed that the performance was better after training, and the confidence of all participants also improved after using the model.

Similarly, the Uro-Scopic Trainer (Limbs and Things, Bristol, United Kingdom) is a benchtop model that consists of a male genitourinary tract model that provides a training system for urethroscopy, cystoscopy, rigid and flexible ureteroscopy, lithotripsy and stone retrieval (Watterson and Denstedt, 2007) (see Figure 1.12c). In (Matsumoto et al., 2001), 17 urologists were assessed while performing stone removals in the Uro-Scopic Trainer before and after a didactic training session with the model. The scores after training improved significantly.

The Adult Ureteroscopy Trainer (Ideal Anatomic Modelling, MI, USA) is a high-fidelity benchtop model of a collecting system. It is composed of the kidney, renal pelvis access, ureter and ureteral orifice (see Figure 1.12d). A study with a total of 46 participants, including experienced and novice urologists, was performed to validate the system. The results showed that 100% of the participants rated the trainer as realistic and easy to use, 98% thought it is a good training system and 96% would use it to practice during residency (White et al., 2010).

The surgical simulation platform presented in this Master's thesis is focused on the medical training for flexible ureterorenoscopic interventions using the robotic surgical system implemented in the LITHOS project. In comparison with the previously described simulation platforms, all the composing elements of the developed training

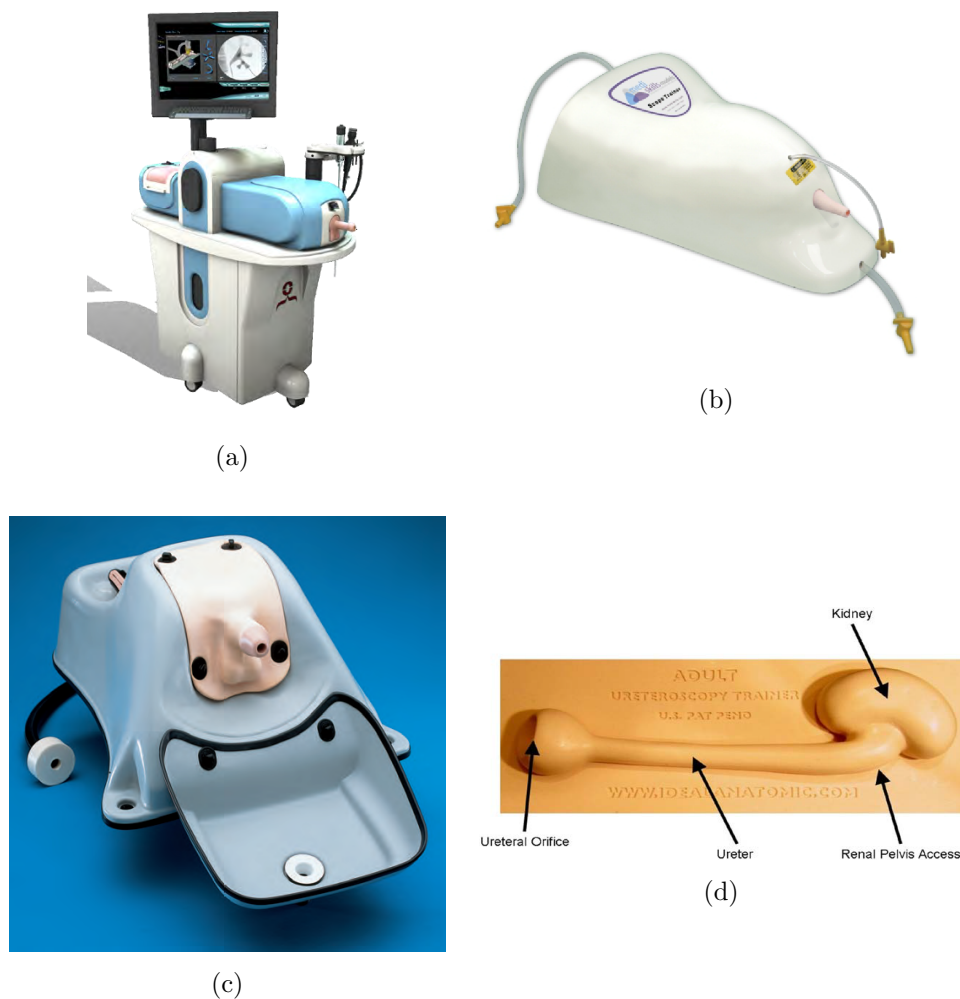


Figure 1.12: (a) URO Mentor system (Symbionix, Tel Aviv, Israel) (Symbionix, 2016); (b) Scope Trainer (Mediskills Ltd., Edinburgh, United Kingdom) (Mediskills Ltd., 2015); (c) Uro-Scopic Trainer (Limbs and Things, Bristol, United Kingdom) (Limbs and Things); (d) Adult Ureteroscopy Trainer (Ideal Anatomic Modelling, MI, USA) (White et al., 2010)

environment in this Master's thesis are computer-based. The proposed interface is identical to the one from the surgeon console of the robotic system, providing the same scenario than in a real surgical intervention. The surgeon site is composed of an ergonomic seat with two controllers for the hands, and two different displays for endoscopic and radiographic intraoperative images. Moreover, the surgical robot controllers provide force feedback to the surgeon to increase the immersion of the surgeon in the real intervention and to prevent possible tissue damage.

### 1.1.4 Introduction to haptic feedback

The introduction of force and tactile feedback in robotic surgery attempts a reduction of the loss of haptic feedback related to most of conventional minimally invasive interventions. Traditional open surgery allows direct tissue examination by touching. However, when the surgeon manipulates the tissue by means of surgical instruments and tools to perform less invasive procedures, the tactile and kinesthetic information perceived by the surgeon decreases. This leads to several drawbacks, such as the impossibility of locate of certain tissue structures or the assessment of tissue characteristics by palpation, and the application of excessive or insufficient forces over tissues and sutures (Trejos et al., 2010). In order to prevent it, some current robotic surgical systems include haptic feedback, like the TELELAP ALF-X surgical system, the RAVEN Surgical Robot, the robotic catheter system Sensei X2, the Flex robotic system and the MASTER system.

A haptic device is defined as a system that provides touch perception to the user, to sense and feel shapes and textures from objects that may not be close to the user. Generally, this stimuli is caused by a force feedback generated in the haptic device and provided to the user. However, there are other types of haptic stimuli that do not necessarily imply force transmission, like temperature changes.

A closed-loop control system or active control system maintains a specific relation between the system output and the reference input, in order to reduce the error signal and make the output take a desired value. In contrast to open-loop control systems, in which the output signal does not affect the control signal, the difference between the output and the reference signals (called error signal) is used to control the current output of the closed-loop control system (Ogata, 2010). In haptic systems, the input signal is produced by the user actions and the output signal is generated by the system. This output signal is in charge of creating the haptic stimulus in the user.

Since their creation, haptic systems have been arranged into diverse classifications regarding their different features. One of them is based on the type of feedback that is generated and provided to the user, which creates different natures of stimulus. The haptic systems can be divided into (Oakley et al., 2000):

- Tactile feedback systems are those related to the skin sensation. They provide information about contours, geometry and other surface characteristics of the object that is being explored by the user, such as roughness and temperature.
- Force feedback systems are those related to kinesthetic sensation. They provide mechanic stimuli and forces that inform about the position, orientation or weight of the object that is being explored by the user.

However, some haptic systems present both type of feedback, which can intensify the haptic experience of the final user.

Another classification of haptic devices is based on the close-loop control architecture that they implement. There are two types of active haptic devices depending on the function of the sensors and actuators (Anam and Al-Jumaily, 2012):

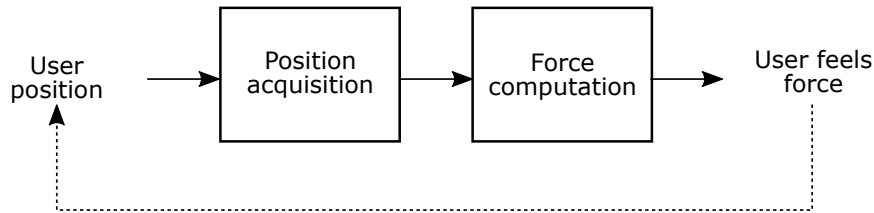


Figure 1.13: Impedance control architecture.

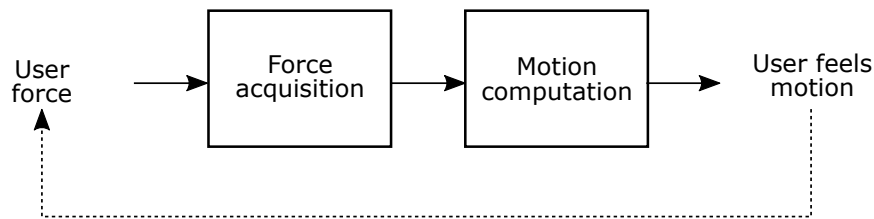


Figure 1.14: Admittance control architecture.

- Impedance control haptic devices are those in which sensors measure the position of the user movements, and actuators generate the force that is applied to the user (see Figure 1.13).
- Admittance control haptic devices are those in which sensors measure the force that the user applies to the manipulator, and actuators compute and apply the position that the manipulator requires to provide the user a motion (see Figure 1.14).

The simulation training platform developed in this Master's thesis includes an impedance control closed loop between the endoscope controllers in the surgeon console and the virtual reality environment to provide the specialist with force feedback.

## 1.2 Motivation and objectives

As stated in Section 1.1, the increasing tendency observed in the urolithiasis morbidity around the world also applies to the usage of endourologic procedures for the treatment of this urologic disease. Moreover, flexible ureteroscopy is also becoming a more frequent procedure for the treatment of urinary stones. This minimally invasive technique presents many benefits from the patient point of view, like less damage to human tissue. However, it also presents important drawbacks to urologic surgeons, such as ergonomic problems and radiation exposure.

In order to provide a solution to this problem, the LITHOS project, where this Master's thesis is framed, was created to develop a technological alternative based on a minimally invasive surgical robot for flexible ureterorenoscopy interventions. It

combines the benefits that fURS offers to the patients, and solutions to the drawbacks encountered from the surgeons perspective.

The main objective of this Master's thesis is the design and implementation of a virtual reality training platform for flexible ureterorenoscopy interventions with the LITHOS system, prior to the implementation of the final surgical system. This developed platform includes the same user interface as the robotic system. Moreover, haptic feedback is provided for the control of the implemented platform with a three degrees of freedom manipulator, so as to increase the immersion of the surgeon in the intervention. Diverse clinical scenarios are simulated and presented to the specialist, including different calculi locations and morphologies. The objective of the implemented platform is to provide an effective training environment for urologic surgeons manipulating the robotic system in fURS interventions.

### 1.3 Document layout

This document is organized in the following chapters, that include the developed tasks to achieve the objectives stated in Section 1.2:

- In Chapter 1, the problem statement, the motivation and the main objectives of this Master's thesis have been explained.
- In Chapter 2, the dynamic model of the flexible ureterorenoscope developed for the training platform is described, as well as the algorithm implementation.
- In Chapter 3, the integration of the endoscope dynamics algorithm implemented in Chapter 2 with a force feedback closed loop is described. In this chapter, further details about the mechanical design of the haptic system are provided.
- In Chapter 4, the validation of the systems developed in Chapters 2 and 3 is presented.
- In Chapter 5, conclusions and future work drawn from this Master's thesis are exposed.



## CHAPTER

## 2

# DYNAMIC MODEL OF A FLEXIBLE URETERORENOSCOPE

### **2.1 Introduction to the simulator**

The main objective of the implemented platform is to provide the urologists who use the LITHOS robot with a realistic and feasible environment for training for flexible ureterorenoscopy interventions. Diverse clinical cases can be simulated and presented to the surgeon, including different calculi locations and morphologies. The previous training aims to help them to acquire the required skills for performing ureteroscopic interventions with the robotic system and to reduce the learning curve. This environment can be also used for the surgical planning of future fURS interventions. The training platform presents a user interface identical to the one of the robotic final system, in which the motions of the flexible ureteroscope are controlled remotely from the surgeon control panel and performed in the patient site by the final actuator system.

The design of the surgeon site aims to provide the urologists with a more ergonomic workplace, in order to reduce unnatural or uncomfortable postures during long periods of time, and also to keep the surgeon away from ionizing radiation of X-rays, used to acquire intraoperative images. The control panel is composed by a comfortable seat for the surgeon, a hand controller device and two monitors, which display the radiographic and endoscopic intraoperative images. The controller device is a 3D mouse. A 3D mouse is an electronic device that produces six degrees of freedom position and orientation information. It is designed to control digital content in an easy and intuitive way using only one hand. The 3D mouse used for this project is

the SpaceMouse Compact by 3Dconnexion (see Figure 2.1) <sup>1</sup>.



Figure 2.1: SpaceMouse Compact by 3Dconnexion (3Dconnexion, 2018).

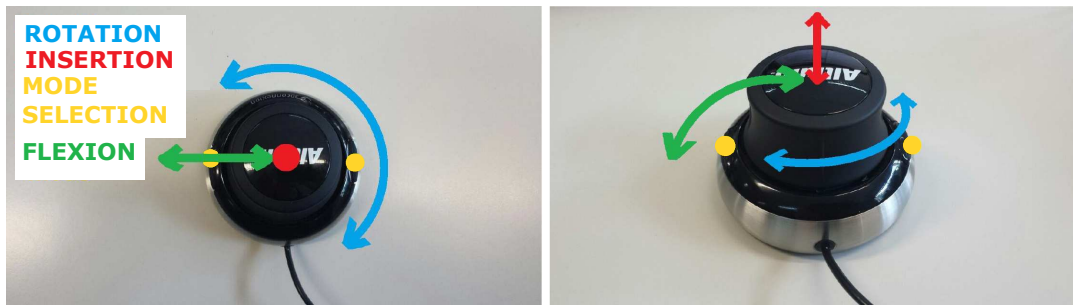


Figure 2.2: 3D mouse movements to control flexion, rotation and insertion of the virtual endoscope in design phase.

The development of the training platform was divided in two different phases: the design phase and the implementation phase.

In the design phase, the requirements of the platform were defined and a very simple virtual model of the training environment was developed. One 3D mouse was used to control the virtual endoscope degrees of freedom: flexion, rotation and insertion (see Figure 2.2). The virtual endoscope model was implemented using rigid body dynamics, without considering collisions with external objects, in a non-anatomic scenario (see Figure 2.3). This virtual model is not deformable during collisions and it provides two different modes of endoscope tip deflection: manual and automatic. The selection of the deflection mode is performed by pressing both side buttons of the 3D mouse simultaneously. In the manual deflection mode, the flexion

<sup>1</sup>[https://www.3dconnexion.co.uk/spacemouse\\_compact/uk/](https://www.3dconnexion.co.uk/spacemouse_compact/uk/)

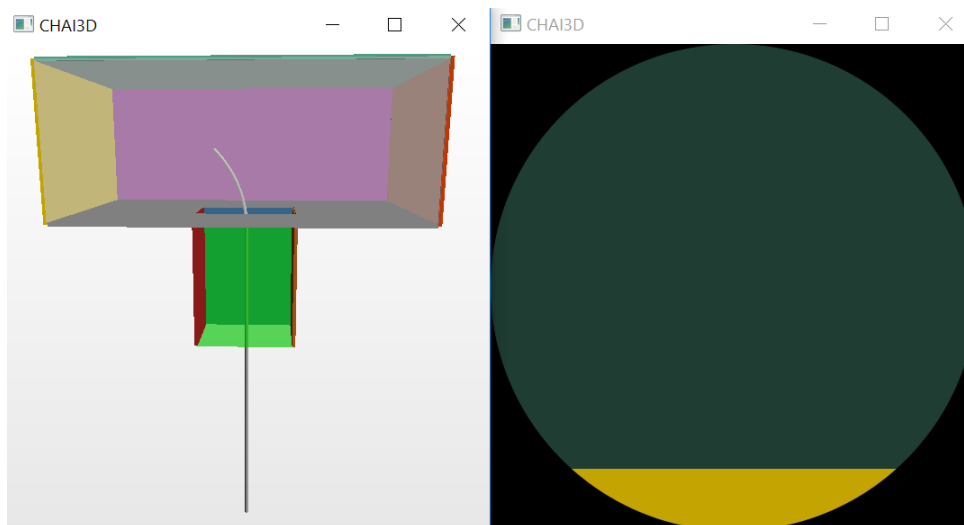


Figure 2.3: Virtual endoscope model implemented in the design phase. On the left, radiographic vision; on the right, endoscopic vision.

level of the deflectable endoscope tip configured by the surgeon remains invariable once the surgeon stops controlling the 3D mouse. In the automatic deflection mode, the deflectable tip recovers the extended configuration once the surgeon stops controlling the 3D mouse. The prototype implemented in this first stage of the development was used to firstly evaluate the design of the final robot interface with several urologists. The feedback provided by two surgeons, with more than 5 years of experience in ureterorenoscopy, was collected using an evaluation rate between 1-5 for assessing the control of each endoscope degree of freedom (see Table 2.1). According to this feedback, the control of the insertion and rotation levels could be easily and intuitively performed, obtaining a rate of 4 and 5, respectively. The manual deflection mode obtained a better rate in comparison to the automatic mode. Moreover, the surgeons indicate that, although the control of the 3D mouse may require a previous training session, it is easy and comfortable to manipulate. They stated that the integration of this controller device in the surgeons daily work would have a positive impact, and they pointed out its feasibility in other types of urologic procedures. In addition, the surgeons indicated that separation between motions in different devices allows them to have a better control of the position of the endoscope distal tip.

DOF	Surgeon 1	Surgeon 2
Insertion	4	4
Rotation	5	5
Manual deflection	3	2
Automatic deflection	1	1

Table 2.1: Results from evaluation of prototype developed in the design phase.



Figure 2.4: 3D mice used as endoscope controllers. On the left, 3D mouse for the left hand controlling rotational motion (1) and insertion motion (2). On the right, 3D mouse for the right hand responsible for flexion motion (3).

The implementation phase took the feedback provided by the surgeons as a starting point. In this phase, two 3D mice were used as endoscope controllers, one for each hand (see Figure 2.4), in order to decouple the degrees of freedom of the endoscope tip for a better control of its absolute position. In this phase, the implemented deflection mode was the manual mode.

As in the design phase, the implemented flexible ureteroscope model has three degrees of freedom that are controllable by the surgeon: rotation, insertion and flexion (see Figure 2.4). Rotation and insertion motions of the endoscope are manipulated with the left 3D mouse, whereas flexion motion is controlled with the right one. In addition, the developed training environment includes the simulation of intracorporeal lithotripsy procedure, calculi fragmentation monitoring and both intracorporeal views from endoscopy and radiography. The laser activation for lithotripsy is performed by pressing both side buttons of the right 3D mouse simultaneously, so as to minimize unintentional laser shots.

In the implementation phase, a deformable model of the virtual endoscope was implemented. This virtual endoscope is actively deflectable by the surgeon and passively deformable during collisions with external objects. In order to simulate the flexible endoscope, the solid model was discretized in a finite number of solid elements, as depicted in Figure 2.5. Being  $N$  the total number of nodes, each node is represented by index  $i$  ( $i \in [0, \dots, N - 1]$ ). The shape of the solid elements is spherical, defined by a specific radius, in order to simplify the implementation of the collision detection method.

The flexible endoscope dynamic model developed is founded on the position based approach (Müller et al., 2007) and the shape matching method (Müller et al., 2005). Vertical distance constraints, flexibility degree constraints and geometric constraints were established between the spherical nodes, as well as external collision constraints.

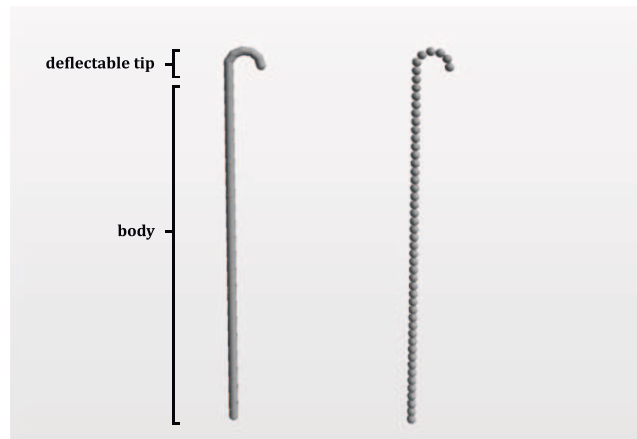


Figure 2.5: On the left, the continuous flexible endoscope model; on the right, its discretization.

The three-dimensional endoscope model is divided into two sections and their dynamics are modeled with different graphic algorithms: deflectable tip and body. The dynamics of the deflectable tip is based on the shape matching graphical approach. On the other side, the position based dynamics algorithm was used to model the performance of the endoscope body. The position of both sections is determined by the user input control over rotation, insertion and flexion levels, and also by the external collisions with environment objects. Moreover, it is important to point out that the positions of both sections are mutually dependent, since they actually constitute a solid body.

The control by the user of the three degrees of freedom of the endoscope impacts directly on the shape of the virtual model. Flexion motion actuates the endoscope tip, whereas endoscope insertion and rotation are performed from the insertion orifice and affect the whole model. However, since the rotation of the endoscope would only have a visual effect on the deflectable tip due to the spherical geometry of the solid nodes, it has been considered that rotational motion only actuates the endoscope tip for simplification.

In Section 2.2, the application of both algorithms for the modeling of the dynamics of the virtual flexible endoscope is explained in detail.

## 2.2 Dynamics algorithm

For the development of the deformable virtual endoscope, dynamics based on the position approach (Müller et al., 2007) and the shape matching method (Müller et al., 2005) were implemented. The main difference between these dynamics simulation methods in comparison to classical approaches is that the former works directly on the position of the objects, omitting the velocity layer. Classical simulation methods are based on force rendering. Total forces exerted on the objects are calculated in

order to compute accelerations with the Newton's second law of motion. Using a time integration method, velocities and finally the positions of the objects are calculated. Classical simulation methods for modeling deformable objects are reviewed in (Nealen et al., 2006), such as mass-spring systems, the Finite Element Method (FEM), the Finite Volume Method or the Method of Finite Differences.

One of the simplest methods is the mass-spring approach. In this method, the object is composed of a set of point masses that are connected by springs. The forces are modeled with the Hooke's law. This approach is very simple to implement, but it presents limitations, such as the difficulty of tuning the spring constants or the inability of capturing volumetric effects directly, like volume conservation or volume inversion prevention (Bender et al., 2015). These limitations are not present in the Finite Element Method, in which a deformable object is considered as a continuous connected volume (Nealen et al., 2006). However, this method is more computationally expensive.

The main application of the geometry based methods is interactive environments. Because of their stability, robustness, simplicity and high level of control, they are becoming very popular in computer graphics and in the game industry in the last years. These characteristics make the position based methods suitable for developing the virtual endoscope model for this project. One of the most important features that the developed training platform has to present is a high frequency rendering, for enabling the real time interaction of the user with the simulation and the integration of a close loop haptic feedback.

Previous surgical simulations have been developed using position based dynamics. In (Berndt et al., 2017), interactive tissue cutting with haptic feedback based in this approach was introduced. In (Qian et al., 2017), a laparoscopic simulator was presented modeled with position based dynamics, in which soft tissues and interactions between them and surgical tools are rendered. The same approach was used in (Camara et al., 2016) to implement a real time simulation platform for robot-assisted partial nephrectomy that allows the interaction of the surgeon with anatomic deformable models.

In sections 2.2.1 and 2.2.2, both geometry based approaches applied to the modeling of the virtual endoscope are explained.

### 2.2.1 Insertion

As aforementioned, the simulation of the insertion movement is performed from the insertion orifice, in which the motion is originated and from where it propagates through the endoscope body. The position based dynamics method was implemented to model the dynamics of the body section (Müller et al., 2007). This graphic approach is based on the modeling of virtual objects using directly positions instead of velocities, in contrast to traditional simulation methods. This approach aims to achieve stability and lower computational load with acceptable visual results.

The algorithm consists of a solver iterator whose objective is to compute the scene

solution that satisfies all the constraints of the points composing the virtual object. In order to fulfill this task, the constraints are repeatedly projected, that is, the corresponding points of this constraint are relocated so as to satisfy the condition. The constraints that have been set in the virtual endoscope model are vertical distance constraints and flexibility degree constraints between adjacent nodes (see Figure 2.6), as well as external collision constraints. However, collision constraints generation and response are performed outside of the solver loop, as suggested in (Müller et al., 2007), obtaining satisfactory results.

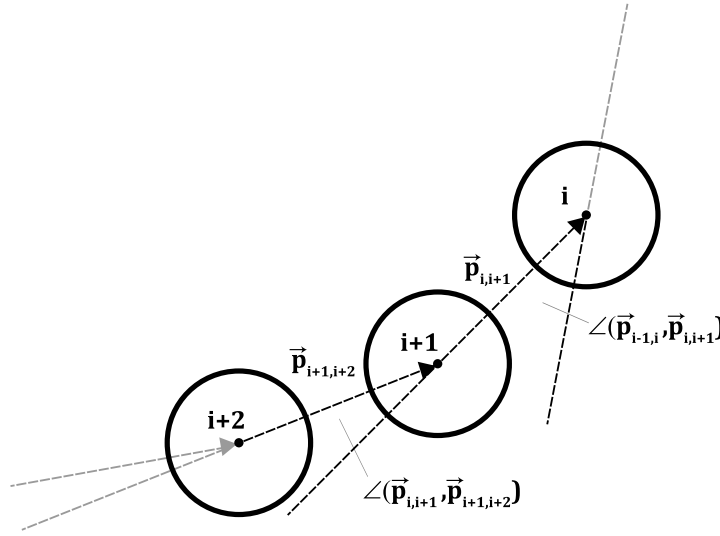


Figure 2.6: Section of the virtual endoscope body implemented: vertical distance constraints and flexibility degree constraints between adjacent nodes.

Let  $C(\vec{p})$  be an equality constraint function over the set of nodes positions  $\vec{p} = [\vec{p}_0^T, \dots, \vec{p}_n^T]^T$ ,  $n \in [0, N - 1]$ .  $N$  is the total number of nodes that represent the virtual discretized model. This equality constraint function is satisfied if  $C(\vec{p}) = 0$ . In order to satisfy the constraint function  $C(\vec{p})$ , a correction  $\Delta\vec{p}$  that makes  $C(\vec{p} + \Delta\vec{p}) = 0$  must be found. This correction can be considered as the displacement of a node trying to satisfy the constraint function. This correction has to be in the direction of  $\nabla_{\vec{p}}C(\vec{p})$  in order to achieve linear and angular momenta conservation if all the nodes have equal masses. This equation can be expressed as

$$C(\vec{p} + \Delta\vec{p}) \approx C(\vec{p}) + \nabla_{\vec{p}}C(\vec{p}) \cdot \Delta\vec{p} = 0 \quad (2.1)$$

$\Delta\vec{p}$  is calculated as

$$\Delta\vec{p} = \lambda \nabla_{\vec{p}}C(\vec{p}) \quad (2.2)$$

where  $\lambda$  is a scalar. By substituting Eq. 2.2 into Eq. 2.1,  $\lambda$  is calculated. Substituting it back into Eq. 2.2, the correction vector is obtained:

$$\Delta \vec{p} = -\frac{C(\vec{p})}{|\nabla_{\vec{p}} C(\vec{p})|^2} \nabla_{\vec{p}} C(\vec{p}) \quad (2.3)$$

The correction vector  $\Delta \vec{p}_i$  for each node  $i$  involved in  $C(\vec{p})$  is

$$\Delta \vec{p}_i = -s \nabla_{\vec{p}_i} C(\vec{p}) \quad (2.4)$$

where  $s = \frac{C(\vec{p})}{\sum_h |\nabla_{\vec{p}_h} C(\vec{p})|^2}$  is the same for all nodes involved in  $C(\vec{p})$ .

If nodes with different masses  $m_i$  are considered, Eq. 2.2 can be expressed as

$$\Delta \vec{p}_i = \lambda w_i \nabla_{\vec{p}_i} C(\vec{p}) \quad (2.5)$$

with  $w_i = 1/m_i$  and the correction vector  $\Delta \vec{p}_i$  for each node  $i$  is

$$\Delta \vec{p}_i = -s w_i \nabla_{\vec{p}_i} C(\vec{p}) = -\frac{C(\vec{p})}{\sum_h w_h |\nabla_{\vec{p}_h} C(\vec{p})|^2} w_i \nabla_{\vec{p}_i} C(\vec{p}) \quad (2.6)$$

For every time step of the simulation, a fixed set of constraint functions is established. It is comprised by vertical distance constraints  $C_D^j(\vec{p}^j)$  ( $j \in [N_T - 1, \dots, N_B - 2]$ ) and flexibility degree constraints  $C_F^k(\vec{p}^k)$  ( $k \in [N_T - 1, \dots, N_B - 3]$ ), being  $N_B$  the number of nodes composing the body and  $N_T$  the number of nodes composing the deflectable tip of the endoscope virtual model. Moreover, a special degree constraint for the joint between the endoscope body and tip was set,  $C_J(\vec{p}^J)$  ( $\vec{p}^J = [\vec{p}_{N_T-2}, \vec{p}_{N_T-1}, \vec{p}_{N_T}]$ ). At each time step, the corrections of nodes positions involved in each constraint function ( $\Delta \vec{p}_i^j$ ,  $\Delta \vec{p}_i^k$  and  $\Delta \vec{p}_i^J$ ) are calculated in a solver iterator which tries to satisfy all the established constraints.

The vertical distance constraint function is

$$C_D^j(\vec{p}^j) = C_D^j(\vec{p}_i^j, \vec{p}_{i+1}^j) = C_D^j(\vec{p}_j, \vec{p}_{j+1}) = |\vec{p}_{j, j+1}| - d \quad (2.7)$$

being  $\vec{p}_{j, j+1} = \vec{p}_j - \vec{p}_{j+1}$  and  $d$  the distance between the nodes with which the constraint is satisfied (see Figure 2.7). The solver iterator projects the constraints from the insertion point of the examined model to the endoscope tip inside the model. It was considered that the nodes outside of the examined model have infinite mass, since all of them have a fixed position controlled by the surgeon.

The gradients with respect to the node positions involved in the constraint are calculated as

$$\nabla_{\vec{p}_j} C_D^j(\vec{p}^j) = \frac{\vec{p}_j - \vec{p}_{j+1}}{|\vec{p}_{j, j+1}|} \quad (2.8)$$

$$\nabla_{\vec{p}_{j+1}} C_D^j(\vec{p}^j) = -\frac{\vec{p}_j - \vec{p}_{j+1}}{|\vec{p}_{j, j+1}|} \quad (2.9)$$

The scaling factor for  $C_D^j(\vec{p}^j)$  is  $s_D^j = \frac{|\vec{p}_{j, j+1}| - d}{w_j + w_{j+1}}$ . Thus, the correction vectors are

$$\Delta \vec{p}_j = -\frac{w_j}{w_j + w_{j+1}} (|\vec{p}_{j, j+1}| - d) \frac{\vec{p}_{j, j+1}}{|\vec{p}_{j, j+1}|} \quad (2.10)$$

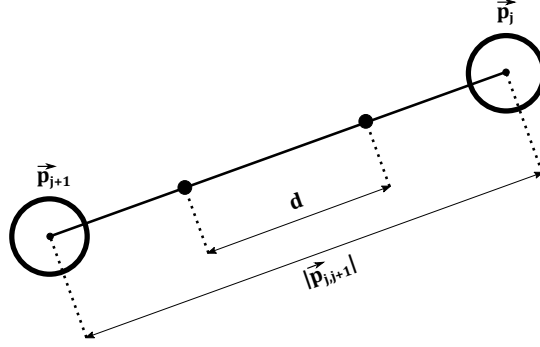


Figure 2.7: Geometric representation of the vertical distance constraint.

$$\Delta \vec{p}_{j+1} = + \frac{w_{j+1}}{w_j + w_{j+1}} (|\vec{p}_{j,j+1}| - d) \frac{\vec{p}_{j,j+1}}{|\vec{p}_{j,j+1}|} \quad (2.11)$$

The flexibility degree constraint function is

$$C_F^k(\vec{p}^k) = C_F^k(\vec{p}_i^k, \vec{p}_{i+1}^k, \vec{p}_{i+2}^k) = C_F^k(\vec{p}_k, \vec{p}_{k+1}, \vec{p}_{k+2}) = \angle(\vec{p}_{k,k+1}, \vec{p}_{k+1,k+2}) - \delta \quad (2.12)$$

being  $\vec{p}_{k,k+1} = \vec{p}_k - \vec{p}_{k+1}$  and  $\vec{p}_{k+1,k+2} = \vec{p}_{k+1} - \vec{p}_{k+2}$  (see Figure 2.8).  $\delta$  represents the angle between the vectors with which the constraint is satisfied.

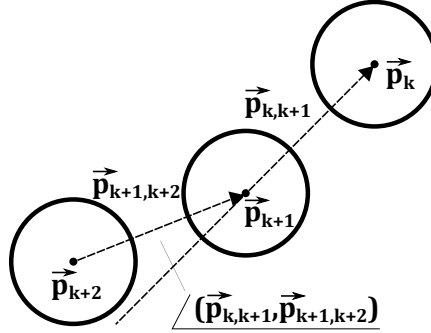


Figure 2.8: Geometric representation of the flexibility degree constraint.

This constraint function can be expressed as

$$C_F^k(\vec{p}_k, \vec{p}_{k+1}, \vec{p}_{k+2}) = \vec{p}_{k,k+1} \cdot \vec{p}_{k+1,k+2} - |\vec{p}_{k,k+1}| |\vec{p}_{k+1,k+2}| \cos \delta \quad (2.13)$$

where the operator  $(\cdot)$  represents the dot product of both vectors. As considered in the vertical distance constraint, the solver iterator projects the constraints from the insertion point to the endoscope tip. Moreover, the nodes outside of the examined model are considered to have infinite mass. The gradients with respect to the node positions involved in the constraint are calculated as

$$\nabla_{\vec{p}_k} C_F^k(\vec{p}^k) = \vec{p}_{k+1,k+2} - \vec{p}_{k,k+1} \frac{|\vec{p}_{k+1,k+2}|}{|\vec{p}_{k,k+1}|} \cos \delta \quad (2.14)$$

$$\nabla_{\vec{p}_{k+1}} C_F^k(\vec{p}^k) = \vec{p}_k - 2\vec{p}_{k+1} + \vec{p}_{k+2} + \vec{p}_{k,k+1} \frac{|\vec{p}_{k+1,k+2}|}{|\vec{p}_{k,k+1}|} \cos \delta - \vec{p}_{k+1,k+2} \frac{|\vec{p}_{k,k+1}|}{|\vec{p}_{k+1,k+2}|} \cos \delta \quad (2.15)$$

$$\nabla_{\vec{p}_{k+2}} C_F^k(\vec{p}^k) = -\vec{p}_{k,k+1} + \vec{p}_{k+1,k+2} \frac{|\vec{p}_{k,k+1}|}{|\vec{p}_{k+1,k+2}|} \cos \delta \quad (2.16)$$

The scaling factor for  $C_F^k(\vec{p}^k)$  is

$$s_F^k = \frac{\vec{p}_{k,k+1} \cdot \vec{p}_{k+1,k+2} - |\vec{p}_{k,k+1}| |\vec{p}_{k+1,k+2}| \cos \delta}{w_k |\nabla_{\vec{p}_k} C_F^k(\vec{p}^k)|^2 + w_{k+1} |\nabla_{\vec{p}_{k+1}} C_F^k(\vec{p}^k)|^2 + w_{k+2} |\nabla_{\vec{p}_{k+2}} C_F^k(\vec{p}^k)|^2} \quad (2.17)$$

Thus, the correction vectors are

$$\Delta \vec{p}_k = -s_F^k w_k \nabla_{\vec{p}_k} C_F^k(\vec{p}^k) \quad (2.18)$$

$$\Delta \vec{p}_{k+1} = -s_F^k w_{k+1} \nabla_{\vec{p}_{k+1}} C_F^k(\vec{p}^k) \quad (2.19)$$

$$\Delta \vec{p}_{k+2} = -s_F^k w_{k+2} \nabla_{\vec{p}_{k+2}} C_F^k(\vec{p}^k) \quad (2.20)$$

The ideal angle between vectors is  $\delta = 0^\circ$ , in order to minimize the total flexion of the endoscope model.

The special degree constraint function for the joint between the endoscope body and the deflectable tip is

$$C_J(\vec{p}^J) = C_J(\vec{p}_{N_T-2}, \vec{p}_{N_T-1}, \vec{p}_{N_T}) = \underline{(\vec{p}_{N_T-2, N_T-1} \times \vec{p}_{N_T-1, N_T}, R_{1x})} - 0^\circ \quad (2.21)$$

being  $\vec{p}_{N_T-2, N_T-1} = \vec{p}_{N_T-2} - \vec{p}_{N_T-1}$  and  $\vec{p}_{N_T-1, N_T} = \vec{p}_{N_T-1} - \vec{p}_{N_T}$ . The operator  $(\times)$  represents the cross product of two vectors. This constraint function can be expressed as

$$\begin{aligned} C_J(\vec{p}_{N_T-2}, \vec{p}_{N_T-1}, \vec{p}_{N_T}) &= (\vec{p}_{N_T-2, N_T-1} \times \vec{p}_{N_T-1, N_T}) \cdot R_{1x} \\ &\quad - |\vec{p}_{N_T-2, N_T-1} \times \vec{p}_{N_T-1, N_T}| |R_{1x}| \cos 0^\circ \\ &= (\vec{p}_{N_T-2, N_T-1} \times \vec{p}_{N_T-1, N_T}) \cdot R_{1x} - |\vec{p}_{N_T-2, N_T-1}| |\vec{p}_{N_T-1, N_T}| \sin(\delta_{ideal}) \end{aligned} \quad (2.22)$$

where the operator  $(\cdot)$  represents the dot product of both vectors, and  $\delta_{ideal}$  is the angle between the corresponding vectors in the ideal shape of the endoscope tip without colliding. The geometric notion behind this constraint function is that the angle between vectors  $\vec{p}_{N_T-2, N_T-1}$  and  $\vec{p}_{N_T-1, N_T}$  has to be the angle between the ideal nodes vectors, calculated in the shape matching algorithm (see Section 2.2.2). Moreover, the vector resulting from the cross product between vectors  $\vec{p}_{N_T-2, N_T-1}$  and  $\vec{p}_{N_T-1, N_T}$  has to be parallel to the  $x$  axis of the local reference frame of the so-called reference node ( $i = N_T - 1$ ) (see Figure 2.9). The rotation of this local reference frame is represented by the rotation matrix  $R_1$  calculated in the shape matching algorithm.

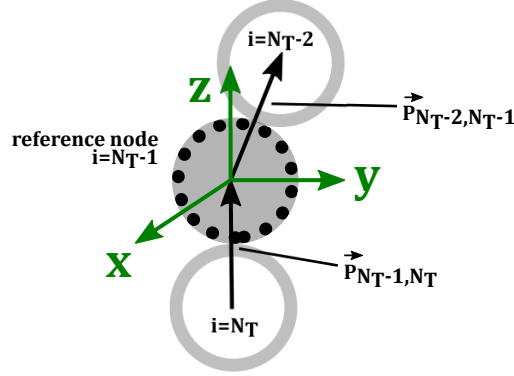


Figure 2.9: Geometric representation of the junction constraint.

Analogously to the previous cases, the gradients with respect to the node positions,  $\nabla_{\vec{p}_{N_T-2}} C_J(\vec{p}^J)$ ,  $\nabla_{\vec{p}_{N_T-1}} C_J(\vec{p}^J)$  and  $\nabla_{\vec{p}_{N_T}} C_J(\vec{p}^J)$ , the scaling factor  $s_J$  and the correction vectors,  $\Delta\vec{p}_{N_T-2}$ ,  $\Delta\vec{p}_{N_T-1}$  and  $\Delta\vec{p}_{N_T}$ , are calculated. In this constraint case, the node in the endoscope tip ( $i = N_T - 2$ ) is considered to have infinite mass so that the shape matching algorithm remains unaltered. This junction constraint between the endoscope body and the tip provides position feedback from the tip to the body when a collision in the deflectable tip occurs.

Once the projected positions  $\vec{p}_i$  have been calculated, the integration scheme implemented was the following

$$\vec{v}_i = \frac{\vec{p}_i - \vec{x}_i}{\Delta t} \quad (2.23)$$

$$\vec{x}_i = \vec{p}_i \quad (2.24)$$

where  $\vec{v}_i$  is the velocity of the  $i$ -th node and  $\vec{x}_i$  is the final position of the  $i$ -th node after the current time step.

### 2.2.2 Flexion and rotation

Both flexion and rotation actuate the deflectable section of the endoscope tip. Dynamics of the tip is modeled using a shape matching algorithm (Müller et al., 2005). At every time step, the tip nodes try to reach previously computed goal positions  $\vec{g}_i$  ( $i \in [0, \dots, N_T - 1]$ , being  $N_T$  the number of nodes composing the deflectable tip of the endoscope virtual model). The goal positions are calculated as

$$\vec{g}_i = R(\vec{x}_i^0 - \vec{x}_{cm}^0) + \vec{x}_{cm} \quad (2.25)$$

where  $\vec{x}_i^0$  are the nodes positions of the ideal shape tip,  $\vec{x}_{cm}^0$  is the center of mass of the ideal shape tip,  $\vec{x}_{cm}$  refers to the center of mass of the actual shape, and  $R$  is a 3x3 rotation matrix that has to be computed every time step.

In order to efficiently calculate the goal positions  $\vec{g}_i$  at every time step, the scheme depicted in Figure 2.10 is followed. The so-called reference node ( $i = N_T - 1$ ) is considered to have infinite mass and acts like a reference for locating the remaining

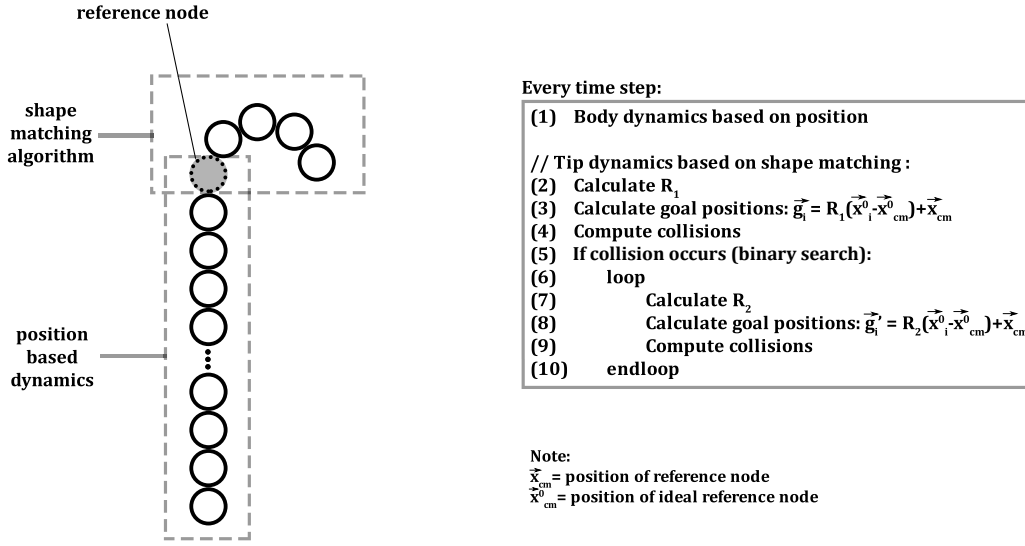


Figure 2.10: Simplified scheme followed for the flexion and rotation graphical computation.

tip nodes, whose masses are finite. The position of the reference node is previously determined by the position based dynamics algorithm, since it is also considered as part of the endoscope body. This method ensures that the tip will always be attached to the flexible body. Thus, the center of mass of the actual shape  $\vec{x}_{cm}$  can be considered as the reference node position ( $\vec{x}_{cm} = \vec{x}_{N_T-1}$ ). Likewise, the center of mass of the ideal shape  $\vec{x}_{cm}^0$  is the position of the ideal reference node ( $\vec{x}_{cm}^0 = \vec{x}_{N_T-1}^0$ ). The rotation matrix  $R_1$  represents the local rotation of the reference node. The rotation matrix  $R_2$  is computed when penetration of the deflectable tip into external objects occurs.

In order to compute the rotation matrix  $R_2$ , external collisions of the endoscope tip with environment objects are taken into account. When the tip penetrates an external object at a time step, the developed algorithm recursively iterates to find a final position where the tip nodes are located inside the object surface, maintaining the endoscope tip shape. This algorithm is based on a balanced binary search tree paradigm, in order to reduce the number of iterations (see Figure 2.11). The algorithm minimizes the distance between the penetrating tip position and the final tip position, preserving the initial shape of the tip at the current time step.

The ideal nodes positions  $\vec{x}_i^0$  are calculated by applying forward kinematics of the flexible ureteroscope tip (Zhang et al., 2014). The model considers a discretized endoscope. The position  $\vec{x}_i^0 (i \in [0, \dots, N_T - 2])$  of the ideal node  $i$  can be calculated as

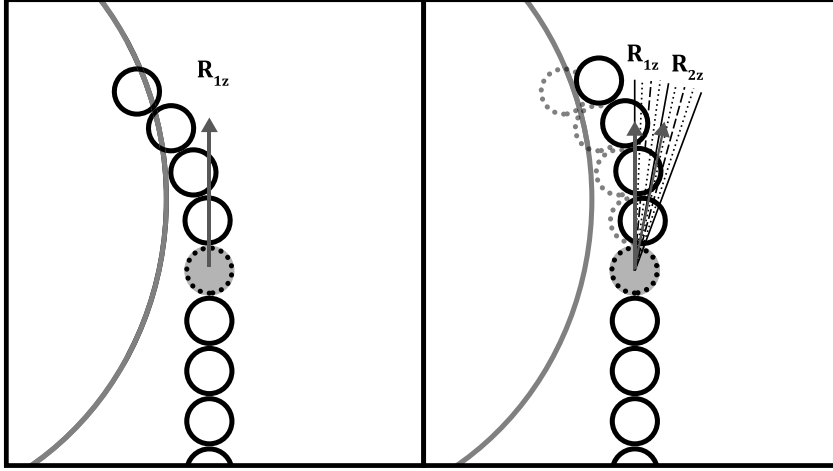


Figure 2.11: Simplified example of the implemented algorithm based on a binary search principle to compute the rotation matrix  $R_2$ , with a balanced binary tree of four levels.

$$\vec{x}_i^0 = \begin{bmatrix} \vec{x}_{ref}^0 \cdot x \\ \vec{x}_{ref}^0 \cdot y + R(1 - \cos(\alpha - i\beta)) \\ \vec{x}_{ref}^0 \cdot z + R \sin(\alpha - i\beta) \end{bmatrix} \quad (2.26)$$

where  $\beta = \frac{\alpha}{N_T - 1}$ ,  $R = \frac{L}{\alpha}$ ,  $N_T$  is the number of nodes composing the virtual endoscope tip,  $\alpha$  the flexion degree ( $0 < \alpha < 270$ ),  $L$  the length of the distal tip and  $\vec{x}_{ref}^0$  the known position of the ideal reference node ( $\vec{x}_{ref}^0 = \vec{x}_{N_T - 1}^0$ ).

The ideal nodes positions  $\vec{x}_i^0$  are recomputed every time the flexion degree of the endoscope tip ( $\alpha$ ) is reconfigured by the user interaction.

Once the goal positions  $\vec{g}_i$  have been calculated, the integration method implemented was the following modified Euler scheme

$$\vec{v}_i(t + \Delta t) = \vec{v}_i(t) + \gamma \frac{\vec{g}_i(t) - \vec{x}_i(t)}{\Delta t} \quad (2.27)$$

$$\vec{x}_i(t + \Delta t) = \vec{x}_i(t) + \Delta t \vec{v}_i(t + \Delta t) \quad (2.28)$$

where  $\vec{v}_i$  is the velocity of the  $i$ -th node,  $\vec{x}_i$  is the position of the  $i$ -th node and  $\gamma$  is a parameter which simulates the stiffness of the object ( $0 \leq \gamma \leq 1$ ). The higher value of  $\gamma$ , the higher stiffness the object presents.

## 2.3 Algorithm implementation

The virtual system was developed using the C++ simulation framework CHAI3D (CHAI3D, 2018), an open-source and multiplatform environment designed to integrate tactile and visual sensations in real time. It uses the OpenGL framework for 3D graphic rendering. CHAI3D includes several libraries for computer haptics,

visualization and interactive real-time simulation, which make it a very useful platform for developing the integration of virtual environments with force feedback.

As shown in Figure 2.12, the basic architecture is composed of two different periodic tasks: the computational and the graphic rendering. The computational task has to calculate, at every time step, the final positions of the nodes of the virtual flexible ureteroscope and capture the user interaction inputs. The graphic rendering task has the objective of updating the visual scene.

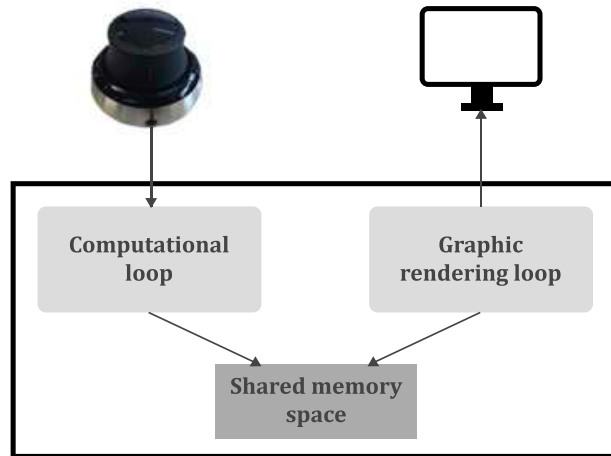


Figure 2.12: Basic architecture of the developed simulation program.

Both tasks are handled by two POSIX threads with different priorities. The computational loop is assigned the highest priority, because the execution of this task, which involves user interaction, requires the highest possible frequency. On the other side, the graphic rendering task is assigned a lower priority. The minimum frequency required for this graphic update is 25 fps.

### 2.3.1 Collision detection

The collision detection method must notify whether two objects are intersecting during the simulation. In the case of the developed training platform, the collision approach has to detect which nodes are penetrating external objects at each time step. The collision detection method implemented provided by the CHAI3D framework is based on an axis aligned bounding box hierarchy. In this approach, virtual objects are wrapped into basic shapes in order to quickly check intersection between them. Particularly in this case, axis aligned bounding boxes (AABB) are used (Weller, 2013). Therefore, objects are organized creating a hierarchical tree topology. Small objects are wrapped in different bounding boxes and then in larger bounding volumes that contain other wrapped objects. In the final tree, each node is linked to a bounding volume that wraps all primitives of children nodes (see Figure 2.13). When detecting

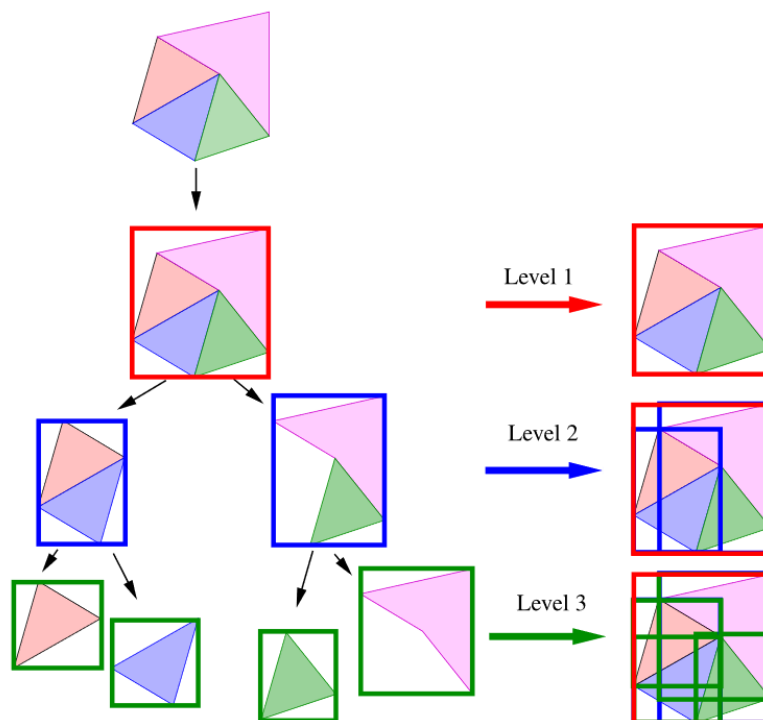


Figure 2.13: Basic principle of the bounding box hierarchy (Weller, 2013).

collision in a bounding volume hierarchical tree, intersection between an endoscope node and the object root node is checked. If intersection occurs in a node, its children nodes are then examined. This procedure is recursively performed until the intersected primitive is determined. Children nodes of bounding volumes that do not intersect are not checked. With this method, the complexity of the detection algorithm may be reduced.

Figure 2.14 shows the AABB based collision detector implemented for the training platform. Only nodes of depth 4 are depicted in the figure. Maximum depth of the created hierarchical tree for the three-dimensional ureterorenal model was 19.

### 2.3.2 Collision response

Regarding the collision response method used for the endoscope body collisions, the force rendering approach “finger-proxy” of the CHAI3D framework was applied to the implemented graphic algorithm (Ruspini et al., 1997). This force model is based on the idea of a virtual proxy that represents the real cursor movements towards a goal. This virtual proxy presents the same behaviour as a real pointer would have in real life; while haptic exploration, it does not penetrate external objects and lies on their surface during collisions. In free space, both proxy and goal positions are the same. When an external object avoids proxy direct motion to the goal, the algorithm tries to reduce the distance between the two points, moving the proxy along the object

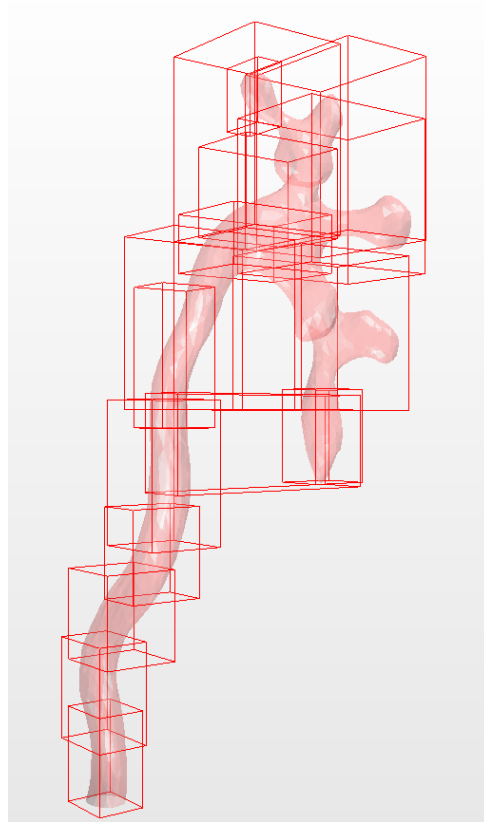


Figure 2.14: Nodes of depth 4 in the axis aligned bounding box hierarchical tree of the implemented three-dimensional ureterorenal model.

external surfaces until it reaches a position with the lower possible distance to the goal (see Figure 2.15). The proxy is considered as a point that can be moved inside the configuration space composed of the configuration-space obstacles, which consist of all points within one proxy radius of the original object surfaces (see Figure 2.16).

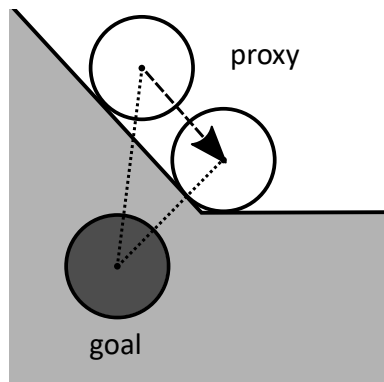


Figure 2.15: The “finger-proxy” algorithm tries to reduce the distance between the proxy and goal positions.

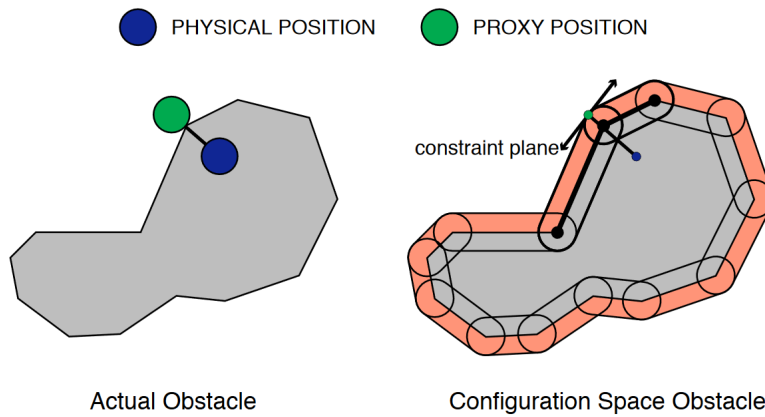


Figure 2.16: Configuration space obstacles and constraint planes (Ruspini et al., 1997).

This principle can be written as an optimization problem as follows

$$\begin{aligned}
 & \text{minimize } \|\vec{x} - \vec{p}\| \text{ subject to} \\
 & \quad \vec{n}_1^T x \leq 0, \\
 & \quad \vec{n}_2^T x \leq 0, \\
 & \quad \dots \\
 & \quad \vec{n}_m^T x \leq 0.
 \end{aligned} \tag{2.29}$$

where  $\vec{p}$  is the difference vector between the proxy position and the real user's position,  $\vec{x}$  is the new proxy position that has to be solved, and  $\vec{n}_i^T$ ,  $0 \leq i \leq m$ , are the unit normals of the constraint planes built around the object surfaces.

Although the computational cost of this algorithm is higher than other alternative methods, like the potential field model, it solves some limitations like discontinuities in the object surface or pop-through of thin objects (Zilles and Salisbury, 1995).



## CHAPTER

# 3

## FORCE FEEDBACK

### 3.1 Introduction to the developed haptic system

Traditional open surgery allows direct tissue examination by touching. However, tactile and kinesthetic information perceived by the surgeons decreases when they manipulate the tissues using surgical instruments and tools to perform minimally invasive interventions. Several recently developed surgical robots incorporate force and tactile feedback, with the main objective of reducing the loss of haptic feedback related to most of conventional minimally invasive interventions. In order to increase the tactile perception and the immersion of the surgeon in the urologic procedure carried out in the developed virtual reality platform, a haptic system was designed and implemented to provide force feedback to the specialist.

The developed haptic device provides 3 DOF input and output for the control of the 3 DOF of the endoscope (insertion, rotation and flexion). This means that the position of the 3 DOF manipulators can be read and forces in these 3 DOF can be provided to the user. The haptic device that has been implemented is composed of two different controllers, one for each hand, following the surgeons feedback provided on the design phase (see Section 2.1). The location of each subsystem depends on the surgeon preferences:

- The haptic controller 1 provides 1 DOF for the manipulation of the endoscope tip flexion, as well as the activation button for the lithotripsy laser.
- The haptic controller 2 provides 2 DOF for the control of the endoscope insertion and rotation.

For the development of a force feedback loop between the implemented virtual reality training platform and the developed haptic device, the following procedure

is executed. Firstly, the position of the controllers is sent to the simulator. This position directly controls the location of the final virtual end effector, constituted by the deflectable endoscope tip. The new location of the endoscope is then rendered in the virtual environment. Computation of the exerted virtual forces on the endoscope tip is performed. The final forces are finally sent back to the corresponding haptic controller, which provides the force feedback to the user. This impedance force closed loop can be observed in Figure 3.1. In order to ensure the stability of the haptic loop, the minimum execution rate must lie in the range of 500-1000Hz.

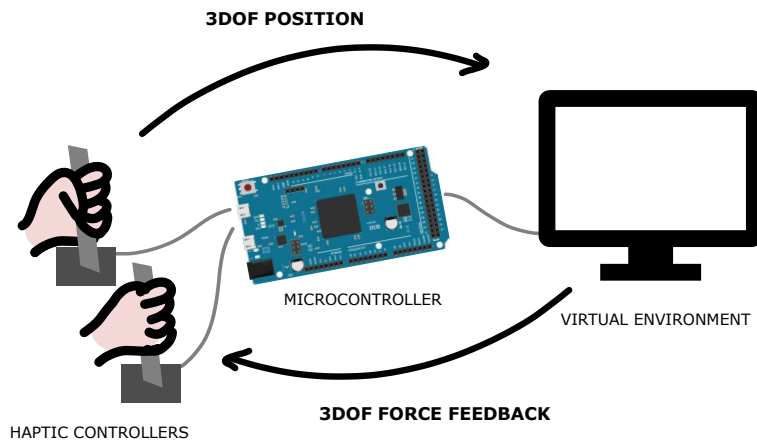


Figure 3.1: Simplified scheme of the developed impedance force closed loop.

The haptic controllers are the physical interface that enables the user to interact with the virtual environment. The haptic manipulators are mechatronic systems that include mechanical parts and electronic components. They have two different functions: sending location to the virtual environment and exerting computed forces to the user. Therefore, as every haptic system, they are comprised of sensors and actuators. The hardware system of the haptic controllers is composed of the following electronic components:

- A microcontroller board Arduino Due based on the Atmel SAM3X8E ARM Cortex-M3 CPU (32 bits) <sup>1</sup>.
- Three direct current (DC) brushed electric motors provided by gearheads and optical/magnetic encoders: two Faulhaber DC Gearmotors 2619S012SR<sup>2</sup> with a reduction ratio of 22:1 and an IE2-16 encoder for insertion and flexion endoscope control and one Faulhaber DC Micromotor 1516E012SR<sup>3</sup> with a reduction ratio of 41:1 and an IE2-16 encoder for the rotation of the endoscope.

<sup>1</sup><https://store.arduino.cc/usa/arduino-due>

<sup>2</sup>[https://www.faulhaber.com/fileadmin/Import/Media/EN\\_2619\\_SR\\_IE2-16\\_DFF.pdf](https://www.faulhaber.com/fileadmin/Import/Media/EN_2619_SR_IE2-16_DFF.pdf)

<sup>3</sup>[https://www.faulhaber.com/fileadmin/Import/Media/EN\\_1516\\_SR\\_DFF.pdf](https://www.faulhaber.com/fileadmin/Import/Media/EN_1516_SR_DFF.pdf)

- Two X-NUCLEO-IHM04A1 dual brush DC motor drive expansion boards<sup>4</sup> based on the DMOS dual full bridge L6206<sup>5</sup>.
- A tactile DIP push button for the activation of the lithotripsy laser, whose signal is correctly low pass filtered to prevent switch bounces.

In this haptic system, the push button and the optical/magnetic encoders act as sensors. They have the function of sensing the position of the motor shaft or the activation of the laser. On the other hand, DC motors work as actuators, providing the computed final forces to the surgeon.

In the following Section 3.2, characterization of the electronics components of the force feedback system is discussed. In Section 3.3, the integration of the final hardware system with the virtual endoscope model is explained.

## 3.2 Hardware architecture description

### 3.2.1 DC motors

As stated in Section 3.1, two Faulhaber DC Gearmotors 2619S012SR 22:1 + IE2-16 are used for the insertion and flexion degrees of freedom. These motors include an integrated optical encoder of 2 channels and 16 lines per revolution. The gearbox has a reduction ratio of 22:1. Therefore, 1408 pulses are provided in a revolution out of the gearbox. This means that the resolution per pulse is 0.256 degrees. Table 3.1 presents the characteristics of these motors, provided by the manufacturer datasheet (see Appendix C).

Parameter	Value	Units
Nominal voltage $U_N$	12	V
Terminal resistance $R_m$	31.5	$\Omega$
Rotor inductance $L_m$	$1600 \times 10^{-6}$	H
Rotor inertia $J_m$	$0.68 \times 10^{-7}$	$kg\ m^2$
Mechanical time constant $t_m$	$7.9 \times 10^{-3}$	s
Electrical time constant $t_e$	$5.13 \times 10^{-5}$	s
Back-EMF constant $k_b$	$16.4 \times 10^{-3}$	Vs/rad
Torque constant $k_m$	$16.4 \times 10^{-3}$	Nm/A

Table 3.1: Parameters of Faulhaber DC Gearmotors 2619S012SR 22:1 + IE2-16 (see Appendix C).

The electrical and mechanical time constants are calculated as  $t_e = L_m/R_m$  and  $t_m = R_m \times J_m/k_m^2$ .

<sup>4</sup><http://www.st.com/en/ecosystems/x-nucleo-ihm04a1.html>

<sup>5</sup><https://www.st.com/en/motor-drivers/l6206.html>

From Table 3.1, the analytical model of the motor is calculated (Félix Monasterio-Huelin & Álvaro Gutiérrez, 2018). The transfer function in angular velocity of a DC motor is

$$G_{\dot{\theta}_m}(s) = \frac{K'_m}{(s + |p_1|)(s + |p_2|)} \quad (3.1)$$

where

$$K'_m = \frac{k_m}{J_m L_m} \quad (3.2)$$

$$p_{1,2} = -\frac{1}{2} \left( \frac{1}{t_e} + \frac{1}{t'_m} \right) \pm \frac{1}{2} \sqrt{\left( \frac{1}{t_e} - \frac{1}{t'_m} \right)^2 - 4 \frac{k_m k_b}{J_m L_m}} \quad (3.3)$$

and  $t'_m = \frac{J_m}{B_m}$ . The viscous friction coefficient is estimated as  $B_m = \frac{J_m}{t'_m} - \frac{k_b k_m}{R_m}$ .

Therefore, the transfer function in angular velocity of the motor is

$$G_{\dot{\theta}_m}^1(s) = \frac{K'_m}{(s + |p_1|)(s + |p_2|)} = \frac{150735294.12}{(s + 19372.39)(s + 127.61)} \quad (3.4)$$

This transfer function can be simplified if the electrical time constant is very small in comparison to the mechanical time constant. Therefore, the transfer function in angular velocity of the DC motor can be expressed as

$$\tilde{G}_{\dot{\theta}_m}^1(s) = \frac{K_m}{(s + p_m)} = \frac{7730}{(s + 126.77)} \quad (3.5)$$

where  $K_m = p_m G_{\dot{\theta}_m}^1(0) = p_m \frac{k_m}{R_m B_m + k_b k_m}$  and  $p_m = 1/t_m$ . The module of the calculated transfer function  $|G_{\dot{\theta}_m}^1(s)|$  and its simplification  $|\tilde{G}_{\dot{\theta}_m}^1(s)|$  are depicted in Figure 3.2.

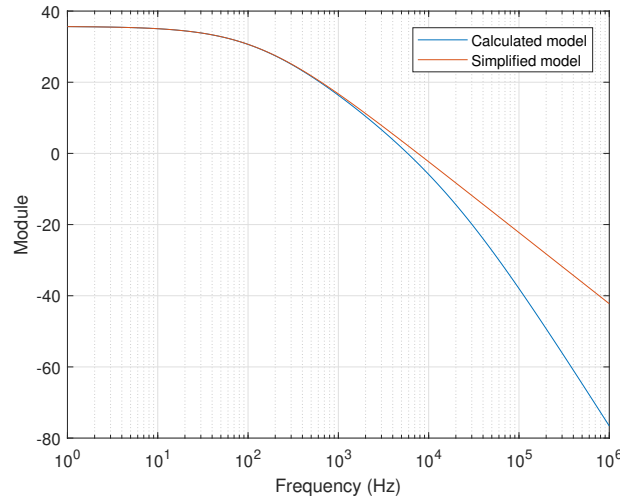


Figure 3.2: Module of the transfer function in angular velocity of the motor for insertion and flexion.

For the rotation endoscope control, one Faulhaber DC Micromotor 1516E012SR + 16A 41:1 + IE2-16 is used, as stated in Section 3.1. The encoder of this motor is magnetic, and it is composed of 2 channels and 16 lines per revolution. The gearbox has a reduction ratio of 41:1. Therefore, 2624 pulses are provided in a revolution out of the gearbox. This means that the resolution per pulse is 0.137 degrees. Table 3.2 presents the characteristics of this motor, provided by the manufacturer datasheet (see Appendix D).

Parameter	Value	Units
Nominal voltage $U_N$	12	V
Terminal resistance $R_m$	115	$\Omega$
Rotor inductance $L_m$	$900 \times 10^{-6}$	H
Rotor inertia $J_m$	$0.23 \times 10^{-7}$	kg m <sup>2</sup>
Mechanical time constant $t_m$	$60 \times 10^{-3}$	s
Electrical time constant $t_e$	$7.83 \times 10^{-6}$	s
Back-EMF constant $k_b$	$6.61 \times 10^{-3}$	Vs/rad
Torque constant $k_m$	$6.61 \times 10^{-3}$	Nm/A

Table 3.2: Parameters of Faulhaber DC Micromotor 1516E012SR + 16A 41:1 + IE2-16 (see Appendix D).

The electrical time constant is calculated as  $t_e = L_m/R_m$ .

Analogously to the previous motors, the analytical model of this motor is calculated by using the data of Table 3.2. The calculated transfer function in angular velocity of the DC motor is

$$G_{\dot{\theta}_m}^2(s) = \frac{K_m'}{(s + |p_1|)(s + |p_2|)} = \frac{319323671.5}{(s + 127761.26)(s + 16.67)} \quad (3.6)$$

This transfer function can be simplified if the electrical time constant is very small in comparison to the mechanical time constant. Therefore, the transfer function in angular velocity of the DC motor can be expressed as

$$\tilde{G}_{\dot{\theta}_m}^2(s) = \frac{K_m}{(s + p_m)} = \frac{2499.055}{(s + 16.67)} \quad (3.7)$$

where  $K_m = p_m G_{\dot{\theta}_m}^2(0) = p_m \frac{k_m}{R_m B_m + k_b k_m}$  and  $p_m = 1/t_m$ . The module of the calculated transfer function  $|G_{\dot{\theta}_m}^2(s)|$  and its simplification  $|\tilde{G}_{\dot{\theta}_m}^2(s)|$  are depicted in Figure 3.3.

### 3.2.2 DC motor driver

The nominal voltage required for the properly functioning of the used DC motors is 12V, specified in Tables 3.1 and 3.2. However, the microcontroller board Arduino Due is able to output only 3.3V through the I/O pins, providing also a very low maximum

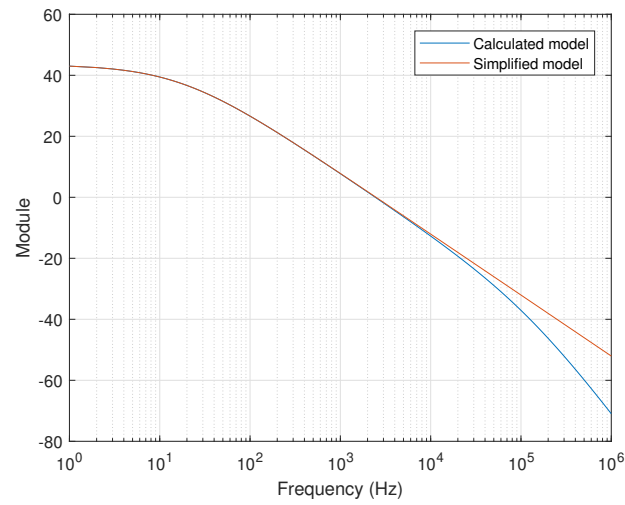


Figure 3.3: Module of the transfer function in angular velocity of the motor for rotation.

output current that is not enough to drive the DC motors (15mA). Therefore, a DC motor driver is needed in order to correctly control the DC motors. Since three different motors have to be controlled, two X-NUCLEO-IHM04A1 dual brush DC motor drive expansion boards are used. These expansion boards are based on the DMOS dual full bridge L6206. They allow the control of the rotation speed and the rotation direction. This is performed by the pulse width modulation (PWM) of four DMOS transistors, that are assembled in a special electronic configuration called H bridge (see Figure 3.4). This circuit allows the activation of both transistors  $Q1$  and

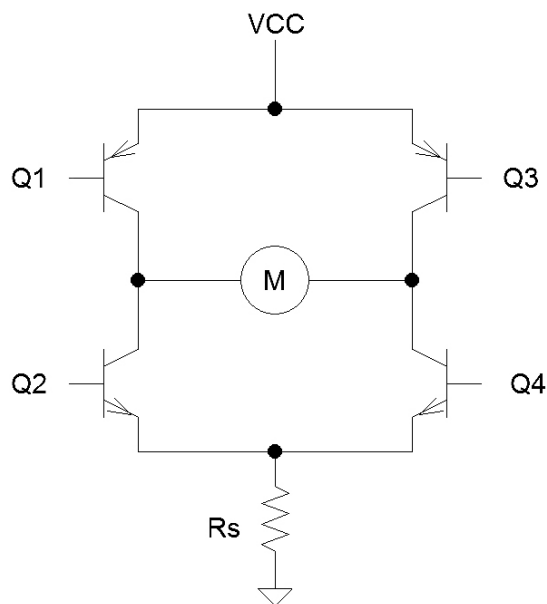


Figure 3.4: Simplified H bridge circuit.

Q1	Q2	Q3	Q4	State
ON	OFF	OFF	ON	Motor runs clockwise
OFF	ON	ON	OFF	Motor runs counter-clockwise
ON	OFF	ON	OFF	Motor brakes
OFF	ON	OFF	ON	Motor brakes
OFF	OFF	OFF	OFF	Motor coasts

Table 3.3: Possible states of the H bridge configuration with a DC motor.

$Q4$  while transistors  $Q2$  and  $Q3$  are in cutoff mode, applying a positive voltage to the motor. This voltage is reversed when transistors  $Q2$  and  $Q3$  are activated and transistors  $Q1$  and  $Q4$  are in cutoff mode. This configuration allows the motor to run forwards and backwards by digital control, without performing assembling changes. Depending on the signals applied to the transistors, the motor can run clockwise, counter-clockwise, brake or coast (freely run). The possible H bridge states can be observed in Table 3.3.

The signals applied to the DMOS transistors are PWM signals. The speed of the motor is controlled by the duty cycle of these PWM signals. The signals applied to the transistors are generated by the Arduino Due by correctly configuring the Peripheral B and selecting the signal frequency and duty cycle. The chosen modulation frequency is 40kHz, which is adequately attenuated by both types of motors (see Figures 3.2 and 3.3).

### 3.2.3 Mechanical design of the haptic system

The development of the mechanical part of the haptic system was performed by 3D printing. 3D printing technology is becoming more and more popular in the recent years. This additive manufacturing process allows the user to produce custom products at low costs with readily available supplies. Moreover, it facilitates and speeds up the development and modification of model designs. However, it has also some limitations, such as not enough precision required to some applications, reduced choice for materials or surface finishes, and limited strength or resistance to heat (Berman, 2012). For the objective of this project, 3D printing technology meets the expected requirements for the development of a first prototype, although other technologies may be required for advanced versions.

The CAD models for the final pieces were firstly designed with the 3D design and modeling software Autodesk 123D. Then, the pieces were printed with a 3D printer Prusa i3 Hephestos<sup>6</sup>. The printed pieces were assembled with the electronic components and validated. Several prior designs of the haptic controllers were previously developed and tested until the final versions for these haptic prototypes were achieved. The mechanical design and assembly of the haptic controllers

<sup>6</sup>[https://reprap.org/wiki/Prusa\\_i3\\_Hephestos/es](https://reprap.org/wiki/Prusa_i3_Hephestos/es)

prototypes were developed following the steps depicted in the flowchart of Figure 3.5.

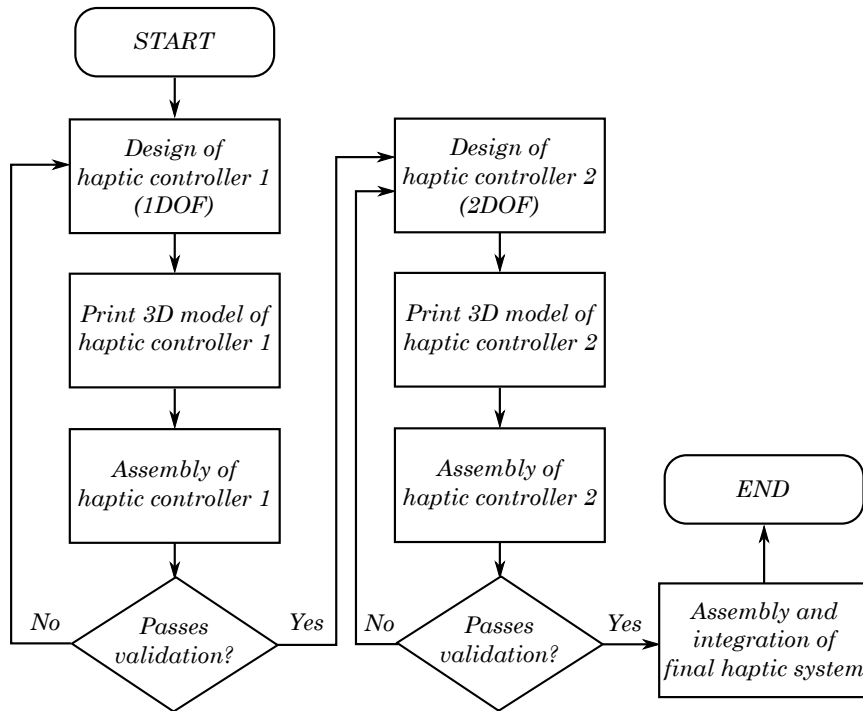


Figure 3.5: Flowchart of the design and assembly process of the final haptic system.

Final results of design and assembly steps of the haptic controller 1 are shown in Figures 3.6a, 3.6c and 3.6e. Final results of design and assembly steps of the haptic controller 2 are presented in Figures 3.6b, 3.6d and 3.6f. The final integrated mechatronic system assembled in the final step can be observed in Figure 3.7.

The fabrication of these custom prototypes of the haptic controllers enables the study and validation of the developed training platform with the implemented degrees of freedom providing force feedback. The validation phase is explained in Chapter 4. In Section 3.3, the integration of the final mechatronic system with the virtual reality simulator is addressed.

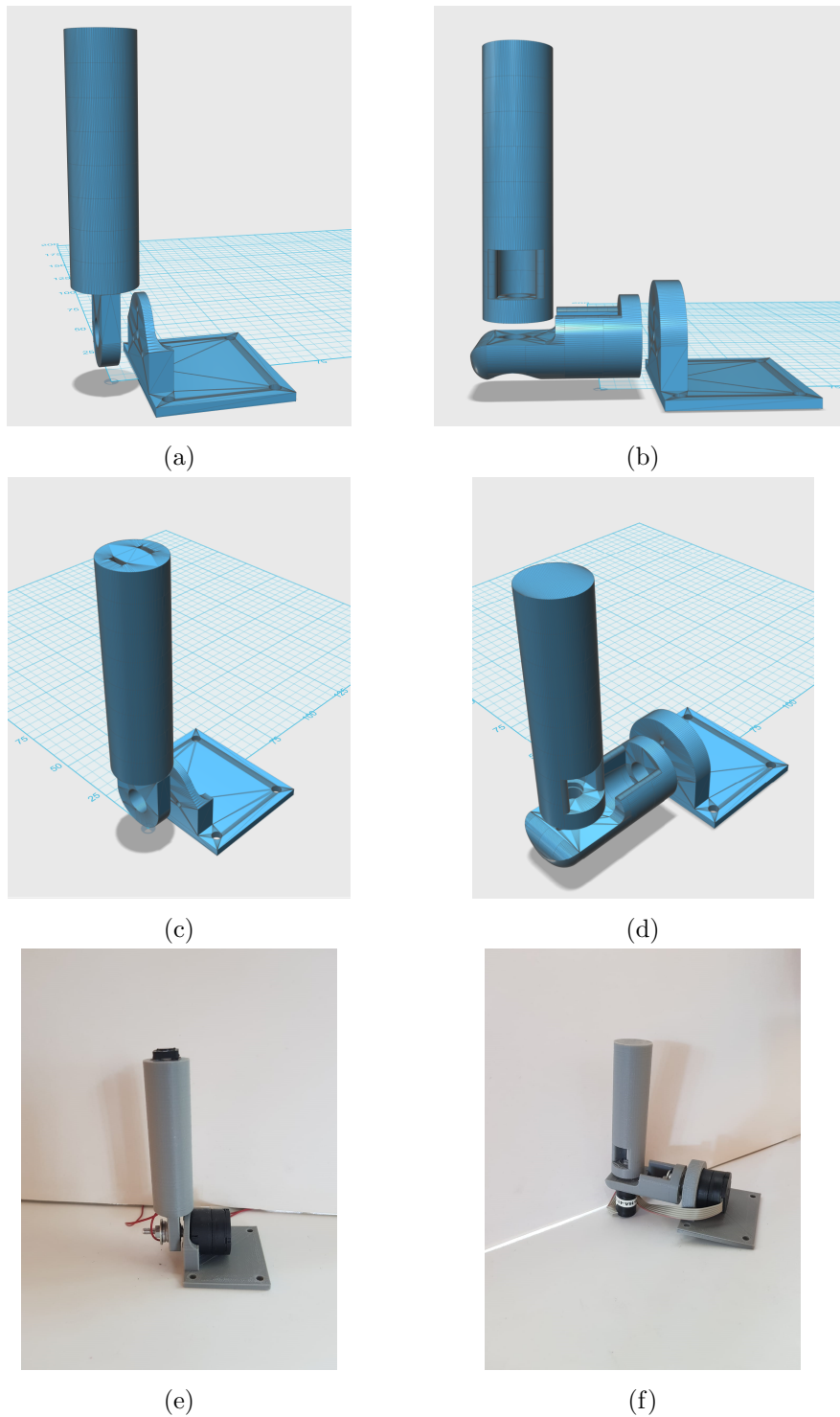


Figure 3.6: On the left, final designed 3D CAD model for controller 1 (a and c) and final 3D printed and assembled haptic controller 1 (e). On the right, final designed 3D CAD model for controller 2 (b and d) and final 3D printed and assembled haptic controller 2 (f).

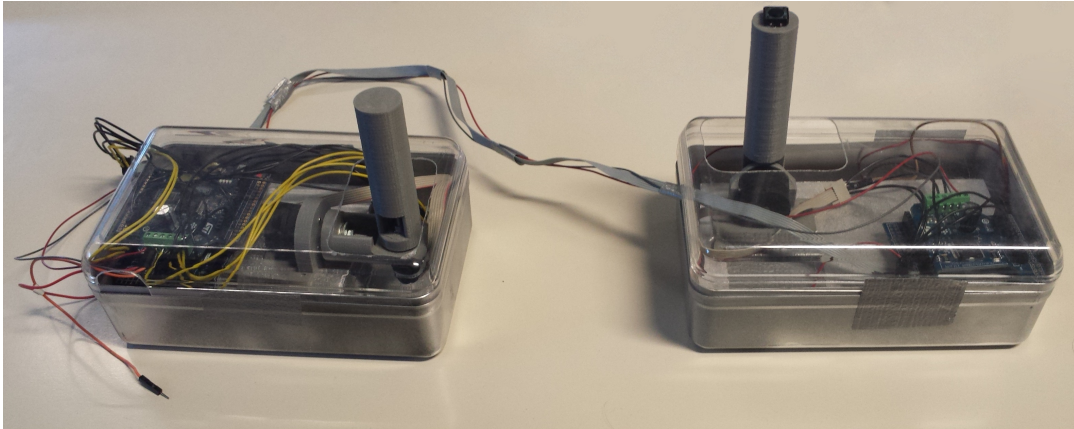


Figure 3.7: Final mechatronic system.

### 3.3 Integration with the training platform

For the integration of the developed training platform with the haptic controllers, an impedance force closed loop between both systems was implemented. The position of the controllers sensed by the motor encoders is sent from the mechatronic system to the virtual platform using the Arduino Due. This position directly controls the location of the deflectable endoscope tip. The new position of the virtual endoscope is then rendered in the simulated environment. After that, the exerted virtual forces on the endoscope tip during the movement are computed. Finally, the calculated forces are sent back to the Arduino Due, which activates the corresponding DC motor in the haptic controllers to provide the force feedback to the surgeon. The magnitude of the exerted force, controlled by the duty cycle of the PWM signals applied to the DC motor, is proportional to the force calculated in the virtual environment. The different steps of this haptic loop can be observed in the flowchart of Figure 3.8.

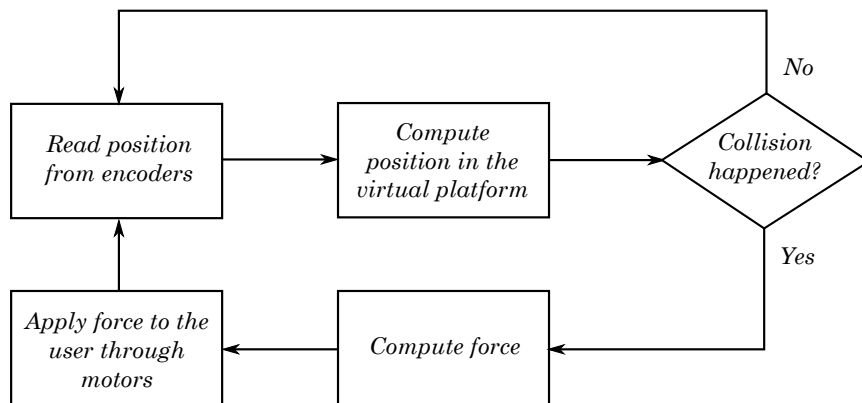


Figure 3.8: Flowchart of the implemented haptic loop.

The communication between the haptic controllers and the virtual reality platform, which is running in a computer, is performed by the Arduino Due. The Arduino Due is connected to the CPU by the serial port. The C++ program opens an available serial port to read and write data through it. In order to reduce the amount of time spent in the communication, the configured baud rate is 115200 bits/s, for both reading and writing. The frames of bits are composed by 8 data bits without parity bits. The range of motion of the haptic controllers for the insertion and flexion degrees of freedom is  $\varphi \in (-58.8, 58.8)^\circ$ , whereas the range of motion of the rotation control is  $\rho \in (0, 360)^\circ$  (see Figure 3.9). The number of different positions in the range considering the resolution of the motors encoders can be observed in Table 3.4, in which the required number of bits for the communication is also stated. Therefore, 2 bytes per degree of freedom have to be transmitted from the Arduino Due to the computer. In addition, an identifier consisting of 2 bits for the three DC motors is used in the transmission. The first 2 bits of each data byte are reserved for the identifier (see Figure 3.10).

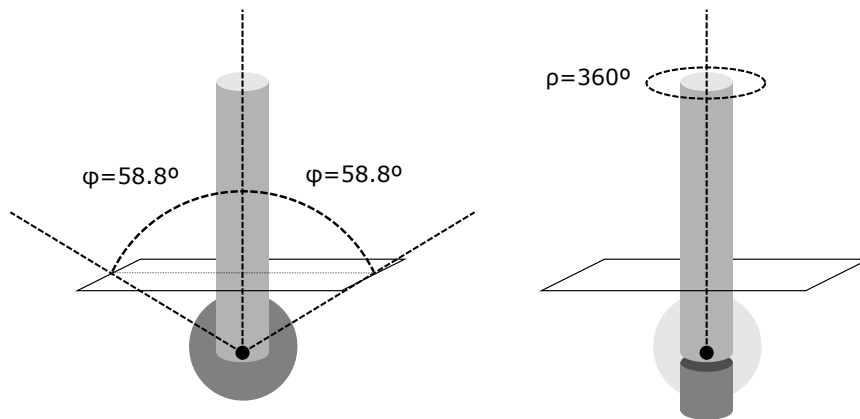


Figure 3.9: Range of motion of insertion and flexion control (left) and rotation (right).

	Range of motion ( $^\circ$ )	Encoder resolution (pulses/rev)	Number of pulses in range	Bits required
Insertion and flexion	117.6	1408	456	9
Rotation	360	2624	2624	12

Table 3.4: Required number of bits for transmission.

The received position information is translated into movement of the virtual endoscope. The computed force in the virtual platform with the new position is then transmitted to the Arduino Due, which applies the proportional signal to

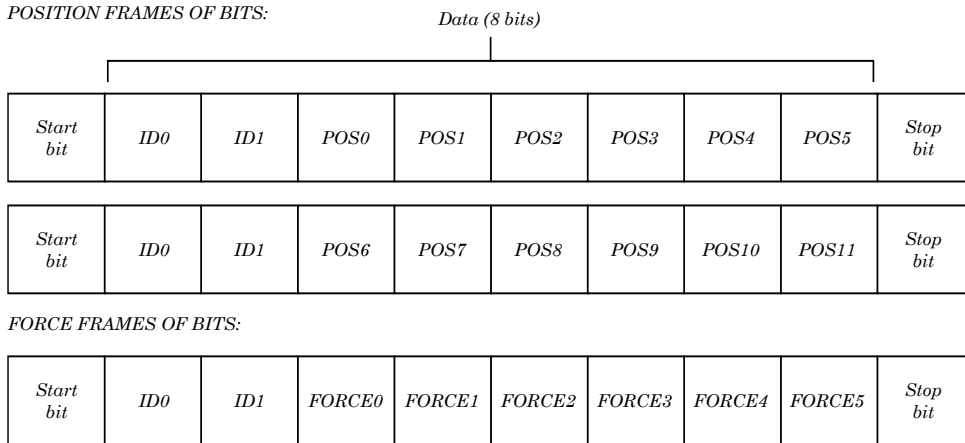


Figure 3.10: Frames of bits for the serial communication used for position (up) and force (down) transmission.

the corresponding motor of the haptic controllers. One byte is used for the force communication, where the first 2 bits are used as identifier of the three DC motors, and the following 6 bits are used to send the computed force (see Figure 3.10).  $2^6 = 64$  different forces can be provided to the user.

The control architecture developed is based on a virtual spring implemented in the haptic controllers, particularly in the insertion and flexion degrees of freedom. This allows relative motion of the haptic controllers, returning to the resting position once the user stops manipulating them. Moreover, the computed force is added to the spring model, resulting in the control scheme of Figure 3.11. For the rotation degree of freedom, no virtual spring model was implemented, since the complete range of motion matches the possible rotation of the virtual endoscope. In the developed control scheme, the error signal  $e(t)$  obtained from the subtraction of the resting

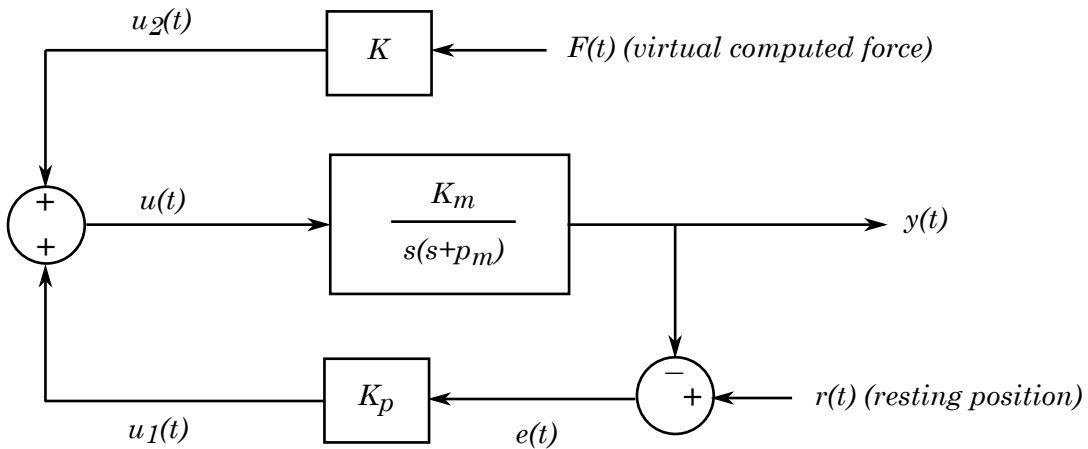


Figure 3.11: Control architecture for the integration of force feedback in the virtual platform.

reference position  $r(t)$  and the current position of the motor  $y(t)$  is used for the virtual spring model, achieved with the proportional control of the motor. The signal  $u(t)$  represents the total control signal in [Volts] applied to the motor, resulting from the sum of the individual control signals  $u_1(t)$  and  $u_2(t)$ . The signal  $u_1(t)$  is the control signal obtained from the proportional control of the motor, using the proportional constant  $K_p$ , that is expressed in the units  $[\frac{Volts}{rad}]$ . The signal  $u_2(t)$  is the control signal calculated with the virtual force from the simulation, using the experimental constant  $K$ , expressed in the units  $[\frac{Volts}{N}]$ . Thus, the following relations are obtained:

$$e(t) = r(t) - y(t) \quad (3.8)$$

$$u_1(t) = K_p \cdot e(t) \quad (3.9)$$

$$u_2(t) = K \cdot F(t) \quad (3.10)$$

$$u(t) = u_1(t) + u_2(t) \quad (3.11)$$

However, when implementing this scheme, several limitations were encountered. The minimum voltage signal that has to be applied to activate the used DC motors is not negligible. This means that these motors provide a deadband in which the signal applied is not high enough to move the rotor of the motor due to the internal torque. This leads to a dead angle range that does not allow the haptic controller to reach the resting position when external motion ceases. This effect may deteriorate the user experience.

One possible solution to this problem is the increase of the proportional constant  $K_p$  in the virtual spring model. With this solution, the dead angle range decreases. However, the total range of motion of the haptic controller also decreases, since higher opposite forces are applied with smaller difference angles. Another solution that was tested is the use of a different DC motor which provides a smaller deadband due to internal torque. The DC motor used was the A-max 32 - 12V<sup>7</sup> with a planetary gearhead GP 32 A 23:1<sup>8</sup> and the incremental encoder Encoder HEDS 5540<sup>9</sup>. Several validations were carried out with this DC motor, in which the force feedback closed loop was implemented between the virtual platform and this motor. However, this solution was not applied since the haptic perception when freely interacting with the motor shaft was not satisfactory and smooth enough. Another possible solution to this problem can be the integration of a mechanical spring in the mechatronic system, instead of a virtual spring model. This requires the redesign of the haptic controllers to assembly the proper torsion spring. For the validations carried out in Chapter 4, higher proportional constant  $K_p$  were used.

Regarding the calculation of the virtual forces applied to the deflectable endoscope tip while controlling the virtual endoscope with the haptic system, the implemented force rendering approach is based on the same idea of the “finger-proxy” method

<sup>7</sup>[https://www.maxonmotor.com/medias/sys\\_master/root/8825411862558/17-EN-162.pdf](https://www.maxonmotor.com/medias/sys_master/root/8825411862558/17-EN-162.pdf)

<sup>8</sup>[https://www.maxonmotor.com/medias/sys\\_master/root/8825547882526/17-EN-335-336.pdf](https://www.maxonmotor.com/medias/sys_master/root/8825547882526/17-EN-335-336.pdf)

<sup>9</sup>[https://www.maxonmotor.com/medias/sys\\_master/root/8827036074014/17-EN-413-414.pdf](https://www.maxonmotor.com/medias/sys_master/root/8827036074014/17-EN-413-414.pdf)

(Ruspini et al., 1997) for calculating the exerted forces. In the latter force model, a virtual proxy represents the real cursor movements towards a goal. The position of the virtual proxy and the virtual cursor in free space is the same. When an external object avoids proxy direct motion to the virtual cursor, the proxy position is calculated by moving the proxy along the external surface of the object and minimizing the distance to the virtual cursor. Therefore, the proxy never penetrates the surrounding objects, and stays on the surfaces, whereas the virtual cursor can be located inside the obstacles. The implementation of the force computation can be easily done with the Hooke's Law  $F = k \times \Delta x$ , where  $k$  is the object's stiffness and  $\Delta x$  is the distance between the proxy position located at the surface of the object and the virtual cursor position, which is penetrating the object surface. Figure 3.12 shows the proxy position of a simple haptic tool, in blue, and the virtual cursor position going through the object, in red. The length of the vector between them ( $\Delta x$ ), in gray, is proportional to the force provided to the user. By modifying the stiffness coefficient  $k$  of this model, different materials can be modeled.

In this case, in order to calculate the virtual force that has to be finally provided by the haptic controllers when the endoscope tip is colliding,  $\Delta x$  is calculated as the distance between the position of center of mass of the computed endoscope tip located at the surface of the object and the position of the center of mass of the endoscope tip penetrating the object surface before the collision response (see Figure 3.13). The position of the center of mass is calculated as follows

$$\vec{x}_{cm} = \frac{\sum_i m_i \vec{x}_i}{\sum_i m_i} \quad (3.12)$$

where  $\vec{x}_i$  and  $m_i$  are the position and the mass of the node  $i$  composing the tip, respectively.

The calculated force is then sent to the Arduino Due, which converts this force into voltage for the signal that is going to be applied to the motors. This conversion between force and voltage is achieved with the constant  $K$  (see Figure 3.11). By modifying this constant, the haptic system can present different behaviours. If the

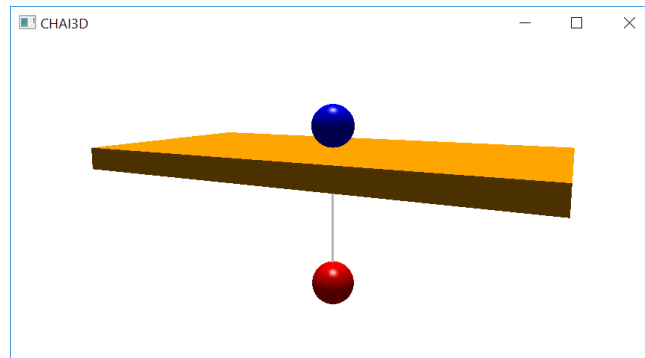


Figure 3.12: Proxy (in blue) and virtual cursor (in red) of the “finger-proxy” algorithm.  $\Delta x$  (in gray) is used for the force calculation with the Hooke's Law.

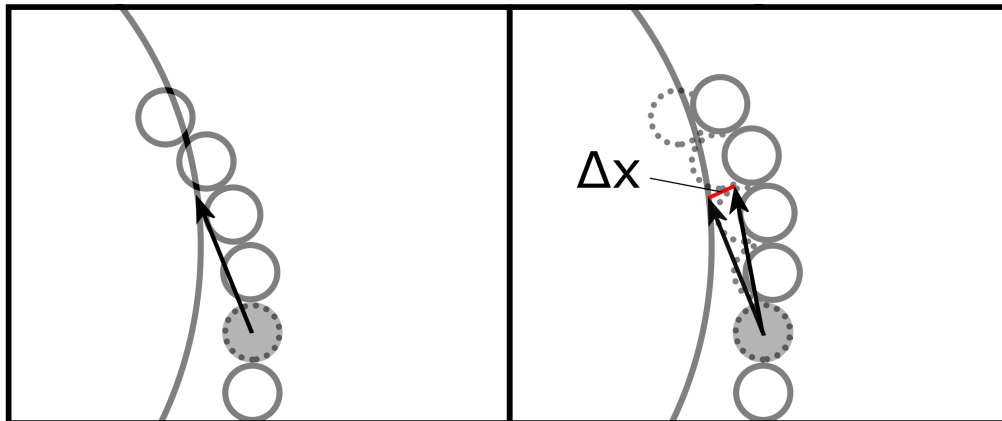


Figure 3.13: Force calculation implemented based on the Hooke's Law.

setup environment requires palpation or examination of structures with different stiffness performed by the end effector, low values for the constant  $K$  are preferred. On the contrary, if the exploration by the end effector is carried out in environments that may be easily damaged by touch, high values of this constant are preferred to prevent tissue injury. The selection of this constant was performed experimentally for the validations carried out in Chapter 4.



## CHAPTER

# 4

## VALIDATION

In this Chapter, the validations performed on the implemented training platform are described. They are divided into two different categories: validation carried out on the virtual flexible endoscope model and validation performed on the final training platform, including the force feedback close loop. The first category of validation aims to test the correct performance of the dynamics implemented to model the virtual endoscope, using the 3D mice as input controllers. The second category of validation has the objective of checking the proper execution of the developed force feedback between the assembled mechatronic haptic controllers and the virtual reality endoscopy environment resulting from the previous validation. In sections 4.1 and 4.2, both validations are addressed respectively.

### 4.1 Dynamics rendering validation

In this validation, the following features of the developed virtual reality platform were assessed:

- Computational rate.
- Visual rendering: refresh rate and visual plausibility.

In order to test the performance of the simulated flexible endoscope, different static tridimensional scenarios were created. These scenarios were composed of pipeline shaped objects with different configurations in which the endoscope is controlled with the 3D mice. These scenarios try to replicate in a simple way the natural shapes of a human urinary tract. Previously created STL models were imported in CHAI3D. The imported objects are polygon meshes, composed by a set of vertices and triangles creating a polyhedron. A high transparency level of the set material was configured,

in order to allow visual exploration of the inside of the objects from front view. Both endoscopic and front views were rendered in different windows.

Figure 4.1 shows front views of the visual plausibility of the endoscope model implemented in three different scenarios (Scenarios 1, 2 and 3), with non-anatomic appearance.

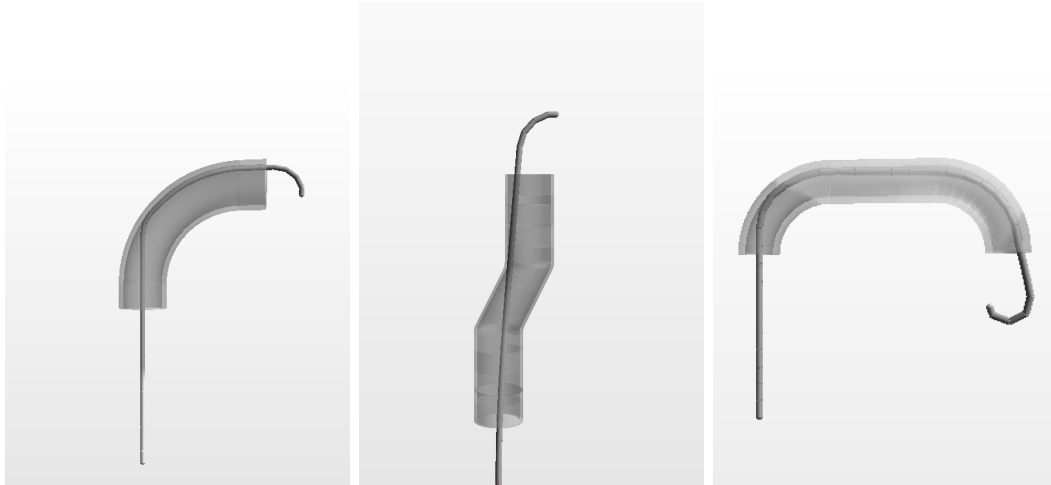


Figure 4.1: Performance of the simulated endoscope model in three different scenarios (from left to right: Scenario 1, 2 and 3, respectively).

The frequency of the computational loop was measured in seven different experiments. In each experiment, a user interacted with the training platform during an interval of 15 seconds in each scenario. In this validation, the number of spherical nodes comprising the virtual endoscope was 37. Figure 4.2 depicts the results obtained in terms of computational rate.

Regarding the execution rate, the computational loop frequency is higher than  $3\text{ kHz}$  in 91 % of the cases and lower than  $1\text{ kHz}$  in 1.04 % of the cases, as shown in the graphs. Concerning the time intervals longer than 2 ms (frequencies lower than 500 Hz), it could be observed that they do not cause a detectable visual impact.

In addition to the non-anatomic scenarios, navigation through a three-dimensional ureterorenal model was implemented (Scenario 4) for creating an accurate and realistic training platform. The 3D model was previously acquired with a CT scan on a real urinary tract. It was then imported in CHAI3D as a polygon mesh.

In this scenario, the training platform provides two different views in different windows, emulating the real surgical setting: the endoscope monitor displaying real time intraoperative images and a remote front view of the patient body equivalently to the radiographic acquisition (see Figure 4.3). The equivalent X-rays view is only updated when required by the surgeon and allows the specialist to know the current exact location of the endoscope. Moreover, the simulation of the laser lithotripsy was implemented (see Figure 4.4). Different calculi locations and morphologies can be

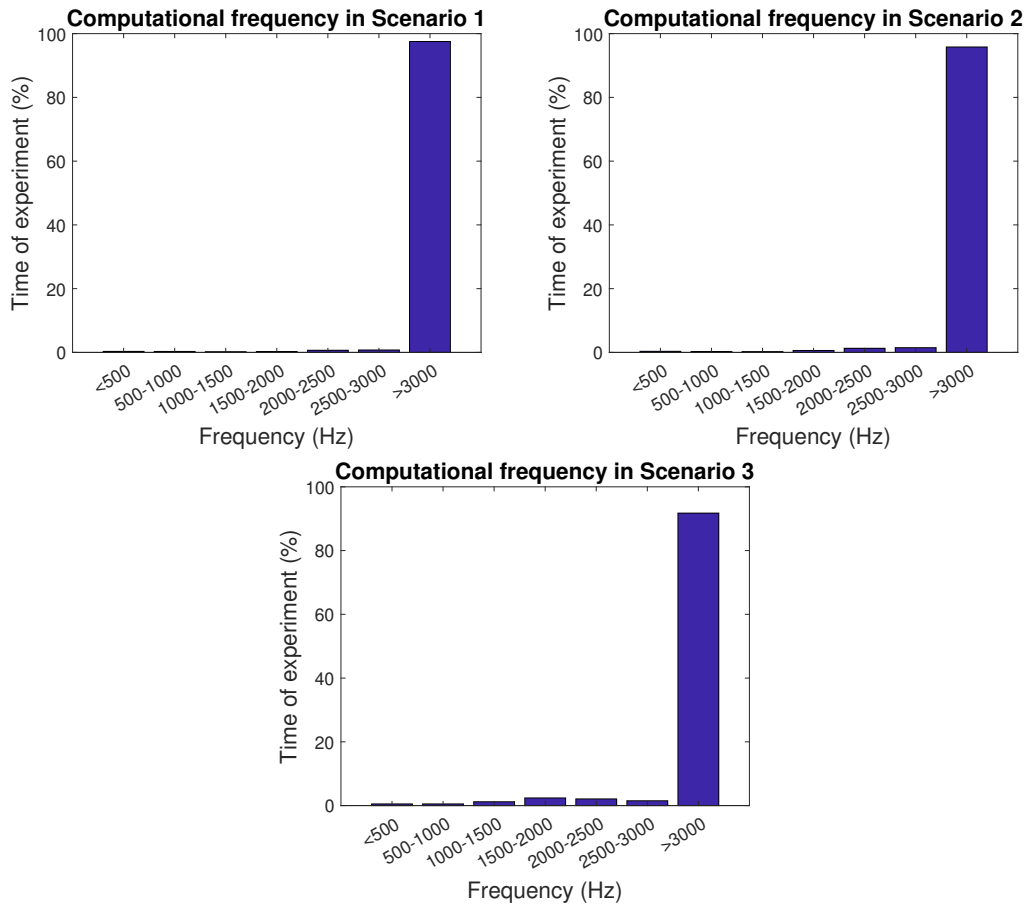


Figure 4.2: Mean computational frequency results obtained with seven experiments of 15 seconds in scenarios 1, 2 and 3.

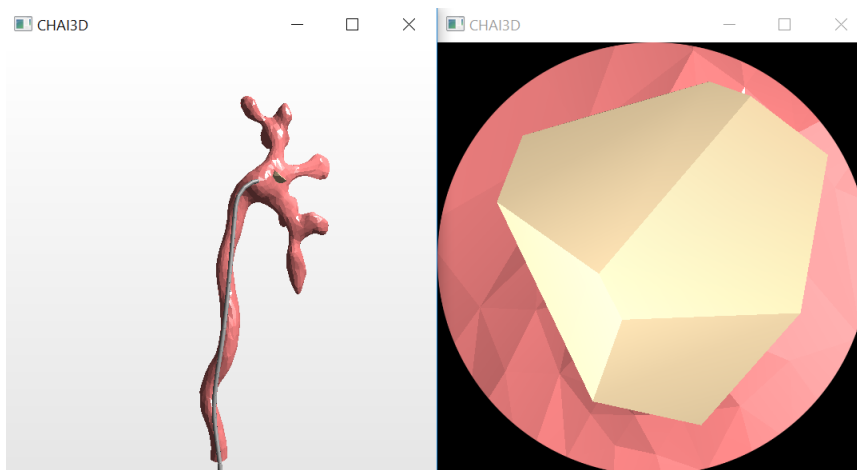


Figure 4.3: Implemented virtual reality environment user interface, including endoscopy (right) and radiography (left) screens.

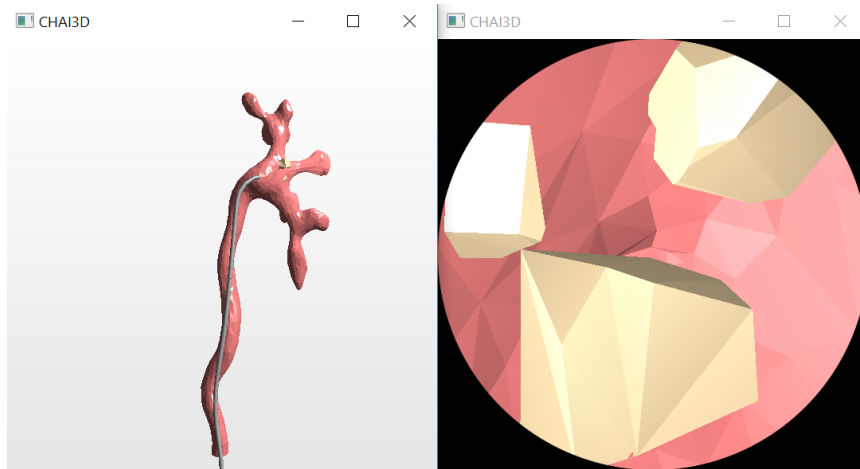


Figure 4.4: Simulation of the lithotripsy procedure.

presented to the surgeon, in order to simulate multiple clinical scenarios.

Like in the previous scenarios, the frequency of the computational loop was measured in seven different trials of 15 seconds each. The number of spherical nodes comprising the virtual endoscope was 37. Figure 4.5 depicts the results obtained in terms of computational rate.

Regarding the computational rate, the frequency is higher than  $3\text{ kHz}$  in 90.7 % of the cases and lower than  $1\text{ kHz}$  in 0.97 % of the cases. Concerning the frequencies lower than 500 Hz, as in the previous scenarios, they did not have any visual effect.

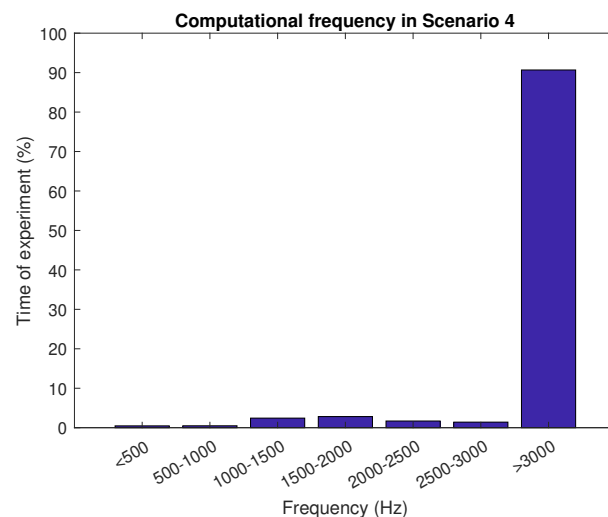


Figure 4.5: Computational frequency results obtained with experiments of 15 seconds in Scenario 4.

As observed in Table 4.1, the performance of the algorithm for the four scenarios

Scenario	% of computational rate (Hz)						> 3000
	< 500	500– 1000	1000– 1500	1500– 2000	2000– 2500	2500– 3000	
1	0.312	0.294	0.19	0.246	0.669	0.754	97.536
2	0.337	0.26	0.218	0.604	1.289	1.483	95.809
3	0.521	0.52	1.208	2.392	2.094	1.513	91.752
4	0.475	0.496	2.432	2.815	1.698	1.415	90.67

Table 4.1: Comparison mean percentage of execution time running at the different frequency ranges in Scenarios 1, 2, 3 and 4.

is similar. However, lower frequencies are reached more often in the third and fourth environments. It was determined that there is a relationship between the execution time and the number of collided nodes that have to be handled. Figure 4.6 shows the relationship between the mean execution frequency and the number of colliding nodes in experiments of 15 seconds with a user in the four scenarios. It can be observed that lower mean computational frequencies are achieved when the number of collided nodes is higher. This effect is expected, since the most time-consuming

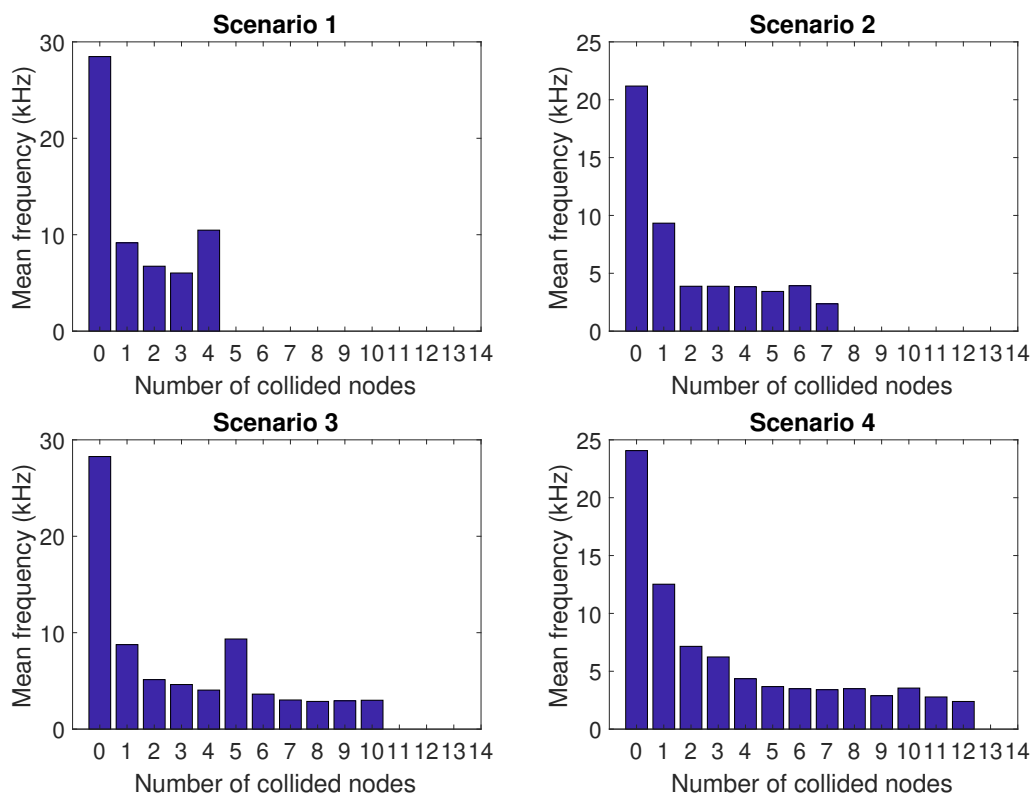


Figure 4.6: Relation between mean computational frequency and number of nodes colliding.

task is the collision detection and handling when the virtual endoscope model reaches a position where the nodes are colliding with a complex obstacle and the constraints are not satisfied. This effect can be observed in the computational rates of Scenario 3 and 4. This behavior is also expected, because the geometries of Scenario 3 and the ureterorenal model are more complex than that of the other environments, leading to a higher number of collisions and constraints that have to be handled. As a result, lower computational rates are reached during a higher execution time percentage, as shown in Table 4.1. In addition, it is important to emphasize that this relationship also depends on the current shape of the virtual endoscope model and how unsatisfied the constraints established between the nodes are. There may be cases in which the constraints got satisfied by the algorithm, although many nodes are colliding, leading to higher computational frequencies after finding that solution. This effect can be observed in the relationships of Scenario 1 and Scenario 3 in Figure 4.6, in which higher mean frequencies are reached with four and five colliding nodes, respectively.

Regarding the frame rate, no significant differences between the scenarios were observed. However, the update rate differs considerably between the following display modes: the first mode consists of a visual interface with real-time endoscopic view and updated radiographic view by pressing a key; the second mode renders both views in real time. Mean percentage of execution time reaching different frame rates are shown in Table 4.2, for experiments of 15 seconds with a user in Scenario 4 for both display modes. It can be observed that with the rendering of a view, frame rates above 50 fps are reached during the total execution time of the simulation. On the contrary, when rendering both the endoscopic and radiographic views in real time, the frame rate is approximately half of the previous case. The frame rate is always below 40 fps, and sometimes it reaches update frequencies below 25 Hz. In this case, the minimum refresh rate for the human eye to perceive movement (25 fps) is not achieved in some cases. This is because the amount of visual information that has to be rendered is higher and the priority of the graphic loop is lower than the computational loop. In the first view mode, the minimum refresh rate is preserved and the simulation is also more similar to the real surgical scenario, in which the radiographic images are acquired when required.

Mode	% of frame rate (fps)					
	< 25	25– 30	30– 40	40– 50	50– 60	> 60
Endoscopic real-time view	0	0	0	0	38.017	61.983
Both real-time views	2.99	5.767	91.243	0	0	0

Table 4.2: Mean percentage of execution time running at the different frame rates in Scenario 4 for both display modes.

## 4.2 Haptic feedback validation

In order to test the proper execution of the developed force feedback between the final mechatronic system and the virtual reality endoscopy environment resulting from the previous validation, a second validation was carried out. The objective of this validation was the evaluation of:

- The computational time of the force calculation task.
- The computational time of the communication task.

The user interface presented in Figure 4.7 was developed and provided to the user. In this new interface, the radiographic view displays a real-time graph with the force provided to the user for each DOF of the endoscope.

Since Scenario 4 presented the lowest computational frequencies in the last validation, the experiments of the current validation were performed in this scenario. The mean computational time required for the calculation of the force and the communication with the Arduino Due is presented in Table 4.3, for seven experiments of 15 seconds with a user in Scenario 4. As observed in these results, the realization of these two tasks takes around 30 % of the total computational time, taking the communication task around 99.8 % of the total time. However, the virtual endoscope rendering remains as the most time-consuming task.

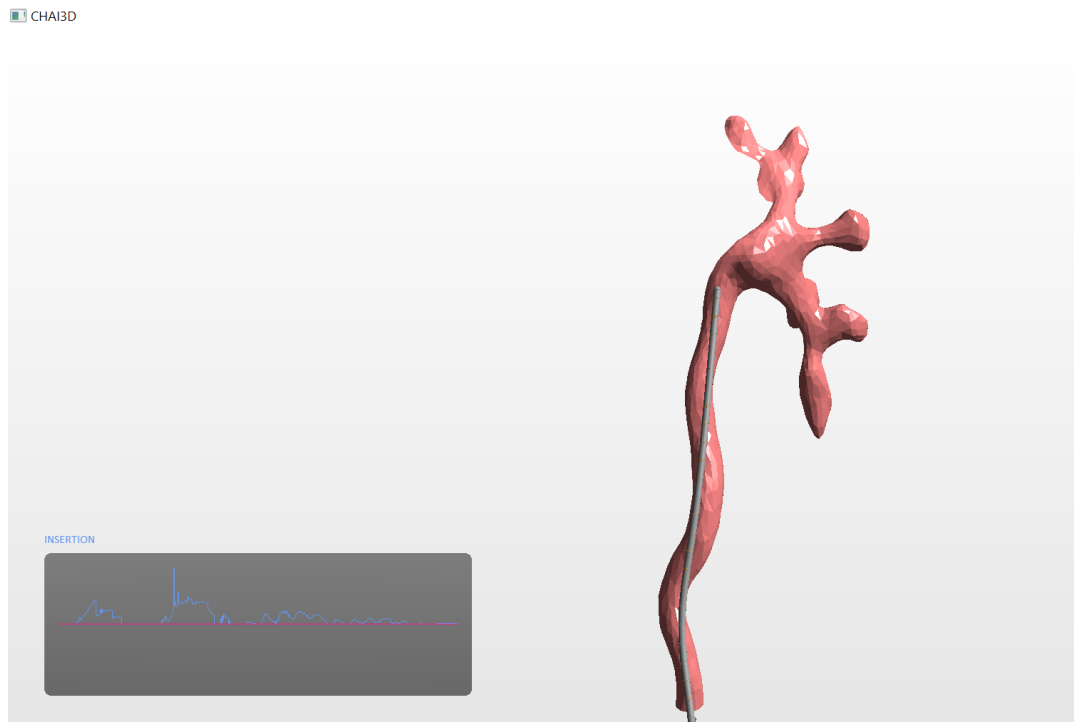


Figure 4.7: Implemented virtual reality environment user interface for the force feedback close loop (radiographic view).

Task	Mean time (%)
Force calculation + communication	29.5901
Communication	29.5321

Table 4.3: Mean time required for force calculation and communication.

Table 4.4 depicts the results obtained in terms of computational rate with the implemented closed-loop force feedback. Computational rates above  $3\text{ kHz}$  are reached around 61 % of the total time, whereas execution frequencies below  $1\text{ kHz}$  are achieved in 1.54 % of the cases. These cases were not significantly perceived in the haptic perception. In this case, lower frequencies take a higher percentage of the total execution time, in comparison to the training platform running without haptic feedback. This may be caused by the communication between the virtual environment and the haptic controllers. However, a minimum frequency for a stable haptic feedback ( $1\text{ kHz}$ ) is preserved in 98.458 % of the cases.

Scenario	% of computational rate (Hz)						
	< 500	500– 1000	1000– 1500	1500– 2000	2000– 2500	2500– 3000	> 3000
4	0.21	1.332	1.964	5.814	14.305	15.421	60.953

Table 4.4: Mean percentage of execution time running at the different frequency ranges in Scenarios 4 with force feedback.

## CHAPTER

# 5

## CONCLUSIONS AND FUTURE WORK

In this Chapter, conclusions drawn from the experiments and validations performed on the developed virtual reality haptic platform are discussed. In addition, possible future lines of research resulting from this Master's thesis are addressed.

### **5.1 Conclusions**

As explained in Chapter 1, many robotic surgical systems have been designed for MIS interventions up to now, which offer many advantages for patients and surgeons. The safety and feasibility of robot-assisted minimally invasive surgery has been demonstrated for different medical interventions. However, just a few of robotic surgical systems have been proved to work on flexible ureteroscopy. It is within this gap where the LITHOS project emerges. The LITHOS project provides a novel system that allows the remote control of the flexible endoscope by the use of robotics as an alternative to traditional ureterorenoscopic interventions. The main objective of the implementation of this robotic surgical system is to meet the needs of both patients and surgeons, offering a solution to the drawbacks associated to the conventional flexible ureterorenoscopy technique from the urologists point of view. This surgical robotic system will be composed by a patient site and a surgeon console, which provides the urologists with a more ergonomic workplace, remote from radiation sources used to acquire intraoperative images.

In this Master's thesis, the implemented virtual training platform for LITHOS project has been presented. It comprises the same interface of the robotic system, including the endoscope controllers, endoscopic and radiographic screens and laser

activation for lithotripsy procedures. First, the dynamic model for the virtual flexible endoscope was implemented using the same principles of the position based approach and the shape matching method. The resulting virtual reality environment is controlled by two 3D mice. After that, the integration of the developed simulation platform with a force feedback closed loop was developed. Two mechatronic controllers were designed and assembled to provide haptic feedback to the user when steering the virtual flexible endoscope.

Both the dynamic model of the flexible ureteroscope and the final haptic system were validated by undertaking several experiments to evaluate their performance. The first validation aimed to assess the computational rate, the visual plausibility and the refresh rate of the virtual reality environment in different scenarios, including the navigation through a three-dimensional ureterorenal model. The second validation had the objective of testing the performance rate of the force calculation and communication when the haptic feedback was established between the designed controllers and the virtual platform.

Regarding the first validation, the obtained results in terms of execution time determine that the training platform developed presents different computational rates depending on the complexity of the implemented environment and on the number of collisions and constraints that have to be handled. However, in this initial study it could be observed that this does not have any detectable visual impact. Computational frequency is higher than  $3\text{ kHz}$  in 91 % of the cases whereas the simulation update rate is always above 50 fps with the display mode of the user interface similar to the real surgical scenario. These outcomes show that the developed virtual reality endoscope model and platform are suitable and plausible for the urologic surgeon training. Concerning the second validation, the performance of the assembled haptic devices is adequate, taking into consideration that this implementation aimed to develop a first prototype of haptic controllers for the virtual reality platform. With regard to the force feedback calculation and communication between the simulated environment and the Arduino Due, the data transmission takes around the 30 % of the execution time. Even so, the dynamics algorithm of the virtual endoscope is the most time-consuming task. Concerning the computational rates, lower frequencies are achieved during a higher percentage of the total execution time, in comparison to the training platform running without haptic feedback. This result is expected taking into account the computational time required for the communication. However, minimum frequency for a stable haptic feedback ( $1\text{ kHz}$ ) is preserved in 98.458 % of the total execution time.

As a conclusion, the developed virtual environment presents a correct and feasible performance in this development initial stage and offers a suitable tool for the training of urologic surgeons manipulating the LITHOS system in flexible ureterorenoscopy interventions. This environment also provides a useful platform for the surgical planning of future fURS interventions.

During the development of this Master's thesis, the article with title "Virtual Re-

ality Training Platform for Flexible Ureterorenoscopy Interventions with a Minimally Invasive Surgical Robot” (Peral Boiza et al., 2017) was published in the Congreso Anual de la Sociedad Española de Ingeniería Biomédica 2017 (CASEIB 2017).

## 5.2 Future work

This Master’s thesis has presented a first approach of a virtual reality training platform for the use of the LITHOS robot in flexible ureterorenoscopic interventions. From this initial work, some future work lines emerge:

- A clinical validation has to be undertaken in order to determine the reduction of the learning curve of the surgeons in flexible ureterorenoscopic interventions. The evaluation of the increase of the dexterity of urologists using the LITHOS robot has to be carried out.
- The study of different approaches for the modeling of flexible materials that could be implemented on the rendering of the endoscope deflectable tip is proposed.
- The development of dynamic environments may be appropriate to test the implemented training platform in a more accurate scenario. These realistic environments may include deformable tissue. However, the rendering of deformable objects that comprise a high number of nodes may reduce the performance of the training platform when including the haptic feedback. Therefore, further studies should be undertaken in this line.
- Due to the important subjective component of this platform, further studies of the haptic perception for the assessment of the developed haptic feedback provided to the user are proposed. Evaluation of the tactile sensation in different participants may be performed in order to find a generalized subjective feedback of the provided force.



# Appendices



APPENDIX

A

ETHICAL, ECONOMIC, SOCIAL  
AND ENVIRONMENTAL ASPECTS

## A.1 Introduction

The main objective of this Master's thesis is the creation of a virtual reality platform for the training of surgeons in ureterorenoscopic interventions using the surgical robotic system of the LITHOS project. The use of computer-assisted systems for performing minimally invasive procedures offers greater precision and can increase the surgeon dexterity (Fuchs, 2002). However, it is required that the surgeons learn to use these innovative systems and the learning curve associated with these type of interventions is generally prolonged. The development of surgical simulations for medical training aims to provide solutions to these limitations. These virtual reality training environments have to be certificated and validated, in order to evaluate their efficacy, utility and feasibility. Moreover, the creation of training programs for surgeons is required and challenging. The simple use of a surgical simulator is not enough to ensure the learning and training of surgeons, and specialized training curricula have to be developed for each type of intervention.

The positive impact of the surgical simulation over the surgeons have been repeatedly reported. Its advantages include improvements in the efficiency and skills of the surgeon, learning curve reduction, improved educational experience, reduction in costs and easy access to different types of clinical scenarios (Al Bareeq et al., 2008). The main target group of this Master's thesis is the urologic surgeons that will perform flexible ureterorenoscopic interventions with the final robotic system of the LITOS project. However, the same model proposed in this project can be applied in the implementation of training simulators of others surgical procedures.

Figure A.1 represents the impacts in relation to the area of influence and the life cycle phase of the product developed in this Master's thesis.

	<b>Ethical and professional aspects</b>	<b>Economic aspects</b>	<b>Social aspects</b>	<b>Environmental aspects</b>
Production and testing	Use of third-party software CHAI3D with BSD License	Low-cost design and implementation	Accessibility for all; design for all	Use of PLA for 3D printing
Packaging and distribution				
Use and maintenance	Low-cost maintenance			
Reuse and recycling	Easily reusable			

Figure A.1: Impacts in relation to the area of influence and the life cycle phase of the product.

## **A.2 Description of significant impacts associated with this project**

In this Section, the impacts in relation to the area of influence determined in Figure A.1 are addressed.

Regarding the ethical and professional aspects, the use of the third-party software CHAI3D (CHAI3D, 2018) for the implementation of the virtual reality training platform has to be considered. CHAI3D is a C++, open-source and multiplatform simulation framework designed to integrate tactile and visual sensations in real time. CHAI3D includes several libraries for computer haptics, visualization and interactive real-time simulation, which make it a very useful platform for developing the integration of virtual environments with force-feedback. This framework uses the BSD license, which is a permissive free software license. It allows the redistribution and use of the software, with or without modification, provided that the redistributions of source code retain a specific copyright notice, list of conditions and disclaimer. Thus, the use of third-party software is allowed in the proposed project and does not pose copyright concerns.

With regard to the economic aspects, one of the objectives of this Master's thesis is the creation of a surgical virtual reality simulator with a low-cost design and implementation. This explains the use of 3D printing as production technology in this first prototype. The maintenance of the simulator is also low-cost and simple. The software component of the virtual environment can be easily maintained with the release of consecutive updates. Regarding the reuse and recycling of the platform, the printed parts can be easily recycled (see Section A.3), whereas the software component does not really need a recycling procedure. Moreover, the versatility and flexibility of the model proposed in this project allow its reapplication to the implementation of training simulators of others surgical procedures.

Concerning the social aspects, the design of this virtual reality platform aims to be accessible to everyone, using low-cost resources and open-source software. The main target group of this project is the urologic surgeons performing flexible ureterorenoscopic interventions with the final robotic system of the LITOS project. Therefore, the feedback of urologists has been taken into account, in order to design a system that meets the real necessities of the target group.

Regarding the environmental aspects, the use of 3D printing technology has a direct impact on the environment. In this project, the printing material used was polylactic acid (PLA), a biodegradable material derived from renewable resources, such as corn starch. The use of this material to produce the mechanical parts of the final prototype can be beneficial in several aspects, in comparison to the use of other resources (see Section A.3).

All the explained aspects have been considered in this Master's thesis, aiming to develop a final system that complies with the regulations and is environmentally conscious, law-abiding and accessible to everyone.

### A.3 Detailed analysis of a significant impact

In this Section, the environmental impact of the use of 3D printing as manufacturing technology is analyzed in detail. 3D printing is an additive manufacturing process in which three-dimensional objects are created by building layers of liquid resin (Berman, 2012). This process allows the user to produce custom products at low costs with readily available supplies. It facilitates and speeds up the development and modification of model designs. However, it has also some drawbacks, like not enough precision required to some applications, reduced choice for materials or surface finishes, and limited strength or resistance to heat. For the objective of this project, 3D printing technology meets the expected requirements for the development of a first prototype. The environmental impact of this technology, that is becoming more and more popular in the recent years, has to be analyzed.

In a study developed in 2013 (Cuboyo, 2018), the environmental impact of traditional injection molding manufacturing and 3D printing was compared. Results showed that the environmental impact of 3D printing depends on the electrical consumption of the 3D printer, since high quality printers usually present higher electrical consumption. Moreover, the study showed that the environmental impact of 3D printing is lower when compared to injection molding for low volume production (<1000 parts). Classic manufacturing is not adequate for low volume production in terms of environmental impact, and 3D printing cannot compete with injection molding when producing high volume of products. Regarding the material saving in the production phase, 3D printing technology enables the creation of pieces without the use of additional molds like in traditional production. In addition, 3D printing can produce lighter pieces which also reduces the fuel consumption in the distribution process.

In the development of this Master's thesis, polylactic acid (PLA) was used as printing resin. It is a biodegradable material derived from renewable resources, such as corn starch. It presents the resin identification code 7 of the Society of the Plastics Industry. It can be recycled and composted. In addition, this material has been proven to be less toxic than other alternatives, like acrylonitrile-butadiene-styrene (ABS) (Wojtyła et al., 2017).

As a conclusion, although the manufacturing technique used in this project presents some limitations, it is more environmentally conscious than other alternatives. Moreover, it allows the custom design of the pieces according to the necessities of the users, providing also low-cost products accessible for everyone.

### A.4 Conclusions

To sum up, the study of the impacts of the proposed Master's thesis shows that the final prototype has a positive direct effect over the target group and does not affect negatively the society nor the environment. The decisions taken in the design and

implementation of the project have contributed towards the development of a low-cost product accessible to all, meeting the real needs of the final users. In addition, the final result is environmentally friendly and coherent with the professional and ethic principles.



APPENDIX

B

ECONOMICAL BUDGET

Figure B.1 shows the calculated economical budget of the project developed in this Master's thesis.

<b>Labour cost (direct cost)</b>			
	hours	€/hour	TOTAL
	500	10,00 €	<b>5.000,00 €</b>

<b>Materials cost (direct cost)</b>				
	Purchase price	Months of use	Years of depreciation	TOTAL
Personal computer	2.000,00 €	6	4	250,00 €
2 x SpaceMouse Compact	307,02 €	6	4	38,38 €
2 x Faulhaber DC Gearmotors	192,00 €	6	4	24,00 €
Faulhaber DC Micromotor	124,00 €	6	4	15,50 €
Tactile DIP push button	0,65 €	6	4	0,08 €
Prusa i3 Hephestos	299,00 €	6	4	37,38 €
<b>TOTAL MATERIALS COST</b>				<b>365,33 €</b>

<b>Overhead cost (indirect cost)</b>	15%	over DC	<b>804,80 €</b>
<b>Industrial benefit</b>	6%	over DC+IC	<b>370,21 €</b>

<b>Consumables</b>	
BQ Filament PLA 1.75mm 1kg	<b>56,97 €</b>

<b>SUBTOTAL BUDGET</b>	<b>6.597,31 €</b>
<b>Applicable VAT</b>	21% <b>1.385,44 €</b>

<b>TOTAL BUDGET</b>	<b>7.982,75 €</b>
---------------------	-------------------

Figure B.1: Economical budget of the project.

APPENDIX

C

FAULHABER DC GEARMOTORS  
2619S012SR 22:1 + IE2-16 - MOTOR &  
ENCODER SPECIFICATIONS

# DC-Gearmotors

Precious Metal Commutation  
with integrated Encoder

## 100 mNm

For combination with  
Drive Electronics:  
Speed Controller

### Series 2619 ... SR ... IE2-16

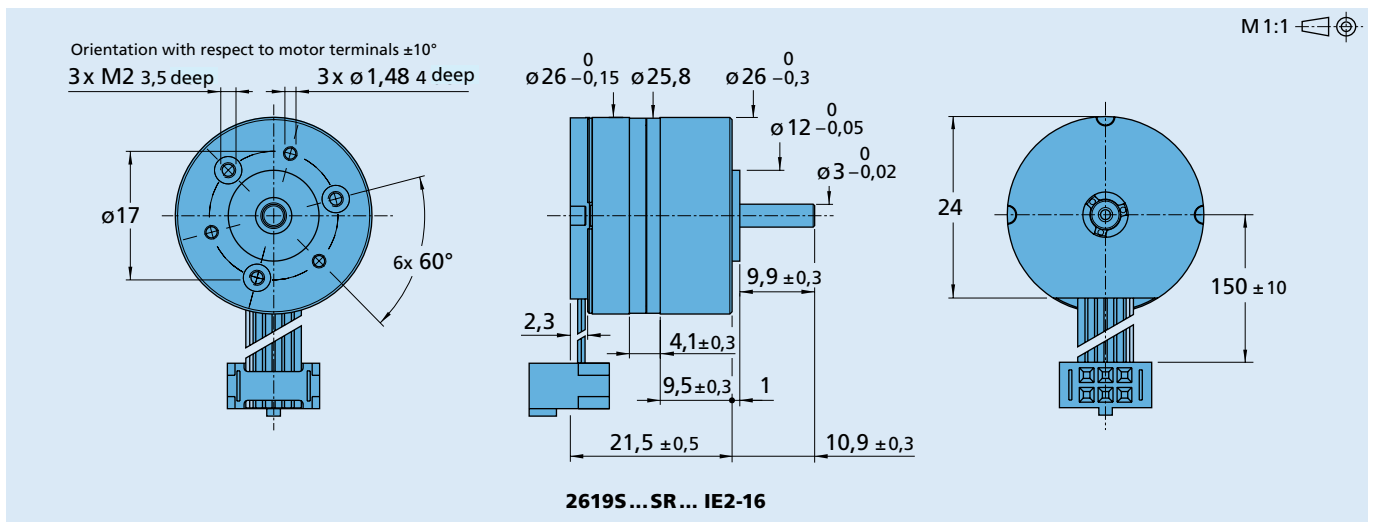
Values at 22°C and nominal voltage		2619 S	006 SR	012 SR	024 SR	IE2-16
Nominal voltage	$U_N$		6	12	24	Volt
Terminal resistance	$R$		8	31,2	118,6	$\Omega$
No-load speed (motor)	$n_0$		6 700	6 900	7 200	$\text{min}^{-1}$
Speed constant	$k_n$		1 130	582	304	$\text{min}^{-1}/\text{V}$
Back-EMF constant	$k_E$		0,884	1,72	3,29	$\text{mV}/\text{min}^{-1}$
Torque constant	$k_M$		8,44	16,4	31,4	$\text{mNm}/\text{A}$
Current constant	$k_I$		0,118	0,061	0,032	$\text{A}/\text{mNm}$
Slope of n-M curve	$\Delta n/\Delta M$		1 060	1 090	1 110	$\text{min}^{-1}/\text{mNm}$
Rotor inductance	$L$		420	1 600	5 800	$\mu\text{H}$
Rotor inertia	$J$		0,68	0,68	0,68	$\text{gcm}^2$

Housing material		plastic				
Geartrain material		metal				
Backlash, at no-load	$\leq$	4				$^\circ$
Bearings on output shaft		brass / ceramic bearings	ball bearings, preloaded			
Shaft load max.:		(standard)	(optional)			
– radial (5 mm from mounting face)	$\leq$	3,5	10,5			N
– axial	$\leq$	2	5			N
Shaft press fit force, max.	$\leq$	10	10			N
Shaft play:						
– radial (5 mm from mounting face)	$\leq$	0,07	0,03			mm
– axial	$\leq$	0,25	0			mm
Operating temperature range		0 ... + 70				$^\circ\text{C}$

### Specifications

reduction ratio (rounded)	output speed up to $n_{\text{max}}$ $\text{min}^{-1}$	weight with motor g	output torque		direction of rotation (reversible)	efficiency %
			continuous operation $M_{\text{max}}$ mNm	intermittent operation $M_{\text{max}}$ mNm		
8 : 1	635	25	9	30	=	81
22 : 1	223	26	23	75	$\neq$	73
33 : 1	151	26	30	100	=	66
112 : 1	44	27	93	180	$\neq$	59
207 : 1	24	27	100	180	=	53
361 : 1	14	27	100	180	=	53
814 : 1	6	28	100	180	=	43
1 257 : 1	4	29	100	180	=	43

Note: output speed at 5000  $\text{min}^{-1}$  input speed. Based on motor 2607 ... SR.



Integrated optical Encoder	IE2-16		
Lines per revolution	<i>N</i>	16	
Signal output, square wave		2	channels
Supply voltage	<i>U<sub>DD</sub></i>	3,2 ... 5,5	V DC
Current consumption, typical ( <i>U<sub>DD</sub></i> = 5V DC)	<i>I<sub>DD</sub></i>	typ. 8, max. 15	mA
Output current, max. allowable (at <i>U<sub>out</sub></i> < 1,5V)	<i>I<sub>OUT</sub></i>	5	mA
Pulse width <sup>1)</sup>	<i>P</i>	180 ± 45	°e
Phase shift, channel A to B <sup>1)</sup>	<i>Φ</i>	90 ± 45	°e
Signal rise/fall time, max. ( <i>C<sub>LOAD</sub></i> = 50 pF)	<i>tr/tf</i>	2,5/0,3	µs
Frequency range <sup>2)</sup> , up to	<i>f</i>	4,5	kHz

<sup>1)</sup> Ambient temperature 22°C (tested at 1kHz)

<sup>2)</sup> Velocity (min<sup>-1</sup>) = *f* (Hz) x 60/*N*

### Features

In this version, the DC-Micromotors have an optical encoder with two output channels. A code wheel on the shaft is optically captured and further processed. At the encoder outputs, two 90° phase-shifted rectangular signals are available with 16 impulses per motor revolution.

The encoder is suitable for the monitoring and regulation of the speed and direction of rotation and for positioning the drive shaft.

The supply voltage for the encoder and the DC-Micromotor as well as the two channel output signals are interfaced through a ribbon cable with connector.

### Full product description

■ Examples:

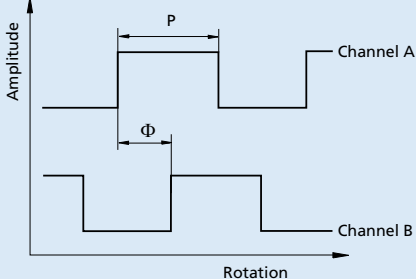
2619S006SR 8:1 IE2-16

2619S024SR 1257:1 IE2-16

### Output signals / Circuit diagram / Connector information

#### Output signals

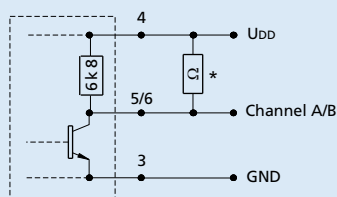
with clockwise rotation as seen from the shaft end



Admissible deviation of phase shift:

$$\Delta\Phi = \left| 90^\circ - \frac{\Phi}{P} * 180^\circ \right| \leq 45^\circ$$

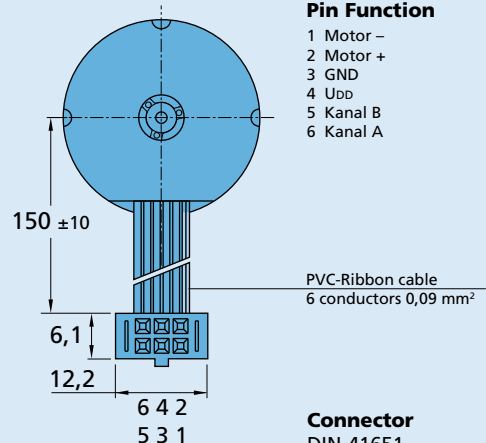
#### Output circuit



\* An additional external pull-up resistor can be added to improve the rise time. Caution: *I<sub>OUT</sub>* max. 5 mA must not be exceeded!

#### Pin Function

- 1 Motor -
- 2 Motor +
- 3 GND
- 4 U<sub>DD</sub>
- 5 Kanal B
- 6 Kanal A



**Connector**  
DIN-41651  
grid 2,54 mm



APPENDIX

D

FAULHABER DC MICROMOTOR  
1516E012SR + 16A 41:1 + IE2-16 -  
MOTOR & ENCODER  
SPECIFICATIONS

# DC-Micromotors

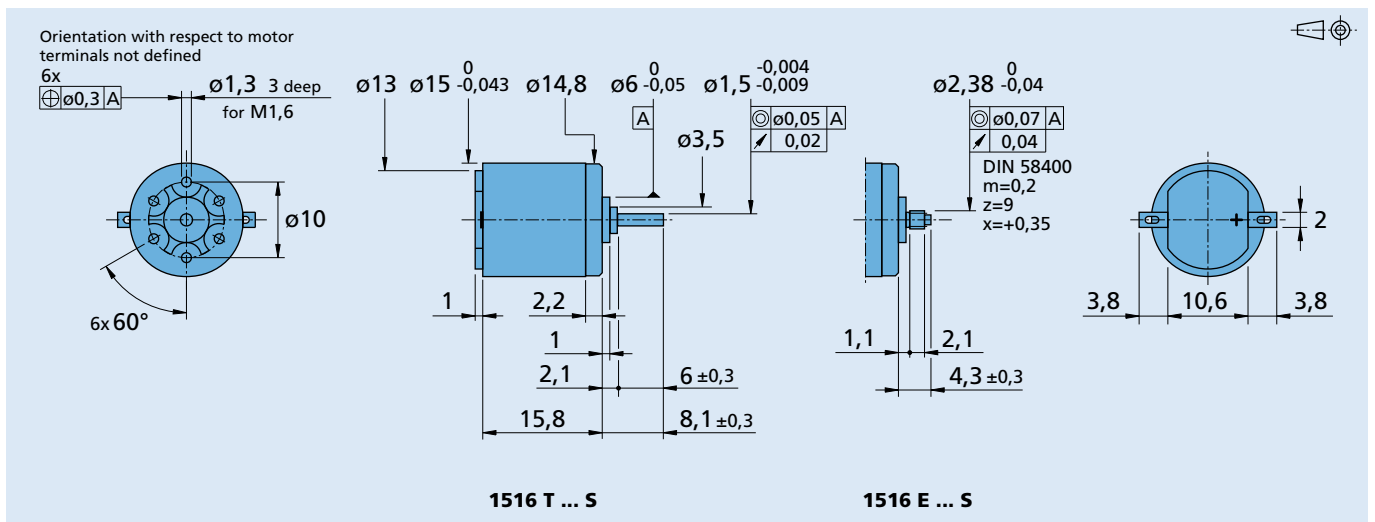
## 0,4 mNm

### Precious Metal Commutation

For combination with  
Gearheads:  
15/5(S), 16A

## Series 1516 ... S

	1516 T	1,5 S	002 S	4,5 S	006 S	012 S	
1 Nominal voltage	$U_N$	1,5	2	4,5	6	12	V
2 Terminal resistance	R	1,11	3,25	14,7	31,2	115	$\Omega$
3 Output power	$P_2 \text{ max.}$	0,45	0,25	0,29	0,23	0,25	W
4 Efficiency, max.	$\eta \text{ max.}$	59	48	50	45	47	%
5 No-load speed	$n_0$	14 400	14 200	15 000	15 000	15 600	rpm
6 No-load current (with shaft $\varnothing$ 1,5 mm)	$I_0$	0,075	0,057	0,027	0,021	0,011	A
7 Stall torque	$M_H$	1,2	0,68	0,73	0,59	0,62	mNm
8 Friction torque	$M_R$	0,07	0,07	0,07	0,07	0,07	mNm
9 Speed constant	$k_n$	10 159	7 827	3 659	2 800	1 445	rpm/V
10 Back-EMF constant	$k_E$	0,098	0,128	0,273	0,357	0,692	mV/rpm
11 Torque constant	$k_M$	0,94	1,22	2,61	3,41	6,61	mNm/A
12 Current constant	$k_i$	1,064	0,82	0,383	0,293	0,151	A/mNm
13 Slope of n-M curve	$\Delta n/\Delta M$	12 000	20 800	20 600	25 600	25 100	rpm/mNm
14 Rotor inductance	L	16	27	140	240	900	$\mu\text{H}$
15 Mechanical time constant	$\tau_m$	39	45	56	56	60	ms
16 Rotor inertia	J	0,31	0,21	0,26	0,21	0,23	$\text{gcm}^2$
17 Angular acceleration	$\alpha \text{ max.}$	39	32	28	28	27	$\cdot 10^3 \text{ rad/s}^2$
18 Thermal resistance	$R_{th 1} / R_{th 2}$	8 / 45					K/W
19 Thermal time constant	$\tau_{w1} / \tau_{w2}$	2 / 200					s
20 Operating temperature range:		-30 ... +65 (optional version -55 ... +125)					$^{\circ}\text{C}$
- motor							$^{\circ}\text{C}$
- rotor, max. permissible		+65 (optional version +125)					$^{\circ}\text{C}$
21 Shaft bearings		sintered bearings	ball bearings	ball bearings,			
22 Shaft load max.:		(standard)	(optional version)	preloaded	(optional version)		
- with shaft diameter		1,5	1,5	1,5	mm		
- radial at 3 000 rpm (3 mm from bearing)		1,2	5	5	N		
- axial at 3 000 rpm		0,2	0,5	0,5	N		
- axial at standstill		20	10	10	N		
23 Shaft play							
- radial	$\leq$	0,03	0,015	0,015	mm		
- axial	$\leq$	0,2	0,2	0	mm		
24 Housing material		steel, zinc galvanized and passivated					
25 Weight		10					g
26 Direction of rotation		clockwise, viewed from the front face					
<b>Recommended values - mathematically independent of each other</b>							
27 Speed up to	$n_e \text{ max.}$	12 000	12 000	12 000	12 000	12 000	rpm
28 Torque up to	$M_e \text{ max.}$	0,4	0,4	0,4	0,4	0,4	mNm



# Encoders

## Magnetic Encoders

**Features:**  
 16 Lines per revolution  
 2 Channels  
 Digital output

### Series IE2 – 16

		IE2 – 16	
Lines per revolution	N	16	
Signal output, square wave		2	channels
Supply voltage	V <sub>DD</sub>	4 ... 18	V DC
Current consumption, typical (V <sub>DD</sub> = 12 V DC)	I <sub>DD</sub>	typ. 6, max. 12	mA
Output current, max. admissible	I <sub>OUT</sub>	15	mA
Phase shift, channel A to B <sup>2)</sup>	Φ	90 ± 45	°e
Signal rise/fall time, max. (C <sub>LOAD</sub> = 100 pF)	tr/tf	2,5 / 0,3	µs
Frequency range <sup>1)</sup> , up to	f	7	kHz
Inertia of code disc	J	0,11	gcm <sup>2</sup>
Operating temperature range		-25 ... +85	°C

<sup>1)</sup> Velocity (rpm) = f (Hz) x 60/N

<sup>2)</sup> Tested at 2 kHz

### Ordering information

Encoder type	number of channels	lines per revolution	in combination with:
IE2 – 16	2	16	DC-Micromotors 1336 ... CXR, 1516 ... SR, 1524 ... SR, 1717 ... SR, 1724 ... SR, 1727 ... C, 1741 ... CXR, 2224 ... SR, 2232 ... SR, 2342 ... CR, 2642 ... CR, 2657 ... CR, 3242 ... CR, 3257 ... CR, 3272 ... CR, 3863 ... C, 3863 ... CR

### Features

These incremental shaft encoders in combination with the FAULHABER DC-Micromotors are used for the indication and control of both shaft velocity and direction of rotation as well as for positioning.

The encoder is integrated in the DC-Micromotors SR-Series and extends the overall length by only 1,4 mm!

Solid state Hall sensors and a low inertia magnetic disc provide two channels with 90° phase shift.

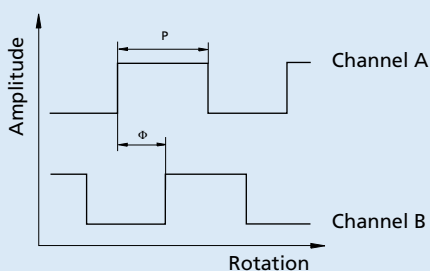
The supply voltage for the encoder and the DC-Micromotor as well as the two channel output signals are interfaced through a ribbon cable with connector.

Details for the DC-Micromotors and suitable reduction gearheads are on separate catalogue pages.

### Output signals / Circuit diagram / Connector information

#### Output signals

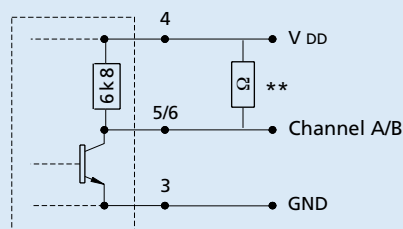
with clockwise rotation as seen from the shaft end



Admissible deviation of phase shift:

$$\Delta\Phi = \left| 90^\circ - \frac{\Phi}{P} * 180^\circ \right| \leq 45^\circ$$

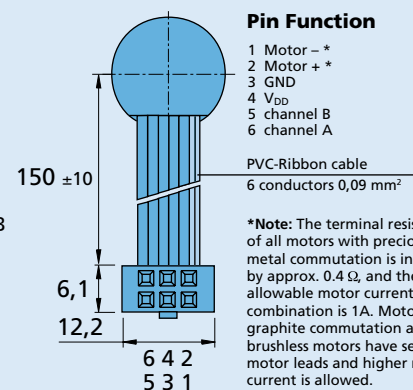
#### Output circuit



\*\* An additional external pull-up resistor can be added to improve the rise time. Caution: I<sub>OUT</sub> max. 15 mA must not be exceeded!

#### Pin Function

- 1 Motor - \*
- 2 Motor + \*
- 3 GND
- 4 V<sub>DD</sub>
- 5 channel B
- 6 channel A



\*Note: The terminal resistance of all motors with precious metal commutation is increased by approx. 0.4 Ω, and the max. allowable motor current in combination is 1A. Motors with graphite commutation and brushless motors have separate motor leads and higher motor current is allowed.

**Connector**  
 DIN-41651  
 grid 2,54 mm

**D. Faulhaber DC Micromotor 1516E012SR + 16A 41:1 + IE2-16 - Motor  
80 & Encoder specifications**

---

# BIBLIOGRAPHY

- 3Dconnexion (2018). SpaceMouse Compact. [https://www.3dconnexion.es/spacemouse\\_compact/es/](https://www.3dconnexion.es/spacemouse_compact/es/). [Online; accessed 31-05-2018].
- Al Bareeq, R., Jayaraman, S., Kiaii, B., Schlachta, C., Denstedt, J. D., and Pautler, S. E. (2008). The role of surgical simulation and the learning curve in robot-assisted surgery. *Journal of robotic surgery*, 2(1):11–15.
- Alenezi, H. and Denstedt, J. D. (2015). Flexible ureteroscopy: Technological advancements, current indications and outcomes in the treatment of urolithiasis. *Asian journal of urology*, 2(3):133–141.
- Alvizatos, G. and Skolarikos, A. (2006). Is there still a role for open surgery in the management of renal stones? *Current opinion in Urology*, 16(2):106–111.
- Alletti, S. G., Rossitto, C., Fanfani, F., Fagotti, A., Costantini, B., Gidaro, S., Monterossi, G., Selvaggi, L., and Scambia, G. (2015). Telelap alf-x-assisted laparoscopy for ovarian cyst enucleation: report of the first 10 cases. *Journal of minimally invasive gynecology*, 22(6):1079–1083.
- Anam, K. and Al-Jumaily, A. A. (2012). Active exoskeleton control systems: State of the art. *Procedia Engineering*, 41:988–994.
- Basillote, J. B., Lee, D. I., Eichel, L., and Clayman, R. V. (2004). Ureteroscopes: flexible, rigid, and semirigid. *Urologic Clinics of North America*, 31(1):21–32.
- Beiko, D. T. and Denstedt, J. D. (2007). Advances in ureterorenoscopy. *Urologic Clinics of North America*, 34(3):397–408.
- Bender, J., Müller, M., and Macklin, M. (2015). Position-based simulation methods in computer graphics. In *Eurographics (Tutorials)*.

- Berman, B. (2012). 3-d printing: The new industrial revolution. *Business horizons*, 55(2):155–162.
- Berndt, I., Torchelsen, R., and Maciel, A. (2017). Efficient surgical cutting with position-based dynamics. *IEEE computer graphics and applications*, 38(3):24–31.
- Boston Scientific Urology (2016). Flexible Ureteroscopy with Dr. Sur, Small Stone Procedure. [https://www.youtube.com/watch?v=Yu8dL92\\_6Z0](https://www.youtube.com/watch?v=Yu8dL92_6Z0). [Online; accessed 31-05-2018].
- Breda, A., Ogunyemi, O., Leppert, J. T., Lam, J. S., and Schulam, P. G. (2008). Flexible ureteroscopy and laser lithotripsy for single intrarenal stones 2 cm or greater—is this the new frontier? *The Journal of urology*, 179(3):981–984.
- Breda, A., Ogunyemi, O., Leppert, J. T., and Schulam, P. G. (2009). Flexible ureteroscopy and laser lithotripsy for multiple unilateral intrarenal stones. *European urology*, 55(5):1190–1197.
- Brehmer, M. and Swartz, R. (2005). Training on bench models improves dexterity in ureteroscopy. *European urology*, 48(3):458–463.
- Brehmer, M. and Tolley, D. A. (2002). Validation of a bench model for endoscopic surgery in the upper urinary tract. *European urology*, 42(2):175–180.
- Buscarini, M. and Conlin, M. (2008). Update on flexible ureteroscopy. *Urologia internationalis*, 80(1):1–7.
- Cadeddu, J. A., Stoianovici, D., Chen, R. N., Moore, R. G., and Kavoussi, L. R. (1998). Stereotactic mechanical percutaneous renal access. *Journal of Endourology*, 12(2):121–125.
- Cadiere, G.-B., Himpens, J., Germay, O., Izizaw, R., Degueudre, M., Vandromme, J., Capelluto, E., and Bruyns, J. (2001). Feasibility of robotic laparoscopic surgery: 146 cases. *World journal of surgery*, 25(11):1467–1477.
- Camara, M., Mayer, E., Darzi, A., and Pratt, P. (2016). Soft tissue deformation for surgical simulation: a position-based dynamics approach. *International journal of computer assisted radiology and surgery*, 11(6):919–928.
- CHAI3D (2018). CHAI3D website. <http://www.chai3d.org/>. [Online; accessed 01-06-2018].
- Coronado, P. J., Herraiz, M. A., Magrina, J. F., Fasero, M., and Vidart, J. A. (2012). Comparison of perioperative outcomes and cost of robotic-assisted laparoscopy, laparoscopy and laparotomy for endometrial cancer. *European Journal of Obstetrics & Gynecology and Reproductive Biology*, 165(2):289–294.

- Cuboyo (2018). The environmental impact of 3D printing. <http://www.cuboyo.com/environmental>. [Online; accessed 31-05-2018].
- Desai, M. M., Aron, M., Gill, I. S., Pascal-Haber, G., Ukimura, O., Kaouk, J. H., Stahler, G., Barbagli, F., Carlson, C., and Moll, F. (2008). Flexible robotic retrograde renoscopy: description of novel robotic device and preliminary laboratory experience. *Urology*, 72(1):42–46.
- Desai, M. M., Grover, R., Aron, M., Ganpule, A., Joshi, S. S., Desai, M. R., and Gill, I. S. (2011). Robotic flexible ureteroscopy for renal calculi: initial clinical experience. *The Journal of urology*, 186(2):563–568.
- Dolmans, V. E., Schout, B. M., de Beer, N. A., Bemelmans, B. L., Scherpbier, A. J., and Hendriks, A. J. (2009). The virtual reality endourologic simulator is realistic and useful for educational purposes. *Journal of endourology*, 23(7):1175–1181.
- Dwyer, M. E., Krambeck, A. E., Bergstralh, E. J., Milliner, D. S., Lieske, J. C., and Rule, A. D. (2012). Temporal trends in incidence of kidney stones among children: a 25-year population based study. *The Journal of urology*, 188(1):247–252.
- Edvardsson, V. O., Ingvarsdottir, S. E., Palsson, R., and Indridason, O. S. (2018). Incidence of kidney stone disease in icelandic children and adolescents from 1985 to 2013: results of a nationwide study. *Pediatric Nephrology*, pages 1–10.
- Ernst, S., Ouyang, F., Linder, C., Hertting, K., Stahl, F., Chun, J., Hachiya, H., Bänsch, D., Antz, M., and Kuck, K.-H. (2004). Initial experience with remote catheter ablation using a novel magnetic navigation system: magnetic remote catheter ablation. *Circulation*, 109(12):1472–1475.
- European Association of Urology (2018a). EAU Patient Information - PNL Treatment. <http://patients.uroweb.org/media-library/kidney-and-ureteral-stones/percutaneous-nephrolithotomy-pcnl/>. [Online; accessed 31-05-2018].
- European Association of Urology (2018b). EAU Patient Information - SWL Treatment. <http://patients.uroweb.org/media-library/kidney-and-ureteral-stones/shock-wave-lithotripsy-swl/>. [Online; accessed 31-05-2018].
- European Association of Urology (2018c). EAU Patient Information - Ureteroscopy. <http://patients.uroweb.org/media-library/kidney-and-ureteral-stones/ureteroscopy-urs/>. [Online; accessed 31-05-2018].
- Fanfani, F., Monterossi, G., Fagotti, A., Rossitto, C., Alletti, S. G., Costantini, B., Gallotta, V., Selvaggi, L., Restaino, S., and Scambia, G. (2016). The new robotic telelap alf-x in gynecological surgery: single-center experience. *Surgical endoscopy*, 30(1):215–221.

- Fanfani, F., Restaino, S., Alletti, S. G., Fagotti, A., Monterossi, G., Rossitto, C., Costantini, B., and Scambia, G. (2015). Telelap alf-x robotic-assisted laparoscopic hysterectomy: feasibility and perioperative outcomes. *Journal of minimally invasive gynecology*, 22(6):1011–1017.
- Félix Monasterio-Huelin & Álvaro Gutiérrez (2018). Modelado de un motorDC. <http://robolabo.etsit.upm.es/asignaturas/seco/apuntes/modelado.pdf>. [Online; accessed 01-06-2018].
- Fuchs, K. (2002). Minimally invasive surgery. *Endoscopy*, 34(02):154–159.
- Geavlete, B., Saglam, R., Georgescu, D., Multescu, R., Iordache, V., Kabakci, A., Ene, C., and Geavlete, P. (2016a). The importance of the ergonomics in robotic flexible ureteroscopy versus standard flexible ureteroscopy. *European Urology Supplements*, 15(11):e1454.
- Geavlete, P., Saglam, R., Georgescu, D., Multescu, R., Iordache, V., Kabakci, A. S., Ene, C., and Geavlete, B. (2016b). Robotic flexible ureteroscopy versus classic flexible ureteroscopy in renal stones: the initial romanian experience. *Chirurgia*, 111:326–329.
- Geraghty, R., Jones, P., and Somani, B. K. (2017). Worldwide trends of urinary stone disease treatment over the last two decades: a systematic review. *Journal of endourology*, (ja).
- Guillotreau, J., Gamé, X., Mouzin, M., Doumerc, N., Mallet, R., Sallusto, F., Malavaud, B., and Rischmann, P. (2009). Radical cystectomy for bladder cancer: morbidity of laparoscopic versus open surgery. *The Journal of urology*, 181(2):554–559.
- Hansel Medical Inc (2016). Sensei Robotic System. <http://hansenmedical.com/us/en/cardiac-arrhythmia/sensei-robotic-system/product-overview>. [Online; accessed 31-05-2018].
- Heers, H. and Turney, B. W. (2016). Trends in urological stone disease: a 5-year update of hospital episode statistics. *BJU international*, 118(5):785–789.
- Hesse, A., Brändle, E., Wilbert, D., Köhrmann, K.-U., and Alken, P. (2003). Study on the prevalence and incidence of urolithiasis in germany comparing the years 1979 vs. 2000. *European urology*, 44(6):709–713.
- Hubens, G., Coveliers, H., Balliu, L., Ruppert, M., and Vaneerdeweg, W. (2003). A performance study comparing manual and robotically assisted laparoscopic surgery using the da vinci system. *Surgical Endoscopy and other interventional techniques*, 17(10):1595–1599.
- Jaffray, B. (2005). Minimally invasive surgery. *Archives of disease in childhood*, 90(5):537–542.

- Kiemeneij, F., Patterson, M. S., Amoroso, G., Laarman, G., and Slagboom, T. (2008). Use of the stereotaxis niobe® magnetic navigation system for percutaneous coronary intervention: Results from 350 consecutive patients. *Catheterization and Cardiovascular Interventions*, 71(4):510–516.
- Kunkler, K. (2006). The role of medical simulation: an overview. *The International Journal of Medical Robotics and Computer Assisted Surgery*, 2(3):203–210.
- Lacy, A. M., Delgado, S., Castells, A., Prins, H. A., Arroyo, V., Ibarzabal, A., and Pique, J. M. (2008). The long-term results of a randomized clinical trial of laparoscopy-assisted versus open surgery for colon cancer. *Annals of surgery*, 248(1):1–7.
- Lee, E., Rafiq, A., Merrell, R., Ackerman, R., and Dennerlein, J. (2005). Ergonomics and human factors in endoscopic surgery: a comparison of manual vs telerobotic simulation systems. *Surgical endoscopy and other interventional techniques*, 19(8):1064–1070.
- Lee, G. I., Lee, M. R., Clanton, T., Sutton, E., Park, A. E., and Marohn, M. R. (2014). Comparative assessment of physical and cognitive ergonomics associated with robotic and traditional laparoscopic surgeries. *Surgical endoscopy*, 28(2):456–465.
- Limbs and Things. Uro-Scopic Trainer. [http://assets.limbsandthings.com/documents/Urology\\_REV\\_2.pdf](http://assets.limbsandthings.com/documents/Urology_REV_2.pdf). [Online; accessed 31-05-2018].
- Lomanto, D., Wijerathne, S., Ho, L. K. Y., and Phee, L. S. J. (2015). Flexible endoscopic robot. *Minimally Invasive Therapy & Allied Technologies*, 24(1):37–44.
- Lum, M. J., Friedman, D. C., Sankaranarayanan, G., King, H., Fodero, K., Leuschke, R., Hannaford, B., Rosen, J., and Sinanan, M. N. (2009). The raven: Design and validation of a telesurgery system. *The International Journal of Robotics Research*, 28(9):1183–1197.
- Mack, M. J. (2001). Minimally invasive and robotic surgery. *Jama*, 285(5):568–572.
- Maeso, S., Reza, M., Mayol, J. A., Blasco, J. A., Guerra, M., Andradás, E., and Plana, M. N. (2010). Efficacy of the da vinci surgical system in abdominal surgery compared with that of laparoscopy: a systematic review and meta-analysis.
- Matsumoto, E. D., Hamstra, S. J., Radomski, S. B., and Cusimano, M. D. (2001). A novel approach to endourological training: training at the surgical skills center. *The Journal of urology*, 166(4):1261–1266.
- Mattheis, S., Hasskamp, P., Holtmann, L., Schäfer, C., Geithoff, U., Dominas, N., and Lang, S. (2017). Flex robotic system in transoral robotic surgery: The first 40 patients. *Head & neck*, 39(3):471–475.

- Mediskills Ltd. (2015). Mediskills Standard Scope Trainer. <http://www.mediskills.com/lang/en-us/products/scope-trainer/>. [Online; accessed 31-05-2018].
- Michel, M. S., Knoll, T., Köhrmann, K. U., and Alken, P. (2002). The uro mentor: development and evaluation of a new computer-based interactive training system for virtual life-like simulation of diagnostic and therapeutic endourological procedures. *BJU international*, 89(3):174–177.
- Miller, K., Benden, M., Pickens, A., Shipp, E., and Zheng, Q. (2012). Ergonomics principles associated with laparoscopic surgeon injury/illness. *Human factors*, 54(6):1087–1092.
- Müller, M., Heidelberger, B., Hennix, M., and Ratcliff, J. (2007). Position based dynamics. *Journal of Visual Communication and Image Representation*, 18(2):109–118.
- Müller, M., Heidelberger, B., Teschner, M., and Gross, M. (2005). Meshless deformations based on shape matching. *ACM transactions on graphics (TOG)*, 24(3):471–478.
- Nealen, A., Müller, M., Keiser, R., Boxerman, E., and Carlson, M. (2006). Physically based deformable models in computer graphics. In *Computer graphics forum*, volume 25, pages 809–836. Wiley Online Library.
- Nick Brook Urologist (2013). Ureteroscopy (Semi-Rigid). <http://www.nickbrookurology.com/ureteroscopy-semi-rigid>. [Online; accessed 31-05-2018].
- Oakley, I., McGee, M. R., Brewster, S., and Gray, P. (2000). Putting the feel in 'look and feel '. In *Proceedings of the SIGCHI conference on Human Factors in Computing Systems*, pages 415–422. ACM.
- Ogata, K. (2010). *Ingeniería de control moderna, 5ª Ed.* Pearson.
- Park, A., Lee, G., Seagull, F. J., Meenaghan, N., and Dexter, D. (2010). Patients benefit while surgeons suffer: an impending epidemic. *Journal of the American College of Surgeons*, 210(3):306–313.
- Peral Boiza, M., Gómez Fernández, T., Sánchez González, P., Rodríguez Vila, B., Gómez Aguilera, E. J., and Gutiérrez Martín, Á. (2017). Virtual reality training platform for flexible ureterorenoscopy interventions with a minimally invasive surgical robot.
- Peters, B. S., Armijo, P. R., Krause, C., Choudhury, S. A., and Oleynikov, D. (2018). Review of emerging surgical robotic technology. *Surgical endoscopy*, pages 1–20.

- Pigazzi, A., Ellenhorn, J., Ballantyne, G., and Paz, I. (2006). Robotic-assisted laparoscopic low anterior resection with total mesorectal excision for rectal cancer. *Surgical Endoscopy and Other Interventional Techniques*, 20(10):1521–1525.
- Prezioso, D., Illiano, E., Piccinocchi, G., Cricelli, C., Piccinocchi, R., Saita, A., Micheli, C., and Trinchieri, A. (2014). Urolithiasis in italy: an epidemiological study. *Archivio Italiano di Urologia e Andrologia*, 86(2):99–102.
- Qian, K., Bai, J., Yang, X., Pan, J., and Zhang, J. (2017). Essential techniques for laparoscopic surgery simulation. *Computer Animation and Virtual Worlds*, 28(2).
- Remacle, M., Prasad, V., Lawson, G., Plisson, L., Bachy, V., and Van der Vorst, S. (2015). Transoral robotic surgery (tors) with the medrobotics flex<sup>TM</sup> system: first surgical application on humans. *European Archives of Oto-Rhino-Laryngology*, 272(6):1451–1455.
- Routh, J. C., Graham, D. A., and Nelson, C. P. (2010). Epidemiological trends in pediatric urolithiasis at united states freestanding pediatric hospitals. *The Journal of urology*, 184(3):1100–1105.
- Ruspini, D. C., Kolarov, K., and Khatib, O. (1997). The haptic display of complex graphical environments. In *Proceedings of the 24th annual conference on Computer graphics and interactive techniques*, pages 345–352. ACM Press/Addison-Wesley Publishing Co.
- Saglam, R., Muslumanoglu, A. Y., Tokatlı, Z., Çaşkurlu, T., Sarica, K., Taşçı, A. İ., Erkurt, B., Süer, E., Kabakci, A. S., Preminger, G., et al. (2014). A new robot for flexible ureteroscopy: development and early clinical results (ideal stage 1–2b). *European urology*, 66(6):1092–1100.
- Sari, V., Nieboer, T. E., Vierhout, M. E., Stegeman, D. F., and Kluivers, K. B. (2010). The operation room as a hostile environment for surgeons: physical complaints during and after laparoscopy. *Minimally Invasive Therapy & Allied Technologies*, 19(2):105–109.
- Sas, D. J., Hulsey, T. C., Shatat, I. F., and Orak, J. K. (2010). Increasing incidence of kidney stones in children evaluated in the emergency department. *The Journal of pediatrics*, 157(1):132–137.
- Scales, C. D., Smith, A. C., Hanley, J. M., Saigal, C. S., in America Project, U. D., et al. (2012). Prevalence of kidney stones in the united states. *European urology*, 62(1):160–165.
- Schout, B., Ananias, H. J., Bemelmans, B. L., d’Ancona, F. C., Muijtjens, A. M., Dolmans, V. E., Scherpbier, A. J., and Hendrikx, A. J. (2010). Transfer of cysto-urethroscopy skills from a virtual-reality simulator to the operating room: a randomized controlled trial. *BJU international*, 106(2):226–231.

- Simbionix (2016). URO - PERC Mentor. [http://simbionix.com/wp-content/pdf/Brochures/URO\\_PERC\\_Brochure\\_12\\_2016-Web.pdf](http://simbionix.com/wp-content/pdf/Brochures/URO_PERC_Brochure_12_2016-Web.pdf). [Online; accessed 31-05-2018].
- Simorov, A., Otte, R. S., Kopietz, C. M., and Oleynikov, D. (2012). Review of surgical robotics user interface: what is the best way to control robotic surgery? *Surgical endoscopy*, 26(8):2117–2125.
- Smithers, B. M., Gotley, D. C., Martin, I., and Thomas, J. M. (2007). Comparison of the outcomes between open and minimally invasive esophagectomy. *Annals of surgery*, 245(2):232.
- Sofia, N. H. and Walter, T. M. (2016). Prevalence and risk factors of kidney stone. *Global Journal For Research Analysis*, 5(3).
- Sorokin, I., Mamoulakis, C., Miyazawa, K., Rodgers, A., Talati, J., and Lotan, Y. (2017). Epidemiology of stone disease across the world. *World journal of urology*, 35(9):1301–1320.
- Su, L.-M., Stoianovici, D., Jarrett, T. W., Patriciu, A., Roberts, W. W., Cadeddu, J. A., Ramakumar, S., Solomon, S. B., and Kavoussi, L. R. (2002). Robotic percutaneous access to the kidney: comparison with standard manual access. *Journal of Endourology*, 16(7):471–475.
- Trejos, A., Patel, R., and Naish, M. (2010). Force sensing and its application in minimally invasive surgery and therapy: a survey. *Proceedings of the Institution of Mechanical Engineers, Part C: Journal of Mechanical Engineering Science*, 224(7):1435–1454.
- Türk, C., Petřík, A., Sarica, K., Seitz, C., Skolarikos, A., Straub, M., and Knoll, T. (2016). Eau guidelines on interventional treatment for urolithiasis. *European urology*, 69(3):475–482.
- Våpenstad, C. and Buzink, S. N. (2013). Procedural virtual reality simulation in minimally invasive surgery. *Surgical endoscopy*, 27(2):364–377.
- Watterson, J. D. and Denstedt, J. D. (2007). Ureterscopy and cystoscopy simulation in urology. *Journal of endourology*, 21(3):263–269.
- Weller, R. (2013). A brief overview of collision detection. In *New Geometric Data Structures for Collision Detection and Haptics*, pages 9–46. Springer.
- White, M. A., DeHaan, A. P., Stephens, D. D., Maes, A. A., and Maatman, T. J. (2010). Validation of a high fidelity adult ureteroscopy and renoscopy simulator. *The Journal of urology*, 183(2):673–677.
- Wikipedia (2018). Stereotaxis. <https://en.wikipedia.org/wiki/Stereotaxis>. [Online; accessed 31-05-2018].

- Wojtyła, S., Klama, P., and Baran, T. (2017). Is 3d printing safe? analysis of the thermal treatment of thermoplastics: Abs, pla, pet, and nylon. *Journal of occupational and environmental hygiene*, 14(6):D80–D85.
- Yasui, T., Iguchi, M., Suzuki, S., and Kohri, K. (2008). Prevalence and epidemiological characteristics of urolithiasis in japan: national trends between 1965 and 2005. *Urology*, 71(2):209–213.
- Zhang, L., Khare, R., Wilson, E., Wang, S., Peters, C. A., and Cleary, K. (2014). Robotic assistance for manipulating a flexible endoscope. In *Robotics and Automation (ICRA), 2014 IEEE International Conference on*, pages 5380–5385. IEEE.
- Zilles, C. B. and Salisbury, J. K. (1995). A constraint-based god-object method for haptic display. In *Intelligent Robots and Systems 95. Human Robot Interaction and Cooperative Robots', Proceedings. 1995 IEEE/RSJ International Conference on*, volume 3, pages 146–151. IEEE.